creative commons
COMMONS DEED

저작자표시-비영리-변경금지 2.0 대한민국

이용자는 아래의 조건을 따르는 경우에 한하여 자유롭게

- 이 저작물을 복제, 배포, 전송, 전시, 공연 및 방송할 수 있습니다.

다음과 같은 조건을 따라야 합니다:

저작자표시. 귀하는 원저작자를 표시하여야 합니다.

비영리. 귀하는 이 저작물을 영리 목적으로 이용할 수 없습니다.

변경금지. 귀하는 이 저작물을 개작, 변형 또는 가공할 수 없습니다.

- 귀하는, 이 저작물의 재이용이나 배포의 경우, 이 저작물에 적용된 이용허락조건을 명확하게 나타내어야 합니다.
- 저작권자로부터 별도의 허가를 받으면 이러한 조건들은 적용되지 않습니다.

저작권법에 따른 이용자의 권리는 위의 내용에 의하여 영향을 받지 않습니다.

이것은 이용허락규약(Legal Code)을 이해하기 쉽게 요약한 것입니다.

Disclaimer

dCollection

공학박사 학위논문

Study on the Photocatalytic Hydrogen Production System Using Chemically Surface-Modified Graphene Quantum Dots

화학적으로 표면 개질된 그래핀 양자점을 이용한 광촉매적 수소 생산 시스템에 대한 연구

2023년 2월

서울대학교 대학원

재료공학부

박 현 호

Study on the Photocatalytic Hydrogen Production System Using Chemically Surface-Modified Graphene Quantum Dots

화학적으로 표면 개질된 그래핀 양자점을 이용한 광촉매적 수소 생산 시스템에 대한 연구

지도교수 박 수 영

이 논문을 공학박사 학위논문으로 제출함

2023년 2월

서울대학교 대학원

재료공학부

박 현 호

박현호의 공학박사 학위논문을 인준함

2023년 2월

위 원 장 안 철 희 (인)

부위원장 박 수 영 (인)

위 원 권 민 상 (인)

위 원 권 지 언 (인)

위 원 안 병 관 (인)

Abstract

Hydrogen energy, one of the most promising renewable energy resources, has recently attracted a lot of attention due to its advantages such as convenience of movement and transportation, and high energy density. To produce hydrogen efficiently, it is required to find efficient photocatalyst material for hydrogen evolution reaction (HER). One of the most promising photocatalyst materials is graphene quantum dot (GQD). GQD have already been studied several times as HER photocatalysts, but low visible light absorption and charge trap sites on the surface limit GQD to have high HER performance. Therefore, research on modification and design is still needed for efficient HER performance. This thesis focused on designing efficient HER photocatalysts through chemical modification and dye-sensitization strategies for GQD.

In chapter 2, ethylene diamine (EDA) functionalized GQD was synthesized by amide bond formation reaction. EDA functionalized GQD exhibited significantly increased HER performance (342 μmol/g of hydrogen after 10 hours) compared to bare GQD (150 μmol/g of hydrogen after 10 hours). Importantly, the HER

performance of EDA functionalized GQD increased proportionally to pH and peaked at pH = 10, in stark contrast to the simple decreasing HER performance with the pH of bare GQDs. Through linear sweep voltage measurement and electrochemical impedance spectroscopy, it is confirmed that the covalently bonded EDA acts as a water dissociation site to improve the photocatalyst HER in the alkali medium.

In chapter 3, amphiphilic GQD functionalized with hexylamine was synthesized through amide bond formation reaction. It was confirmed that hexylamine functionalized GQD (GQD-HA) is amphiphilic and can act as photocatalyst and templating surfactant simultaneously. GQD-HA can form much more stable composite nanoparticles with a thermally activated delayed fluorescence (TADF) photosensitizer than bare GQDs. Importantly, the HER performance and stability of the composite system are significantly improved after HA functionalization (11.64 mmol/g of hydrogen after 14 hours). Through electrochemical analysis, it was confirmed that the composite nanoparticles with GQD-HA and the photosensitizer have efficient charge separation and fast charge transfer characteristics.

In Chapter 4, a highly efficient photocatalytic HER system with

GQD-HA incorporating visible light sensitizing dyes was demonstrated. It was confirmed that HA functionalization helps GQD produce hydrogen more efficiently by providing trap passivation properties and availability of dye sensitization. GQD-HA formed modified nanostructures through strong interactions with photosensitizers. Dye-mixed GQD-HA nanostructures showed efficient HER performance (initial rates of 0.182 mmol/g · h and 1.303 mmol/g of hydrogen after 15 hours) and AQY of 22.5% under 500 nm light irradiation. It also showed enhanced stability in both pure and simulated seawater. Dye-sensitized GQD-HA showed high charge separation and efficient charge transfer characteristics through electrochemical analysis.

Keyword : Water splitting; Hydrogen evolution reaction (HER); Graphene quantum dots (GQD); Functionalization; Dye-sensitization

Student Number : 2018-21006

Table of Contents

List of Tables

List of Schemes

List of Figures

Chapter 1. Introduction

1.1 Photocatalytic Hydrogen Evolution Reaction

Recently, the global energy crisis has emerged as one of the important issues. Fossil fuels such as petroleum and coal are the most used energy sources, accounting for about 80% of human energy consumption. They cause problems such as CO_2 emission and environmental pollution. Moreover, in that these fossil fuels have limited reserves, it is important to find new eco-friendly and renewable energy sources.

Hydrogen energy is one of the most promising candidates because of its high energy density (>120 kJ/g) and environment-friendly advantages. However, currently most hydrogen energy is produced from fossil fuels, coal, and petroleum, which makes these advantages meaningless. Therefore, it is essential to develop a new eco-friendly and efficient strategy for producing hydrogen energy. One of the most representative methods is artificial photosynthesis. Artificial photosynthesis is a technology that synthesizes chemical compounds from solar energy, an infinite source of energy, and was developed inspired by natural photosynthesis.[1] In this artificial photosynthesis mechanism, it is required to use adequate semiconductor materials.

At the beginning, the semiconductor absorbs light and generates excited electrons in the conduction band (CB) and holes in the valence band (VB). These generated charge carriers either recombine or move to the surface of the semiconductor and be utilized for photocatalytic reactions. In this respect, the overall efficiency of artificial photosynthesis depends on major processes such as light absorption, charge separation, charge transfer, and catalytic active sites. Therefore, in order to implement a successful artificial photosynthesis system, it is important to introduce strategies that can promote these processes. In the last decades, several strategies, including crystal and morphology modification, bandgap engineering, and surface modification of semiconductor photocatalysts, have been developed in an attempt to improve a performance of photocatalyst materials.[2-5]

Such artificial photosynthesis technology can also be used for hydrogen production. Many researchers have proposed and demonstrated a photocatalytic water splitting system to transform solar energy into hydrogen energy. Photocatalytic hydrogen generation systems can be broadly classified into two types. One of them is a photoelectrochemical water splitting system. It is consisting of two electrodes and a photocurrent is generated. The other system

is photocatalytic water splitting system.[6] Photocatalytic water splitting system uses semiconductor materials dispersed in aqueous solvent, which can absorb solar energy and generate excited electrons during irradiation. Overall water splitting system consists of hydrogen evolution reaction (HER) and oxygen evolution reaction (OER) as shown in Figure 1-1.

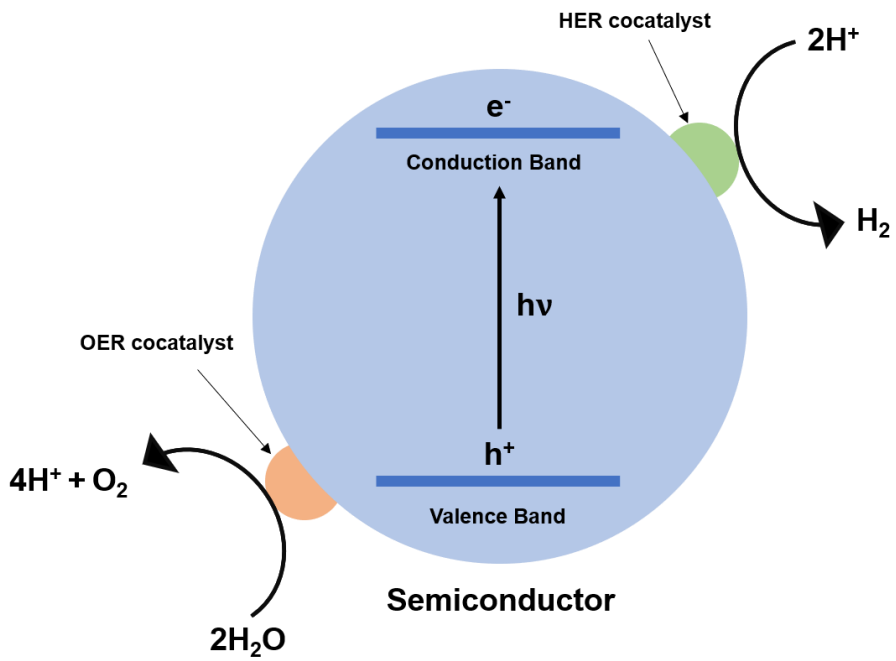

Figure 1-1. Scheme of photocatalytic overall water splitting system

Each reaction proceeds as follows.

$$\text{Oxidation (OER): } 2H_2O \rightarrow O_2 + 4H^+ + 4e^-$$

$$\text{Reduction (HER): } 4H^+ + 4e^- \rightarrow 2H_2$$

$$\text{Overall Reaction: } 2H_2O \rightarrow 2H_2 + O_2$$

The essential conditions for the photocatalytic overall water splitting reaction are as follows: (a) Valence band level of the photocatalyst should be more positive than the water oxidation potential (+1.23 V vs. NHE). (b) Conduction band (CB) level must be more negative than the reduction potential of proton (0 V vs. NHE). Two electrons are needed to make a hydrogen molecule, whereas four electrons are needed to make an oxygen molecule. Since OER requires four electrons, it has large overpotential and relatively sluggish reaction rate than that of HER that requires only two electrons. For this reason, OER acts as a rate determining step for overall water splitting mechanism. In most cases, the slow OER speed acts as a limitation to the overall efficiency of the overall water splitting system.[7, 8]

Another system in which half reaction (HER or OER) is performed separately has been proposed. Each reaction proceeds as follows.[9, 10]

(* denotes an active site on the surface of the photocatalyst)

HER mechanism:

Steps	Acid condition	Alkaline condition
Volmer	$* + H^+ + e^- \rightarrow H*$	$* + H_2O + e^- \rightarrow H* + OH^-$
Heyrovsky	$* + H^+ + e^- + H* \rightarrow H_2 + *$	$* + H_2O + e^- + H* \rightarrow H_2 + OH^- + *$
Tafel	$2H* \rightarrow H_2 + 2*$	$2H* \rightarrow H_2 + 2*$
Overall	$* + 2H^+ + 2e^- \rightarrow H_2$	$* + 2H_2O + 2e^- \rightarrow H_2 + 2OH^-$

Table 1-4. HER mechanism under acid and alkaline condition.

OER mechanism:

	In acid condition	In alkaline condition
	$H_2O \rightarrow OH* + H^+ + e^-$	$OH^- \rightarrow OH* + e^-$
	$OH* \rightarrow O* + H^+ + e^-$	$OH* + OH^- \rightarrow H_2O + 2e^- + O*$
	$2O* \rightarrow O_2$	$2O* \rightarrow O_2$
Overall	$2H_2O \rightarrow O_2 + 4H^+ + 4e^-$	$4OH^- \rightarrow O_2 + 2H_2O + 4e^-$

Table 1-5. OER mechanism under acid and alkaline condition.

Above three basic steps of HER, including the Volmer, Heyrovsky, and Tafel steps, constitute two HER mechanisms: Volmer–Heyrovsky and Volmer–Tafel. The catalytic current increases exponentially with overpotential in both HER mechanisms above, but the rate of current increase can be a variable that identifies the rate-determining step. Tafel slope is a factor with a specific value associated with one of the three basic steps mentioned above, representing the rate of current increase. The experimental relationship between current density and overpotential is defined by the Tafel equation as shown below.[11]

$$\eta = a + b\log(j)$$

where η is overpotential, j is the current density and b is Tafel slope. Theoretically, most cases of electrochemical redox reactions can be explained by Butler–Volmer equation as shown below.[12]

$$j = j_0 \cdot \left\{ \exp\left[\frac{\alpha_a z F \eta}{RT}\right] - \exp\left[-\frac{\alpha_c z F \eta}{RT}\right] \right\}$$

where j_0 is the exchange current density, α is the transfer coefficient, F is the Faraday's constant, R is the universal gas constant, and T is the absolute temperature. When it comes to the high overpotential range, Butler–Volmer equation can be simplified to Tafel equation as shown below.

$$\eta = \pm \frac{RT}{\alpha F} \ln(\frac{j_0}{j})$$

From these equations, it is possible to plot overpotential vs. log j, which can be a great indicator for electrochemical reaction.

Theoretically, when the Volmer step common to both mechanisms acts as the rate−determining step, Tafel slope has a value of about 120 mV /dec. On the other hand, when the Heyrovsky or Tafel steps act as rate−determining steps, the Tafel slopes have values of 40 or 30 mV /dec, respectively. In this respect, experimentally confirming the Tafel slope is an important to explain the HER mechanism and find optimal design of the photocatalyst material.

The difference between HER mechanisms under acidic and alkaline conditions is that H* intermediates are formed by dissociation of water molecules under alkaline conditions. According to Sabatier's principle, the bond strength between the catalyst and H* is generally important for the HER mechanism of photocatalysts. The Sabatier principle is named after the French chemist Paul Sabatier, who suggests that the interaction between the catalyst and the substrate must be appropriate for the catalyst to have high efficiency.[13, 14] In other words, if the interaction is too weak or strong, the catalyst has low efficiency. If the interaction is too weak, the molecule cannot bind to the catalyst and HER does not occur. In contrast, if the interaction

is too strong, the adsorbed H* cannot dissociate from the surface of the photocatalyst. Therefore, the hydrogen bond energy is widely considered as an HER performance descriptor.

In order to realize the half reaction system, there is a disadvantage in that it is necessary to additionally introduce sacrificial reagents which are capable of giving or receiving electrons. However, sacrificial reagents can photo-modify biomaterials into useful new materials, and high-purity hydrogen gas without oxygen can be produced from this system.[15-17] In addition, it has already been reported in many papers that high HER performance can be achieved through this strategy.[18]

For HER systems, most of them are configured as shown in Figure 1-2. In the beginning, a photosensitizer absorbs solar light and generates excited electrons. Consequently, remaining holes in HOMO of the photosensitizer receive electrons from sacrificial electron donors and excited electrons transfer to the conduction band (CB) of a semiconductor. At the catalytic sites of the semiconductor, electrons reduce protons and molecular hydrogen is generated. Within this mechanism, electron transfer occurs relatively slowly and rarely compared to other processes. Therefore, in order to use the excited electrons in the catalytic reaction, it is necessary to increase

the excited state lifetime and prevent charge recombination.

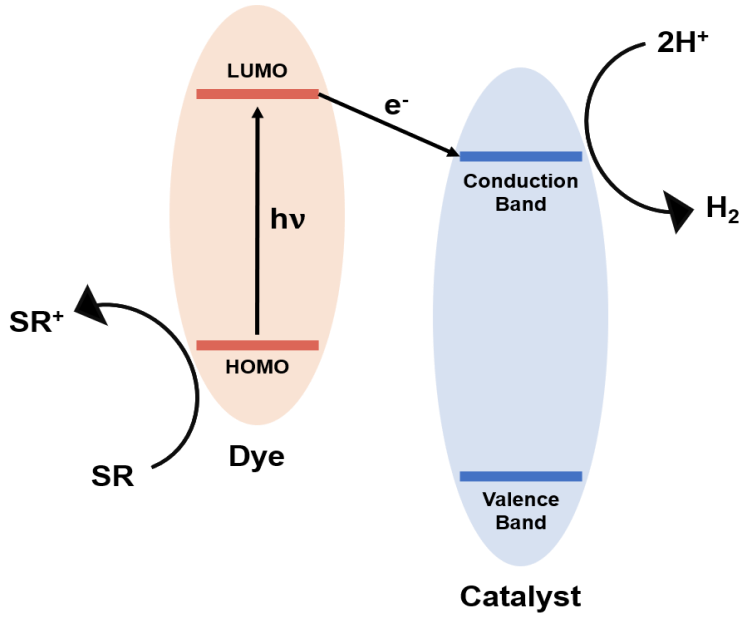

Figure 1-2. Scheme of dye-sensitized HER system

Most of the photocatalytic HER systems studied so far have been designed based on fresh water, which accounts for only about 3% of the total water. However, a vast amount of water is needed to meet the vast energy needs around the world, and it is difficult to meet them with only existing fresh water. In addition, the purification and desalination process of converting seawater, which accounts for about 97% of the total water, into fresh water, are expensive, which acts as the biggest obstacle to the commercialization of water splitting systems. In order to solve this problem, it is important to design a photocatalytic system capable of using seawater directly.[19-

[21] The difference between seawater and fresh water is that seawater contains a huge amount of ions and impurities. The ion composition ratio of the actual seawater is shown in Table 1-3.[22]

Table 1-6. The composition of standard seawater with salinity = 35 g/kg.

Species	Concentration		Specific concentration (g/kg)/s
	(g/kg of seawater)	(mol/kg of seawater)	
Na^+	10.784	0.469	0.308
Mg^{2+}	1.284	0.053	0.037
K^+	0.412	0.010	0.011
Ca^{2+}	0.399	0.010	0.012
Sr^{2+}	0.008	-	-
F^-	0.001	-	-
Cl^-	19.353	0.546	0.553
SO_4^{2-}	2.412	0.028	0.078
HCO_3^-	0.107	0.002	0.003
Br^-	0.067	0.001	0.002
CO_3^{2-}	0.016	-	-
$B(OH^-)_4$	0.008	-	-
$B(OH)_3$	0.019	-	-
Total	35.171	1.120	1.005

These various ions in seawater can affect the stability and performance of photocatalytic systems. In particular, it is difficult to maintain the photocatalytic HER system in seawater stably because the corrosivity in seawater is very high. Since there have been few reports of stable operation of photocatalytic HER systems in seawater, it is important to find new and stable photocatalysts that are suitable for photocatalytic HER in seawater.

1.2 Graphene Quantum Dots

Since the first demonstration of a photoelectrochemical cell composed of TiO_2 photoelectrode designed by Fujishima and Honda in 1972,[23] many studies have been focused on water splitting systems using metal-based semiconductor materials including metal oxides and sulfides.[24-27] Although these materials are highly efficient, their rapid charge recombination, toxicity, corrosion, and low selectivity limit their sustainable utilization. To overcome these limitations, it is desirable to find metal free photocatalysts which are earth-abundant and environment friendly.

From this point of view, many studies have recently been conducted on graphene-based materials. Graphene is a two-dimensional material in which sp^2-hybridized carbon atoms are connected in a

lattice structure. In 2004, Geim and Novoslov obtained monolayer-type graphite using scotch tape technique, which was the first discovery of graphene.[28] Since then, numerous studies have been conducted on the synthesis, characteristics, and application of graphene. Due to the unique sp^2-hybridized carbon network, graphene has a very high thermal conductivity, fast charge mobility, and large surface area. These properties make graphene one of the promising candidates as an ideal support for photocatalytic systems. Therefore, several studies have been conducted on the applicability of graphene materials to photocatalytic systems.[29, 30]

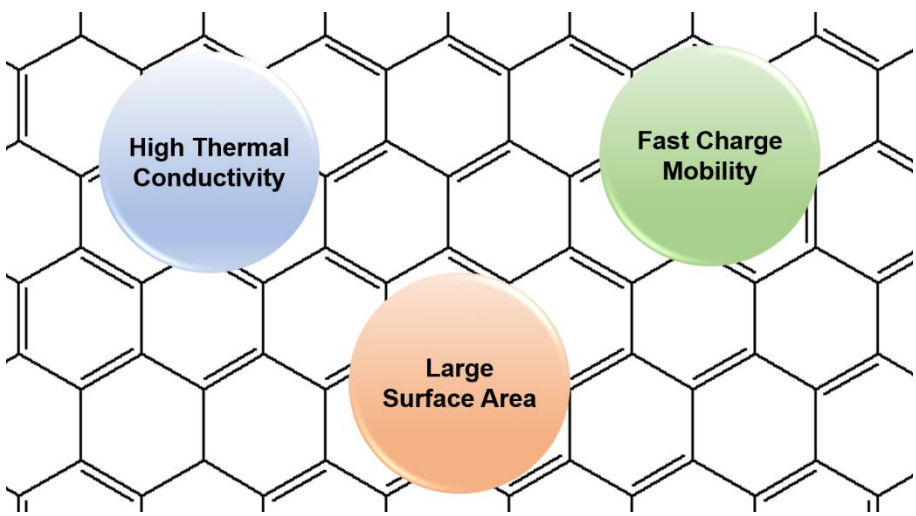

Figure 1-3. Properties of graphene

However, graphene has a zero bandgap, which limits its application as a sole photocatalyst. To solve this problem, many studies have been conducted to change the characteristics by causing structural

modification in graphene. Among them, the most successful result is graphene quantum dots (GQDs). GQD is a piece of graphene having a size of 1 to 20 nm. Due to a quantum confinement effect that is induced from small size, the band gap of GQD is open and has semiconductor properties. In addition, the properties of GQDs can be modified by various strategies such as heteroatom doping, functionalization or forming composites with other materials. Because of these characteristics, GQD has applicability to various applications including optical devices, bioimaging, drug delivery, and photocatalysis.[31-36]

Synthetic strategies for GQD are broadly categorized into two broad categories: top-down methods and bottom-up methods. Top-down methods are strategies for decomposing and exfoliating cheap and easily available bulk graphene-based materials, typically graphite. Such methods usually require several steps including concentrated acid, strong oxidizing reagents, and high temperature and pressure. Although these methods are relatively simple, they lack precise control over the shape and size distribution of the generated particles. On the other hand, bottom-up methods are strategies for synthesizing quantum dots from aromatic compounds. Although these methods are complex, they can control the characteristics of the final

product more precisely.

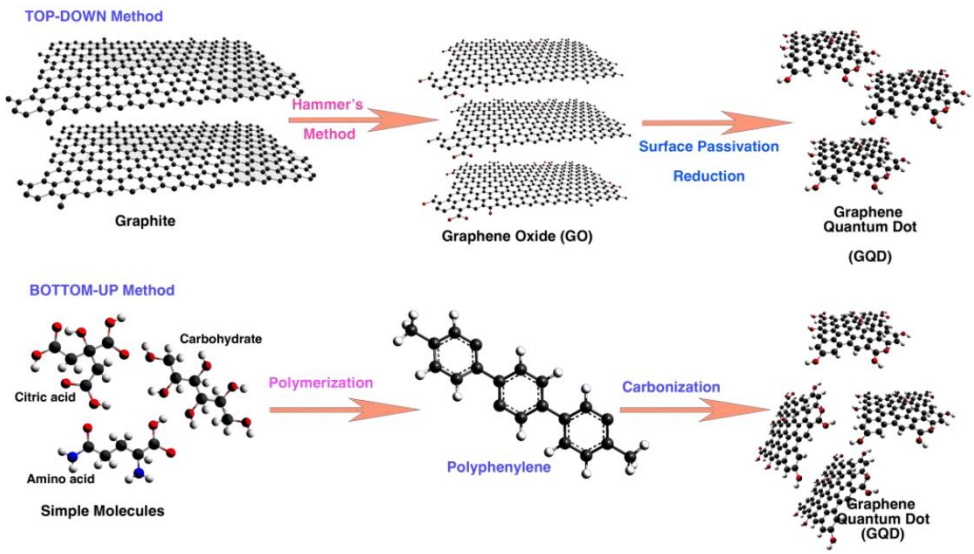

Figure 1-4. Synthetic strategies for GQD.[37]

1.3 Purpose of Research

Despite these excellent advantages, it is difficult to use GQD in photocatalytic systems due to low visible light absorption and charge trapping sites on the surface. Therefore, in order to produce hydrogen efficiently using GQD, it is essential to adapt novel strategies such as dye-sensitization, functionalization, and surface modification. In this thesis, we demonstrated several strategies to design efficient GQD-based photocatalytic HER systems.

In chapter 2, we have synthesized covalently functionalized GQDs

with ethylenediamine (EDA) by an amide coupling reaction. It was found that EDA-functionalized GQDs generally exhibited much higher HER activity (342 μmol/g of hydrogen after 10 hours) than bare GQDs (150 μmol/g of hydrogen after 10 hours). Importantly, the HER activity of EDA-functionalized GQDs increased in proportion to the pH and peaked at pH = 10, which is in stark contrast to the simple decreasing HER rate with the pH of bare GQDs. Through linear sweep voltammetry measurement and electrochemical impedance spectroscopy analysis, it was verified that covalently bonded EDA acts as water dissociation sites to enhance the photocatalytic HER in alkaline medium.

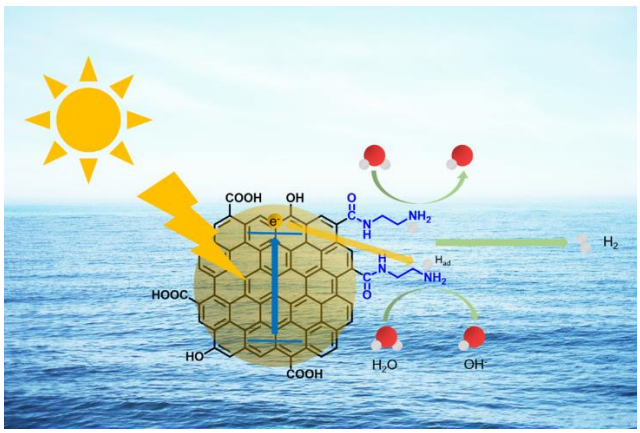

Figure 1-5. An overview of chapter 1.

In chapter 3, we have synthesized amphiphilic GQD by hexylamine (HA) functionalization through an amide bond formation reaction. We

confirmed that HA functionalized GQD (GQD-HA) is amphiphilic and can act as the photocatalyst and templating surfactant at the same time. GQD-HA can form much more stable composite nanoparticles with thermally activated delayed fluorescence (TADF) photosensitizer than bare GQD. Importantly, the HER performance and the stability of the composite systems are remarkably enhanced after HA functionalization (11.64 mmol/g of hydrogen after 14 hours). Through electrochemical analyses, it was verified that composite photosensitizer nanoparticles with GQD-HA have efficient charge separation and fast charge transfer properties.

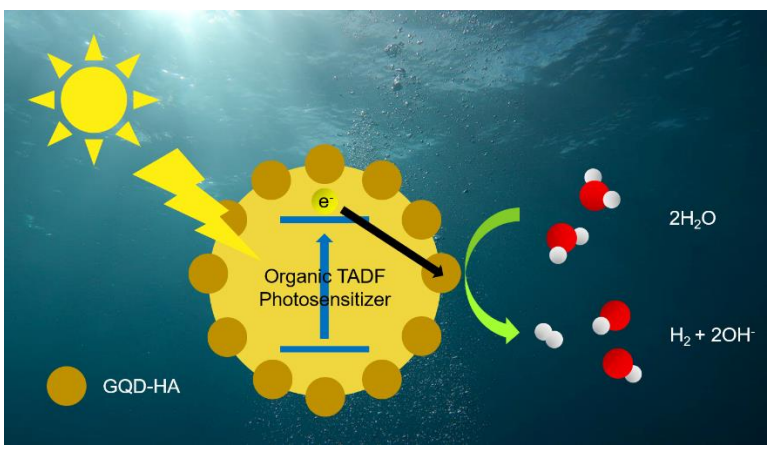

Figure 1-6. An overview of chapter 2.

In chapter 4, we demonstrate highly efficient photocatalytic HER system of hexylamine-functionalized amphiphilic GQD (GQD-HA) incorporating a visible light photosensitizing dye which was enabled

by the trap passivation and dye-sensitization. It was shown that GQD-HA formed a modified nanostructure via strong interaction with the photosensitizer. Dye-incorporated GQD-HA nanostructure showed efficient HER performance (initial rate of 0.182 mmol/g·h and 1.303 mmol/g of hydrogen after 15 hours) and AQY of 22.5% under 500 nm light irradiation. It also showed enhanced stability in both pure water and simulated seawater. Through electrochemical analyses, it was found that the dye-sensitized GQD-HA have high charge separation and efficient charge transfer properties.

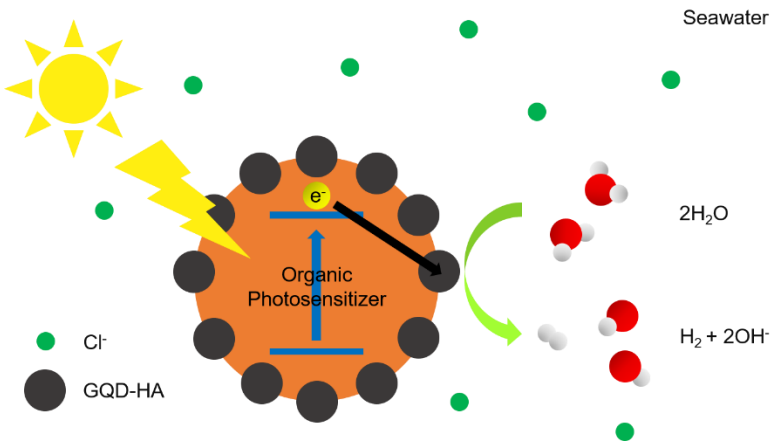

Figure 1-7. An overview of chapter 3.

Bibliography

1. Abas, N.; Kalair, E.; Kalair, A.; Hasan, Q. u.; Khan, N., *International Journal of Hydrogen Energy* **2020,** *45* (41), 20787–20799.

2. Zhang, Z.; Wang, Z.; Cao, S.–W.; Xue, C., *The Journal of Physical Chemistry C* **2013,** *117* (49), 25939–25947.

3. Tu, W.; Zhou, Y.; Li, H.; Li, P.; Zou, Z., *Nanoscale* **2015,** *7* (34), 14232–14236.

4. Zhang, P.; Wang, T.; Chang, X.; Gong, J., *Accounts of Chemical Research* **2016,** *49* (5), 911–921.

5. Zhao, Y.; Zhang, S.; Shi, R.; Waterhouse, G. I. N.; Tang, J.; Zhang, T., *Materials Today* **2020,** *34*, 78–91.

6. Tachibana, Y.; Vayssieres, L.; Durrant, J. R., *Nature Photonics* **2012,** *6* (8), 511–518.

7. Mahmood, N.; Yao, Y.; Zhang, J.–W.; Pan, L.; Zhang, X.; Zou, J.–J., *Advanced Science* **2018,** *5* (2), 1700464.

8. Wei, J.; Zhou, M.; Long, A.; Xue, Y.; Liao, H.; Wei, C.; Xu, Z. J., *Nano–Micro Letters* **2018,** *10* (4), 75.

9. Yan, Z.; Liu, H.; Hao, Z.; Yu, M.; Chen, X.; Chen, J., *Chemical Science* **2020,** *11* (39), 10614–10625.

10. Jin, H.; Guo, C.; Liu, X.; Liu, J.; Vasileff, A.; Jiao, Y.; Zheng, Y.; Qiao, S.–Z., *Chemical Reviews* **2018,** *118* (13), 6337–6408.

11. Shinagawa, T.; Garcia–Esparza, A. T.; Takanabe, K., *Scientific Reports* **2015,** *5* (1), 13801.

12. Adler, S. B., 11 – Sources of cell and electrode polarisation losses in SOFCs. In *High-Temperature Solid Oxide Fuel Cells for the 21st Century (Second Edition)*, Kendall, K.; Kendall, M., Eds. Academic Press: Boston, 2016; pp 357-381.

13. Sabatier, P., *La catalyse en chimie organique*. 1920.

14. Sheng, W.; Myint, M.; Chen, J. G.; Yan, Y., *Energy & Environmental Science* 2013, *6* (5), 1509-1512.

15. Graetzel, M., *Accounts of Chemical Research* 1981, *14* (12), 376-384.

16. Wakerley, D. W.; Kuehnel, M. F.; Orchard, K. L.; Ly, K. H.; Rosser, T. E.; Reisner, E., *Nature Energy* 2017, *2* (4), 1-9.

17. Lhermitte, C. R.; Sivula, K., *ACS Catalysis* 2019, *9* (3), 2007-2017.

18. Miller, D. S.; Bard, A. J.; McLendon, G.; Ferguson, J., *Journal of the American Chemical Society* 1981, *103* (18), 5336-5341.

19. Ayyub, M. M.; Chhetri, M.; Gupta, U.; Roy, A.; Rao, C. N. R., *Chemistry – A European Journal* 2018, *24* (69), 18455-18462.

20. Yao, Y.; Gao, X.; Meng, X., *International Journal of Hydrogen Energy* 2021, *46* (13), 9087-9100.

21. Li, J.; Sun, J.; Li, Z.; Meng, X., *International Journal of Hydrogen Energy* 2022, *47* (69), 29685-29697.

22. Al-Anezi, K.; Hilal, N., *Desalination* 2007, *204* (1), 385-402.

23. Fujishima, A.; Honda, K., *Nature* 1972, *238* (5358), 37-38.

24. Chen, X.; Shen, S.; Guo, L.; Mao, S. S., *Chemical Reviews* 2010, *110* (11), 6503-6570.

25. Yang, Y.; Niu, S.; Han, D.; Liu, T.; Wang, G.; Li, Y., *Advanced Energy Materials* 2017, *7* (19), 1700555.

26. Guo, Y.; Park, T.; Yi, J. W.; Henzie, J.; Kim, J.; Wang, Z.; Jiang, B.; Bando, Y.; Sugahara, Y.; Tang, J.; Yamauchi, Y., *Advanced Materials* 2019, *31* (17), 1807134.

27. Zhao, H.; Li, X.; Cai, M.; Liu, C.; You, Y.; Wang, R.; Channa, A. I.; Lin, F.; Huo, D.; Xu, G.; Tong, X.; Wang, Z. M., *Advanced Energy Materials* 2021, *11* (31), 2101230.

28. Novoselov, K. S.; Geim, A. K.; Morozov, S. V.; Jiang, D.; Zhang, Y.; Dubonos, S. V.; Grigorieva, I. V.; Firsov, A. A., *Science* 2004, *306* (5696), 666-669.

29. Xiang, Q.; Yu, J.; Jaroniec, M., *Chemical Society Reviews* 2012, *41* (2), 782-796.

30. Li, X.; Yu, J.; Wageh, S.; Al-Ghamdi, A. A.; Xie, J., *Small* 2016, *12* (48), 6640-6696.

31. Konstantatos, G.; Badioli, M.; Gaudreau, L.; Osmond, J.; Bernechea, M.; de Arquer, F. P. G.; Gatti, F.; Koppens, F. H. L., *Nature Nanotechnology* 2012, *7* (6), 363-368.

32. Tetsuka, H.; Asahi, R.; Nagoya, A.; Okamoto, K.; Tajima, I.; Ohta, R.; Okamoto, A., *Advanced Materials* 2012, *24* (39), 5333-5338.

33. Yeh, T.-F.; Teng, C.-Y.; Chen, S.-J.; Teng, H., *Advanced Materials* 2014, *26* (20), 3297-3303.

34. Dinda, D.; Park, H.; Lee, H.-J.; Oh, S.; Park, S. Y., *Carbon* 2020, *167*, 760-769.

35. Yang, J.; Miao, H.; Jing, J.; Zhu, Y.; Choi, W., *Applied Catalysis B: Environmental* 2021, *281*, 119547.

36. Chung, S.; Revia, R. A.; Zhang, M., *Advanced Materials* 2021, *33* (22), 1904362.

37. Mousavi, S. M.; Hashemi, S. A.; Yari Kalashgrani, M.; Kurniawan, D.; Gholami, A.; Rahmanian, V.; Omidifar, N.; Chiang, W.-H., *Biosensors* 2022, *12* (7), 461.

Chapter 2. Ethylenediamine functionalized graphene quantum dots as alkaline HER photocatalyst

2.1 Introduction

The discovery of renewable and eco-friendly energy is emerging as an important issue to solve the global energy crisis and environmental pollution. Hydrogen energy has the advantages of high energy density, environmentally friendly, and convenient storage and transportation, which is one of the most promising candidates to replace fossil fuels with hydrogen energy. Currently, however, most of the hydrogen energy is made from fossil fuels, which have limited reserves and environmental pollution, so a new strategy is needed to produce hydrogen energy. In order to produce hydrogen energy eco-friendly, a photocatalytic water splitting system that converts solar energy, an infinite and powerful source of energy, into hydrogen energy has been proposed in many studies.[1-3]

In order to build a successful photocatalytic overall water splitting system, it is important to promote and balance an oxygen evolution

reaction (OER) that is kinetically slower than a hydrogen evolution reaction (HER) due to four-electron transfer and large overpotential. Considering that the OER in acidic medium not only undergoes higher overpotential than the OER in alkaline medium, but also has less available OH^- and no corrosive conditions, it is difficult to find stable and efficient photocatalytic materials that can be used in acidic medium.[4, 5] In this regard, many studies have been conducted on the photocatalytic OER system in alkaline medium, which can serve as the basis for implementing an efficient and stable overall water splitting system.

However, since the HER in alkaline medium occurs much slower than in acidic medium, enhancement is essentially needed to balance the OER rate for overall water splitting.[6, 7] In alkaline medium, HER is carried out through two steps: first, water molecules adsorbed on the surface of the catalyst are dissociated into adsorbed hydrogen atoms and hydroxyl ions. The adsorbed hydrogen atom is then combined with other hydrogen atoms or water molecules in the water to form hydrogen molecules. In general, the water dissociation step called the Volmer step, which is slow enough to act as a rate-determining step for the entire water splitting mechanism, limits the HER performance in alkaline medium. That is, in order to improve the HER performance

in alkaline medium, the water dissociation reaction must occur frequently. In order to facilitate the water dissociation step, it is important to design a catalyst in which water molecules may be easily adsorbed and dissociated on the surface. For example, Danilovic et al. designed a $Ni(OH)_2$–decorated Pt catalyst with much improved HER performance than a bare Pt catalyst.[8] In this system, $Ni(OH)_2$ could act as active sites to decompose water molecule into H_{ad} and OH^- by lowering the energy barriers, thereby improving HER overall performance. Furthermore, Mahmood et al. reported HER system consisting of decorated Ru nanoparticles and nitrogenated holey two–dimensional carbon (C_2N) catalyst. It was confirmed that decorated Ru nanoparticles within the holes of the C_2N catalyst could accelerate the water dissociation reaction for the HER.[9]

The first implementation of the water splitting system was a photoelectrochemical cell consisting of TiO_2 photoelectrode demonstrated by Fujishima and Honda in 1972.[10] Since then, many studies have been conducted on the application of various types of metal–based semiconductor materials including metal oxides and sulfides to water splitting systems.[11–14] These materials exhibit high catalytic efficiency, but their sustainable application is limited due to the fast charge recombination, low visible light absorption, toxicity,

and low selectivity. In order to solve these problems, it is essential to find novel metal-free photocatalysts that are earth-abundant and environment-friendly.

In this respect, many researches have been focused on photocatalysts for water splitting consisting of earth-abundant elements.[15-19] Graphene quantum dots (GQDs) are one of the promising photocatalytic materials, which have attracted much attention recently due to their semiconducting properties.[20, 21] GQDs are a piece of graphene with a size smaller than 100 nm. GQDs are stable in an aqueous solution because of the oxygen-containing groups such as carboxyl group, hydroxyl group, and carbonyl group on the surface. GQD has semiconductor properties and open bandgap that are acquired due to a quantum confinement effect, which can be useful for a variety of applications including photocatalytic HER.[22-27] In addition, several studies have already been conducted to implement GQD-based photocatalytic HER systems through strategies to improve HER performance by introducing heteroatomic doping or photosensitizer into GQD. For example, Tsai et al. reported that nitrogen-doped GQDs could produce more hydrogen than bare GQDs, with an estimated solar-to-hydrogen efficiency of 0.035%.[24] In recent work, we successfully confirmed that Rhodamine 123-

sensitized GQDs could produce 940 μmol/g of hydrogen within 4 h under visible light irradiation.[25] Nevertheless, most studies have generally been conducted under neutral condition in which favorable to efficient HER, and studies to adapt GQD as the photocatalyst for HER in alkaline medium have not yet been conducted.

In order to utilize GQD as the HER photocatalyst under alkaline condition, it is important to introduce additional highly efficient water dissociation sites on the surface of GQD. EDA functionalization is one of the well-known strategies that can introduce primary amines as adsorption sites to provide additional catalytic active sites for energy conversion.[28-33] For example, Cho et al. developed an EDA functionalized graphene material and reported that the CO_2 to CH_4 conversion efficiency can be improved by attached amines which are acting as efficient CO_2 adsorption sites.[31] As an example, in the field of water splitting, Deng et al. proved that the amine group attached to the graphene sheet can improve electron-transfer kinetics by reducing the free energy barrier, which has high HER electrocatalyst efficiency.[32] In addition, Li et al. manufactured a composite of EDA-amidated graphene and TiO_2 to develop a material with high photocatalytic HER efficiency in a neutral solution.[33] Nevertheless, the effect of EDA functionalization strategies on photocatalytic water

splitting efficiency under alkaline condition has not yet been studied. Primary amines of exist in the form of a free amine in alkaline medium, which can act as adsorption sites. Therefore, in this study, in contrast to the HER performance of bare GQD, GQD functionalized with EDA to design a GQD complex (GQD-EDA) that exhibits higher performance in alkaline medium. We have synthesized GQD through hydrothermal reaction of GO. After that, through the amide bond formation reaction, EDA was attached to the surface of GQD by covalent bond to synthesize the GQD-EDA complex. The synthesized GQD-EDA showed improved HER performance compared to the bare GQD. Furthermore, unlike bare GQD, it was confirmed that the HER performance increased as the pH of the solution increased, suggesting that GQD-EDA could be an excellent photocatalyst with high HER performance under alkaline condition. Through photocatalytic performance and electrochemical analysis, it was confirmed that the attached amines of EDA act as water dissociation sites to promote the rate of the water dissociation step, and consequently contribute to the improvement of HER performance.

2.2 Experimental details

2.2.1 Chemical used

All chemicals were of analytical grade and used without any further purification. Graphite powder was purchased from Sigma-Aldrich. Sulfuric acid (H_2SO_4, 95 wt%), phosphoric acid (H_3PO_4, 85 wt%), hydrogen chloride (HCl, 36%), hydrogen peroxide (H_2O_2, 30%), potassium permanganate ($KMnO_4$), and sodium hydroxide (NaOH) were purchased from Samchun Chemical. Sodium nitrate ($NaNO_3$) was purchased from Alfa Aesar. N-Hydroxysuccinimide (NHS) and 2-morpholin-4-ylethanesulfonic acid (MES) were purchased from Sigma-Aldrich. N-(3-Dimethylaminopropyl)-N′-ethylcarbodiimide hydrochloride (EDC) and ethylenediamine (EDA) were purchased from TCI.

2.2.2 Synthesis of graphene oxide

We have synthesized graphene oxide from graphite by the modified Hummers method following our previously reported paper.[25] 2 g of graphite powder was added into 240 mL of concentrated mixed acids (H_2SO_4/H_3PO_4 = 5:1) and the mixture was stirred. Subsequently, 1 g of sodium nitrate ($NaNO_3$) was added to the mixture and stirred for 30 min. Then, the temperature of the mixture was lowered with an

ice bath, and 6 g of potassium permanganate ($KMnO_4$) was added gradually. The rate of addition was controlled thoroughly to keep the temperature below 20 ° C. After that, the ice bath was removed and the temperature was gradually increased to 40 ° C. After 4 h, another 6 g of $KMnO_4$ was added to the mixture at once and the mixture was left at 40 ° C for 12 h. During the reaction, the mixture was gradually turned into a brownish-gray paste. After cooling to room temperature, the mixture was poured into 4 mL ice-cold distilled water with stirring followed by the addition of 8 mL of 30% H_2O_2 solution. An immediate color change from brown to light yellow was observed. The yellow precipitate was left for precipitation. Then, the precipitate was washed with 1 L of 10% HCl solution and then with 2 L of distilled water to remove the unreacted reagents. Finally, the golden viscous GO was suspended in distilled water and stored for further use.

2.2.3 Synthesis of GQD

We have used as-synthesized GO for the synthesis of GQD. We have taken 20 mL (3.5 mg/mL) of GO solution in a beaker and diluted it to 80 mL by adding distilled water. The mixture was ultrasonicated for 30 min for homogeneous dispersion. After that, the pH of the mixture

was adjusted to 8 by adding 2 N NaOH solution followed by sonication for 1 h. The mixture was transferred to a Teflon-lined autoclave and was treated at 200 ° C for 16 h for hydrothermal synthesis. After cooling to room temperature, the filtrate solution was collected through a 0.2 μm Millipore membrane filter and was dialyzed using a KDa dialysis tube for 2 days. The solution was dried and the bright yellow powder was collected.

2.2.4 Synthesis of GQD-EDA

We have covalently attached EDA to the carboxyl groups of the GQD via an amide bond formation reaction to synthesize GQD-EDA. For this, 4 mg of GQD was dissolved in 40 mL of distilled water. Then, 64 mg of MES buffer was dissolved in it to maintain the pH at 6 during the reaction and stirred for 30 min. Then, 58 mg of EDC and 53 mg of NHS were added into it in sequence and stirred for 1 h in the dark. After that, different amounts of EDA (0.1, 0.3, 0.5, 1, and 2 mL) were added into the solution and left for 24 h in the dark for amide bond formation. Afterward, the solution was collected and was dialyzed using a 1 KDa dialysis tube for 3 days to remove unreacted reagents.

2.2.5 Characterizations of the material

We have characterized our synthesized GO, GQD, and GQD-EDA by using different spectroscopic as well as microstructural analyses. Fourier transform infrared spectroscopy (FTIR) was carried out using a Nicolet iS50 spectrometer (Thermo Fisher Scientific). X-ray photoelectron spectroscopy (XPS) was carried out using an AXIS-His (KRATOS) system. Raman analysis was conducted using a LabRAM HR Evolution microscope (HORIBA). X-ray diffraction (XRD) data were obtained by using D8 Advance (Bruker) with a diffractometer equipped with Cu Kα (λ = 1.5418 Å) radiation. JEM-2100F high-resolution transmission electron microscope and JEM-ARM200F Cs corrected transmission electron microscope with Cold FEG were used for morphological analysis. UV-vis absorption and photoluminescence measurements were carried out using a Shimadzu UV-1650 PC and Varian Cary spectrophotometer. The evaluation of the hydrophilicity of our synthesized GQD and GQD-EDA was performed through contact angle measurements using a Drop Shape Analyzer DSA 25 (Krüss GmbH). Deionized water (1.8 μL) was dropped at three points of each sample and the average contact angle was calculated. Measurements were conducted immediately after treatment. FluoTime 200 spectrometer (PicoQuant) equipped with a PicoHarp300 TCSPC board and a PMA182 photomultiplier was used

for fluorescence lifetime measurements.

2.2.6 Photocatalytic HER measurements

We have carried out all the photocatalytic HER measurements in a gas enclosed Pyrex vial system. 1 mg of bare GQD and GQD–EDA composites were used as photocatalyst and 10 vol % triethanolamine (TEOA) was added as sacrificial reagents. Total volume was maintained to 13 mL with distilled water. Argon gas mixed with 1% CH_4 was used as a standard gas to calculate the amount of evolved hydrogen. After gas purging with the standard gas for 15 min, the sample was irradiated with a 300 W xenon lamp with 370 nm band–pass filter. We have calculated the amount of evolved hydrogen gas using an Agilent 7890A gas chromatograph (equipped with a thermal conductivity detector and a 5 Å molecular sieve column) during the photocatalytic measurements. The pH of the solution was adjusted with 2 N HCl and 2 N NaOH aqueous solution. The apparent quantum yield (AQY) was calculated according to the following equation.

$$AQY(\%) = \frac{number\ of\ reacted\ electrons}{number\ of\ incident\ photons} \times 100$$

$$= \frac{number\ of\ evolved\ H_2\ molecules \times 2}{number\ of\ incident\ photons} \times 100$$

2.2.7 Electrochemical measurements

All the electrochemical measurements were carried out using a Vertex.One (Ivium Technology) electrochemical analyzer using a standard three-electrode system. We have used GQD or GQD-EDA materials as the working electrode by drop-casting them over ITO-coated polyethylene terephthalate plates. 0.1 M KOH aqueous solution was used as the supporting electrolyte for linear sweep voltammetry (LSV) measurement and 0.1 M KPF_6 aqueous solution was used as the supporting electrolyte for electrochemical impedance spectroscopy (EIS). Pt wire and Ag/AgCl were used as the counter and reference electrodes, respectively.

2.3 Results and discussion

2.3.1 Structural analysis of the catalyst

First, we have characterized GO and GQD through HR-TEM to verify the formation of GQD from GO sheets through hydrothermal treatment as shown in Figure 2-1. In the TEM image in Figure 2-1(a) of GO and GQD, we confirmed the 2D sheet-like morphology of GO. We also confirmed TEM image of GQD in Figure 2-1(b) and 1(c). GQD has 6~8 nm of size distribution and clear (1120) in-plane crystal lattice structure with spacing of 0.24 nm. Essentially, GO and

GQDs were successfully characterized as published earlier in detail.[20, 34]

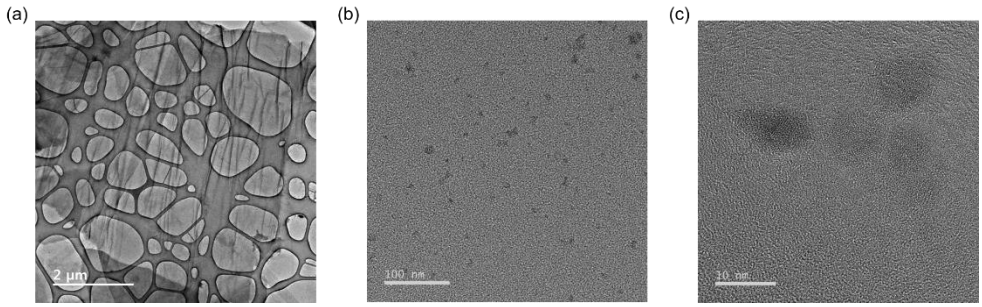

Figure 2-1. TEM image of our (a) synthesized GO and (b), (c) synthesized GQD

Next, we have characterized our newly synthesized GQD-EDA. As can be seen from Cs-corrected transmission electron microscopy image of GQD-EDA in Figure 2-2(a), the size distribution of the GQD-EDA particle is between 6 and 8 nm which is almost same as that of pristine GQD. In HR-TEM image of GQD-EDA as shown in Figure 2-2(b), the crystalline structure with observed lattice spacing of 0.24 nm related to (1120) in-plane lattice spacing of graphene was clearly identified. The particle size distribution and crystalline structure remain almost the same as those of pristine GQD, implying no significant change in physical properties of the core GQD structure after EDA functionalization.

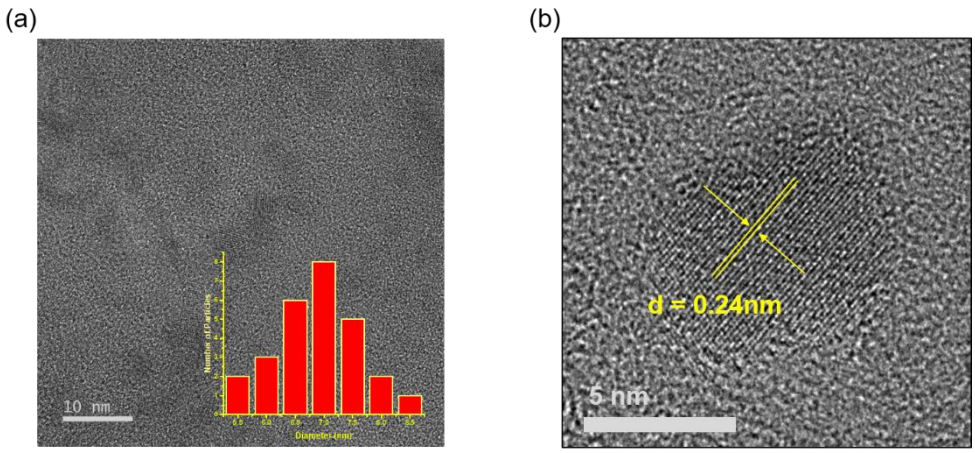

Figure 2-2. TEM images of GQD-EDA. (a) TEM image along with particle size distribution (inset) and (b) HRTEM image with lattice fringes.

Figure 2-3 shows the FTIR spectra of GQD and GQD-EDA. In the spectrum of GQD, several characteristic peaks at 3440, 1600, and 1086 cm^{-1} are assigned to O-H, C=C, and C-O bonds. Other peaks at 1430 and 605 cm^{-1} are assigned to C-OH stretching and C-H bending vibrations.[35] After EDA functionalization of GQD, all characteristic peaks of GQD are still observed in FTIR spectra of the GQD-EDA composite. In addition, a new peak at 1630 cm^{-1} related to an amide bond and a new peak at 1550 cm^{-1} related to N-H in-plane stretching have arisen as a result of amide bond formation between carboxyl groups of GQD and one primary amine of EDA. All these peaks confirm successful EDA functionalization of GQD. Furthermore, two peaks at 3330 and 1470 cm^{-1} have arisen due to the N-H stretching

vibrations of one remaining free primary amine of EDA in the GQD-EDA composite.

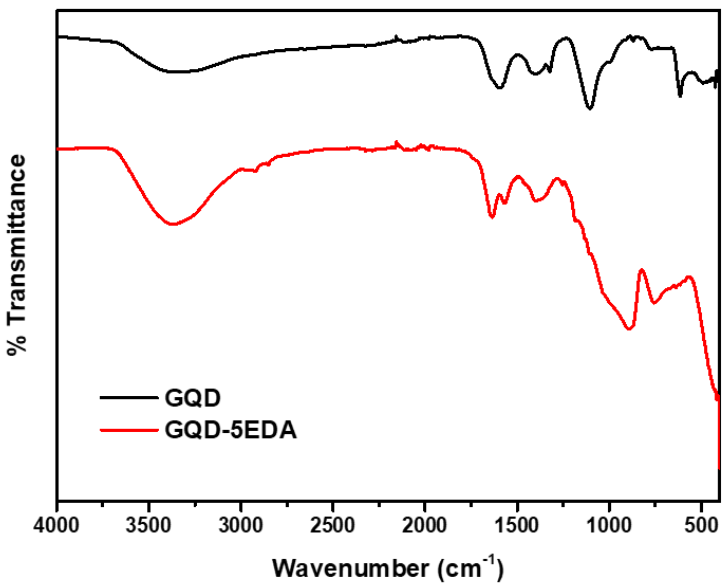

Figure 2-3. Comparison of FTIR spectra of GQD and GQD-5EDA.

As can be seen in low-resolution XPS spectra in Figure 2-4(a), GQDs show only two peaks at 284 and 540 eV for carbon and oxygen, whereas GQD-EDA shows one additional peak around 400 eV for nitrogen. Moreover, we have deconvoluted the XPS spectrum of GQD and GQD-EDA to interpret the exact functional groups of the composite. The deconvoluted C_{1s} spectrum of GQD shows C-C, C-O, C═O, and HO-C═O peaks as described in Figure 2-4(b), whereas the deconvoluted C_{1s} spectrum of GQD-EDA shows C-C, C-O, C═O,

C–N, and HO–C═O peaks as described in Figure 2–4(c). The presence of the C–N peak confirms that GQD is successfully functionalized with EDA. Moreover, the deconvoluted spectrum of N_{1s} shows a free amine peak (C–NH–) and amide (–HN–C═O) bond peaks at 399.5 and 401.5 eV, respectively, as described in Figure 2–4(d).[36] Especially, the peak for amide bond clearly reveals that GQD is covalently functionalized with EDA.

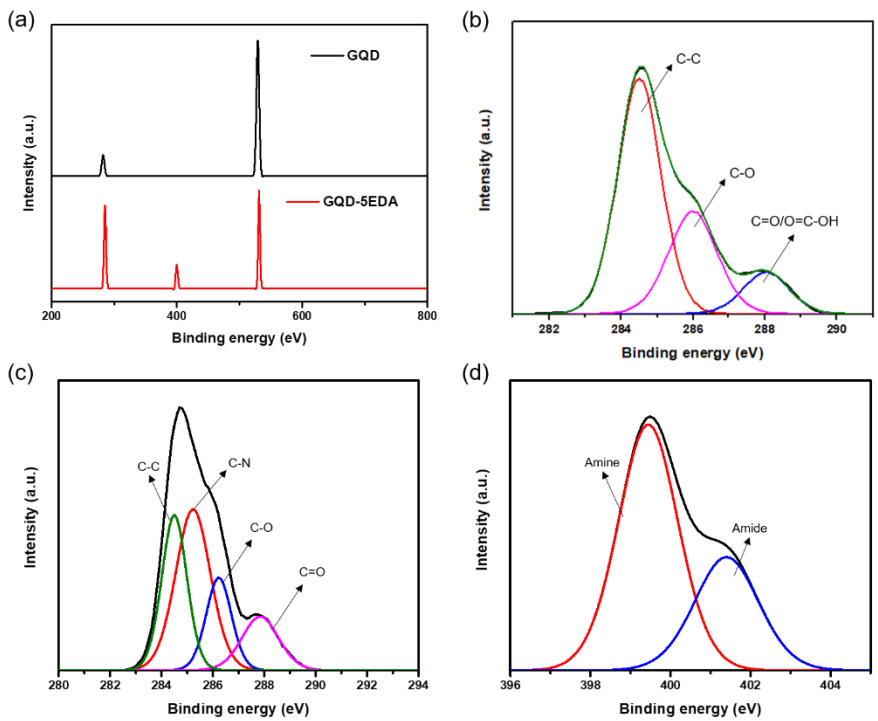

Figure 2–4. (a) Comparison of FTIR spectra of GQD and GQD–5EDA. (b) Comparison of low–resolution XPS spectra of GQD and GQD–5EDA. High–resolution XPS spectra of (c) deconvoluted C_{1s} and (d) deconvoluted N_{1s} of GQD–5EDA.

Actual amount of attached EDA could be estimated by integrating the nitrogen peak area in the low-resolution XPS spectra. Calculation was carried out as follows:

We assumed that number of attached EDA = n, Weight of EDA =52n (ignoring Hydrogen atoms). EDA contains 2n of nitrogen atoms and 2n of carbon atoms (Total 4n of atoms). From the low resolution XPS spectrum of GQD, we observed that carbon : oxygen = 2 : 1. We assumed that number of carbon = 2x, number of oxygen = x, Weight of GQD = 2x×12+x×16=40x. After EDA attaching, the total number of atoms increased from 3x to 3x+4n. If the observed atomic percentage of nitrogen = p %, then

$$\frac{2n}{3x+4n} = \frac{p}{100}$$

$$\frac{200-4p}{3p} n = x$$

Using that,

$$Weight\ of\ GQD\ = 40x = \frac{40 \times (200-4p)}{3p} n$$

From that, we calculated wt% of EDA

$$= \frac{156p}{40(200-4p)}$$

Through these calculations, we confirmed the amount of attached EDA according to the amount of EDA used for the reaction as shown

in Figure 2-5.

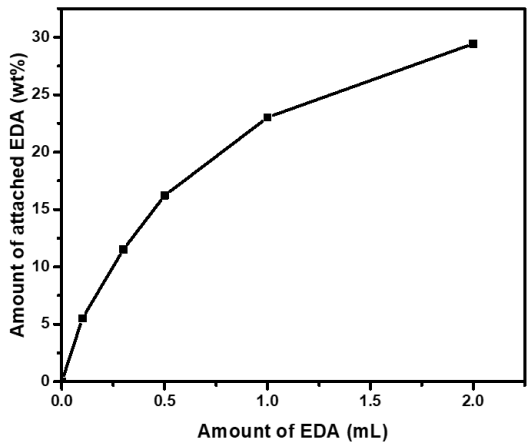

Figure 2-5. Calculated the weight percentage of attached EDA

In addition, we have measured the Raman spectra and XRD spectra of GQD and GQD-EDA to characterize the defect states. As shown in Figure 2-6(a), the peak at 1590 cm^{-1} (G) is related to the vibration of the sp^2-hybridized carbon atoms in the graphene lattice, whereas the peak at 1350 cm^{-1} (D) is related to the out-of-plane vibrations from structural defect states. The Raman spectrum of GQD-EDA (I_D/I_G = 1.03) shows a higher I_D/I_G ratio than GQD (I_D/I_G = 0.97), indicating the generation of structural defect states after EDA functionalization. In the case of XRD spectra in Figure 2-6(b), the XRD spectrum of GQD shows a broad peak around 24° corresponding to the (002) plane of graphene. A broad peak indicates a large area of exposed edge sites obtained from the formation of few

nanometer-sized GQD. Furthermore, no significant change in the XRD spectrum of GQD is observed after EDA functionalization.

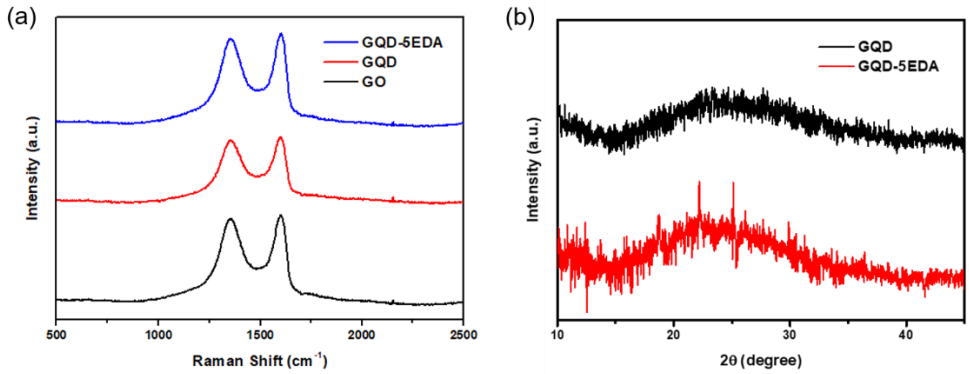

Figure 2-6. (a) Raman spectrum of GO, bare GQD and GQD-5EDA. (b) XRD spectrum of GQD and GQD-5EDA.

2.3.2 Photocatalytic HER Activity and Mechanism

GQD-EDA was evaluated as the photocatalyst for the photocatalytic HER. We conducted all the measurements at pH = 10 with 10 vol % TEOA as a sacrificial electron donor. First, we measured the photocatalytic HER activity of GQD-EDA samples synthesized with different amounts of EDA. Figure 2-7(a) clearly shows that the HER performance of GQD is significantly enhanced by EDA functionalization with a maximum at 16.2 wt% of EDA (GQD-5EDA synthesized with 0.5 mL of EDA).

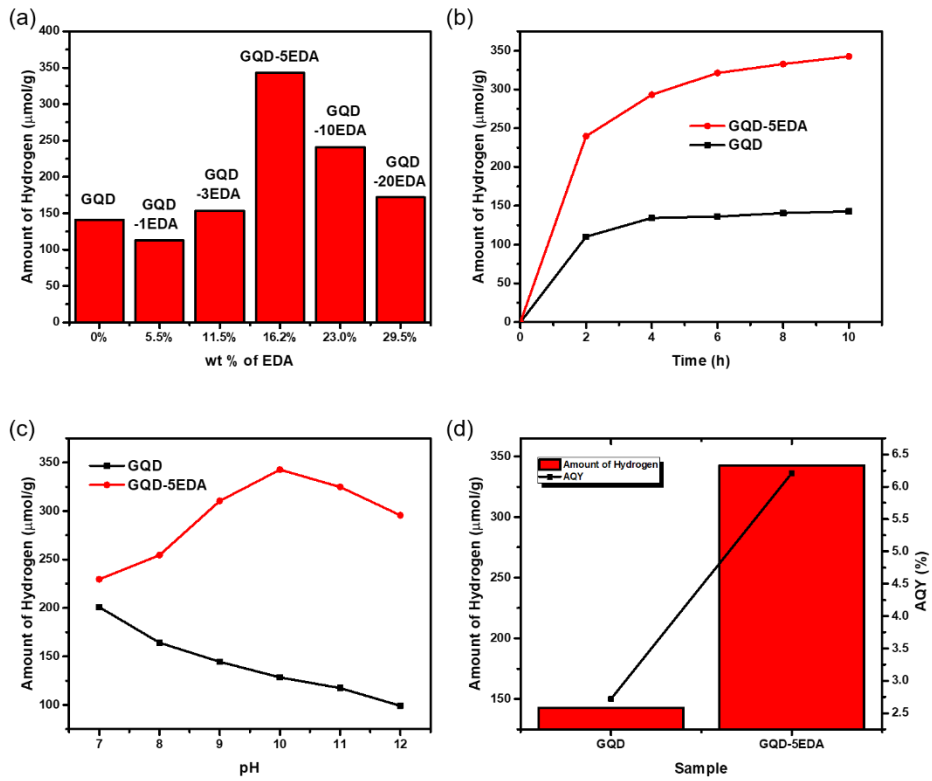

Figure 2-7. (a) Photocatalytic HER efficiency of GQD-EDA at pH = 10 with different wt% of EDA after 10 h of irradiation; (b) comparison of hydrogen evolution efficiency at pH = 10 between GQD and GQD-5EDA within 10 h; (c) pH-dependent HER efficiency of GQD and GQD-5EDA; and (d) AQY values of GQD and GQD-5EDA.

To compare the photocatalytic activity of GQD-EDA with bare GQD, particularly in terms of pH dependency, we have done photocatalytic HER measurement for 10 h. As shown in Figure 2-7(b), we can see that there was an enhancement of the HER activity after EDA functionalization. Bare GQD produce 150 mmol/g of hydrogen molecules (AQE = 2.72%) after 10 h of irradiation, whereas GQD-

5EDA produces 342 mol/g of hydrogen molecules (AQE = 6.21%) after 10 h of irradiation. We further confirmed the pH dependence of the HER activity by adjusting the pH concentration of the sample as shown in Figure 2-7(c). Although bare GQD show a simple decrease in the HER activity with increasing pH, GQD-5EDA shows continuous increase in the HER activity with increasing pH. These results clearly show that the HER activity of GQD, particularly in alkaline solution, could be improved through EDA functionalization.

In addition, to check the photostability of GQD-5EDA, we have measured Raman and XPS analysis of the sample after 10 h of the photocatalytic HER under alkaline condition. As shown in Figure 2-8, still we can observe the Raman peaks of amide bond and N-H after 10 h of HER experiment although their intensities are slightly decreased. Furthermore, as shown in Figure 2-9(a), there is no noticeable change in the low-resolution XPS peaks of C, N, and O. We deconvoluted C_{1s} spectra to confirm the presence of amide linkage of GQD-5EDA after 10 h of the HER. In Figure 2-9(b), we still can find the strong peak of C-N even after 10 h of the photocatalytic HER, which indicates high photostability of the amide linkage.

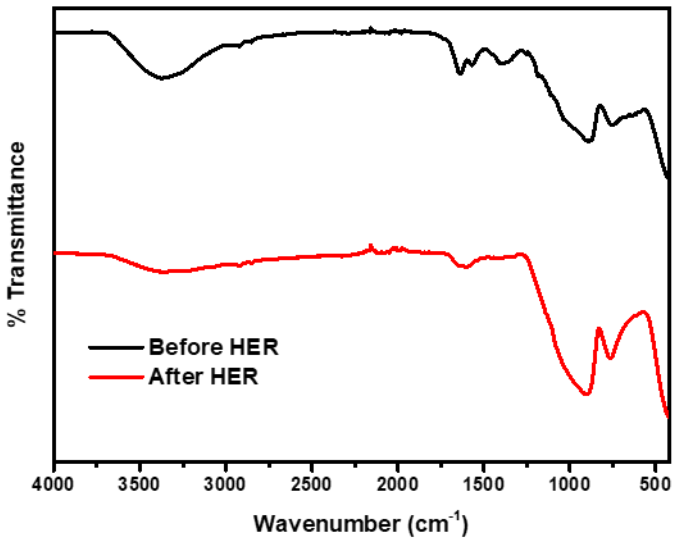

Figure 2-8. Change in FTIR spectrum of GQD-5EDA after 10 h of HER experiment

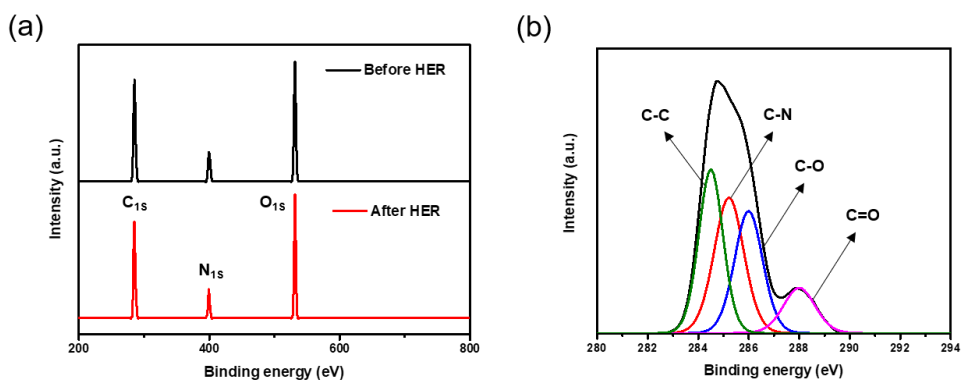

Figure 2-9. (a) low resolution XPS spectrum and (b) deconvoluted C_{1s} spectrum of GQD-5EDA after 10 h of HER experiment under alkaline condition

Indeed, from the pH dependence result depicted in Figure 2-7(c), we can confirm that the enhancement of the HER activity in an alkaline solution is much greater than the enhancement in neutral

solution. As the number of protons generally decreases with increasing pH, the HER activity of bare GQD decreases with increasing pH as well. On the other hand, the HER activity of GQD–5EDA increases along with the increase of pH and then decreases in the range of pH = 11 or higher, most likely according to the following process. In alkaline solution, the HER mechanism consists of several steps. First, water molecules are adsorbed on active sites of a catalyst and dissociate into adsorbed hydrogen atoms and hydroxyl ions, which is called the Volmer step. Then, adsorbed hydrogen atoms are combined with other hydrogen atoms or water molecules and hydrogen molecules are generated.[37] From these results, we can predict the role of the remaining primary amine in GQD–EDA in the photocatalytic HER mechanism. In this case, the primary amines of EDA can act as water adsorption sites because of their strong nucleophilicity, as has already been demonstrated in several other papers.[38, 39] After irradiation, photoexcited electrons in GQD are steadily generated. Then, the amines on the GQD surface easily adsorb water molecules. Adsorbed water molecules accept the excited electrons from GQD and dissociate. Through this mechanism, the pH dependence result can be explained as follows. Because pKa of the primary amine is about 10.6, most of the primary amines of

EDA can present in the form of neutral amines in alkaline medium. These neutral amines can act as water dissociation sites and enhance the HER activity. As the pH decreases, the fraction of neutral amines decreases and the dissociation of water molecules is less likely. Although the HER activity is reduced due to the rapid decrease of proton concentration when the pH is higher than 10, it is still much higher than that of bare GQD. Thus, the pH dependence of the HER activity implies that EDA functionalization can help GQD produce hydrogen efficiently in alkaline solution by providing primary amine sites which act as additional water dissociation sites.

To get further insights into the HER mechanism, we measured contact angles of GQD and GQD–EDA with water droplets. As shown in Figures 2−10 and 2−11, the water contact angle is decreased by EDA functionalization which implies that the primary amines of EDA easily adsorb water molecules.

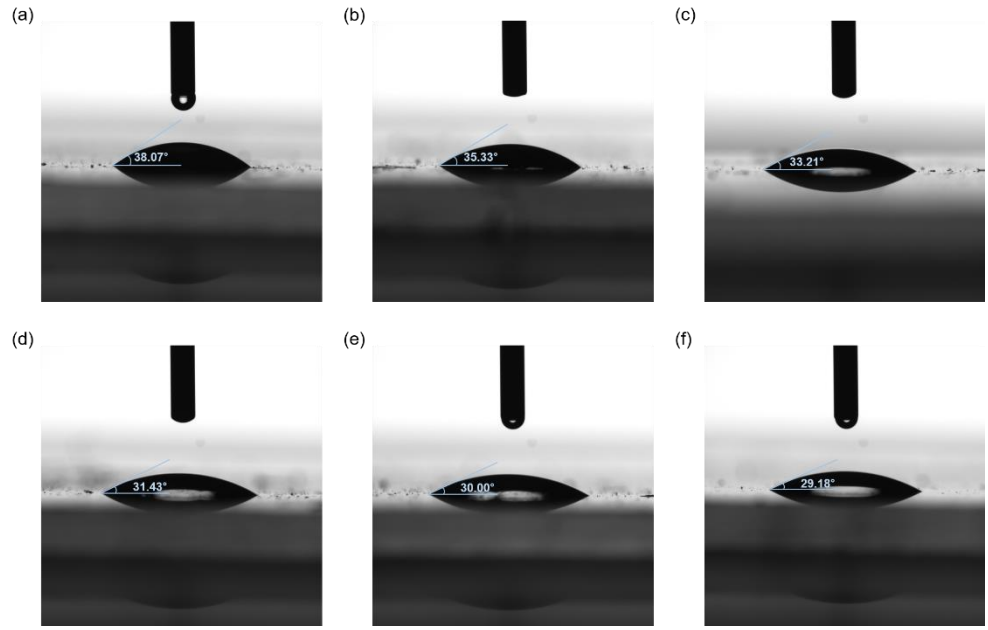

Figure 2-10. Image of water contact angles on (a) bare GQD film, (b) GQD-1EDA (5.9 wt%), (c) GQD-3EDA (11.5 wt%), (d) GQD-5EDA (16.2 wt%), (e) GQD-10EDA (23.0 wt%), and (f) GQD-20EDA (29.5 wt%)

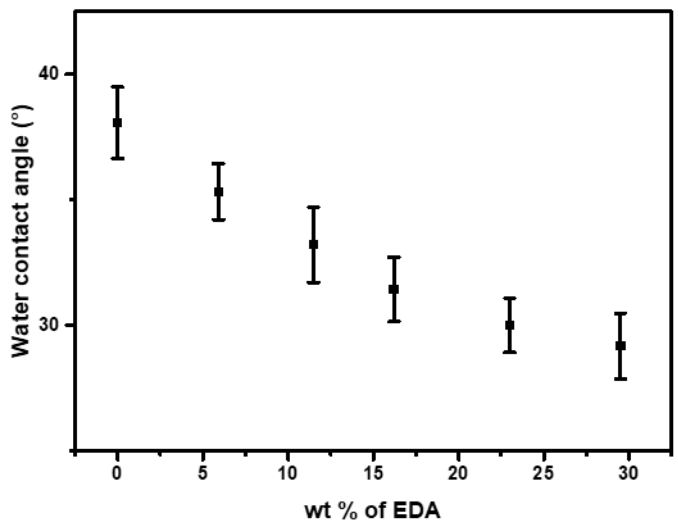

Figure 2-11. Water contact angle dependent on weight percentage of EDA

2.3.3 Electrochemical Measurements

To verify that the amines of EDA promote the HER, the electrochemical measurements were conducted. In Figure 2-12(a), the LSV curves of bare GQD and GQD-5EDA are shown. Under neutral conditions (0.1 M KPF_6), bare GQD produce hydrogen at an overpotential of 470 mV, whereas GQD-5EDA produces hydrogen at an overpotential of 433 mV. As with the HER performance results, bare GQD show lower current density in alkaline solution (0.1 M KOH) than that in neutral solution (0.1 M KPF_6). On the other hand, GQD-5EDA shows higher current density in alkaline solution than that in neutral solution. Significantly, the GQD-5EDA sample shows much higher current density than the bare GQD sample in alkaline solution. Figure 2-12(b) displays Tafel plots of the corresponding LSV curves, which help to analyze the HER mechanism on the surfaces of catalysts. In the case of bare GQD, the Tafel slope in neutral solution is 113 mV per decade, whereas it increases to 162 mV per decade in alkaline solution. On the other hand, the Tafel slope of GQD-5EDA is 107 mV per decade in neutral solution, whereas it decreases to 65 mV per decade in alkaline solution. These results indicate that, in the case of GQD, HER performance decreases under alkaline conditions due to the slow water dissociation step, whereas

in the case of GQD-5EDA, the water dissociation step becomes faster as the pH increases, so that the HER is also promoted. The decreased Tafel slope of GQD-5EDA compared to GQD verifies that the water dissociation step is efficiently facilitated on the surface of GQD-5EDA through EDA functionalization.[40, 41]

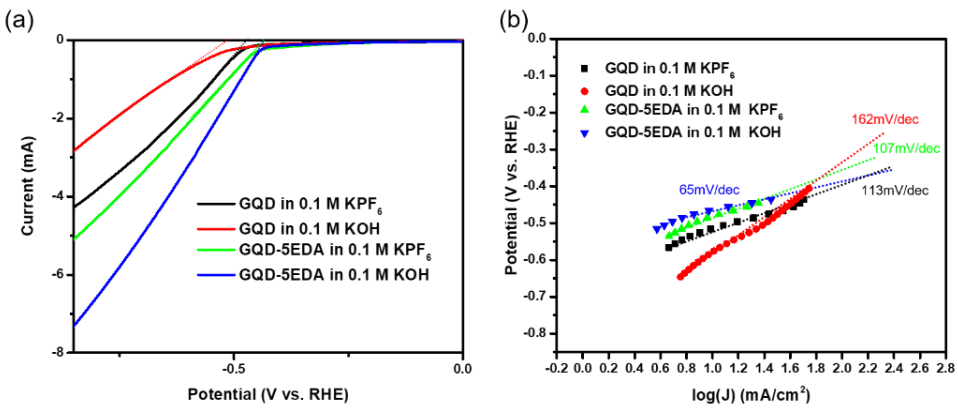

Figure 2-12. (a) LSV curves of GQD and GQD-5EDA. (b) Tafel curves of GQD and GQD-5EDA.

To get further insights into the charge separation properties of GQD, we have also measured the change of charge-transfer resistance of bare GQD and GQD-5EDA by EIS analysis. In Figure 2-13(a) and (b), the Nyquist plot of GQD-5EDA has smaller semicircle radius compared to bare GQD at -0.4 V regardless of the pH condition. It indicates that GQD-5EDA has more efficient charge separation properties and higher charge-transfer rate than bare GQD. In conclusion, the electrocatalytic results obviously demonstrate that

EDA functionalization can significantly facilitate the HER and improve photocatalytic efficiency by providing additional water dissociation sites and promoting charge separation.

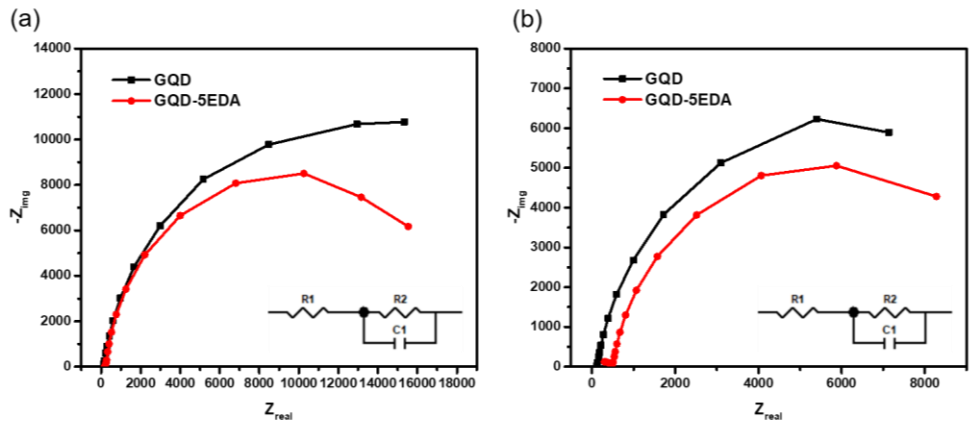

Figure 2-13. Nyquist plots of GQD and GQD-5EDA at -0.4 V (a) in 0.1 M KPF_6 aqueous solution and (b) in 0.1 M KOH aqueous solution.

2.3.4 Fluorescence Lifetime Measurement

To confirm the enhancement of charge separation property, we measured fluorescence lifetimes of GQD and GQD-5EDA at 420 nm emission wavelength. As shown in Figure 2-14(a) and (b), the lifetime of GQD is increased after EDA functionalization regardless of the pH condition. These results indicate that the excited electrons of GQD-5EDA which can be utilized for the water dissociation reaction stay in the excited state longer than those of bare GQD. From these results, it is confirmed that EDA functionalization helps to improve charge separation properties of GQD. In conclusion, the

lifetime results imply that attached EDA distributes to enhanced photocatalytic HER efficiency by assisting charge separation.

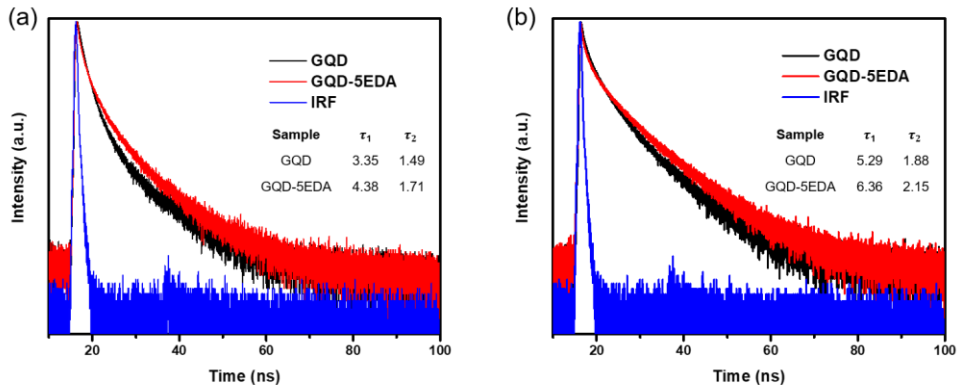

Figure 2-14. Comparison of fluorescence lifetimes between GQD and GQD-5EDA (a) under neutral conditions and (b) under alkaline conditions.

2.3.5 Effect of Amine Sources with Different Chain Lengths on HER Performance of Functionalized GQD

Based on the effect of EDA functionalization on HER performance, it is significant to study the effect of amine group distance from GQD on HER performance. In this study, we prepared three functionalized GQD samples with EDA, 1,4-diaminobutane (BDA), and 1,6-diaminohexane (HDA), respectively. All the synthesis procedures and photocatalytic HER performance measurements were conducted under the same condition. HER performances of functionalized GQD samples are displayed in Figure 2-15. This result clearly reveals that the introduction of the amine group can improve HER

performance regardless of its chain length. Notably, as the chain length increased, HER performance decreased and GQD-EDA shows higher HER performance than other samples. This result can be interpreted that it becomes more difficult for adsorbed water molecules to receive electrons as they move away from the GQD.

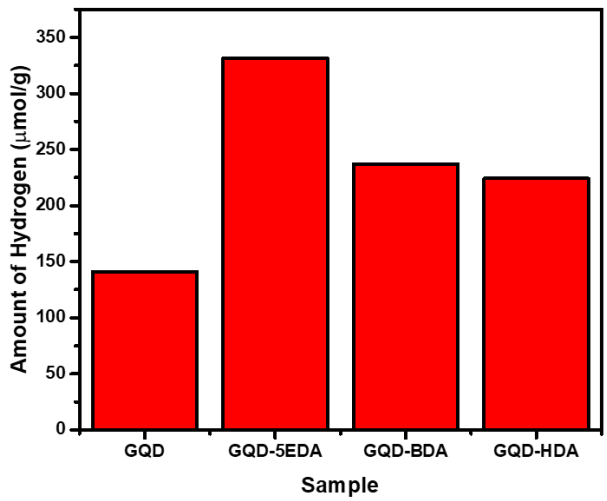

Figure 2-15. Photocatalytic HER performances of GQD-5EDA, GQD-BDA, and GQD-HAD after 10 h of irradiation.

2.4 Conclusion

In conclusion, we successfully synthesized GQD functionalized with EDA by the amide bond formation reaction between carboxyl groups of GQD and amines of EDA. Synthesized GQD-EDA exhibited

enhanced photocatalytic HER performance than bare GQD and peaked HER performance at pH = 10. This result suggests that EDA functionalization clearly increases the photocatalytic efficiency of GQD in alkaline solution. Through the electrochemical measurements, we found that the amines of GQD–EDA act as the water dissociation active sites, which facilitate the entire HER mechanism especially in alkaline solution. Additionally, through electrochemical and fluorescence lifetime measurements, it was found that the charge separation properties were also improved after EDA functionalization. Through these results, we found that EDA functionalization could enhance the photocatalytic HER activity of GQD effectively by introducing additional water dissociation sites. This work demonstrates an easy and promising strategy to design an efficient metal–free photocatalyst material in alkaline solution.

Bibliography

1. Maeda, K.; Domen, K., *The Journal of Physical Chemistry Letters* 2010, *1* (18), 2655-2661.

2. Tachibana, Y.; Vayssieres, L.; Durrant, J. R., *Nature Photonics* 2012, *6* (8), 511-518.

3. Takanabe, K., *ACS Catalysis* 2017, *7* (11), 8006-8022.

4. Jamesh, M.-I.; Sun, X., *Journal of Power Sources* 2018, *400*, 31-68.

5. Yu, J.; Le, T. A.; Tran, N. Q.; Lee, H., *Chemistry - A European Journal* 2020, *26* (29), 6423-6436.

6. Mahmood, N.; Yao, Y.; Zhang, J.-W.; Pan, L.; Zhang, X.; Zou, J.-J., *Advanced Science* 2018, *5* (2), 1700464.

7. Wei, J.; Zhou, M.; Long, A.; Xue, Y.; Liao, H.; Wei, C.; Xu, Z. J., *Nano-Micro Letters* 2018, *10* (4), 75.

8. Danilovic, N.; Subbaraman, R.; Strmcnik, D.; Chang, K.-C.; Paulikas, A. P.; Stamenkovic, V. R.; Markovic, N. M., *Angewandte Chemie International Edition* 2012, *51* (50), 12495-12498.

9. Mahmood, J.; Li, F.; Jung, S.-M.; Okyay, M. S.; Ahmad, I.; Kim, S.-J.; Park, N.; Jeong, H. Y.; Baek, J.-B., *Nature Nanotechnology* 2017, *12* (5), 441-446.

10. Fujishima, A.; Honda, K., *Nature* 1972, *238* (5358), 37-38.

11. Chen, X.; Shen, S.; Guo, L.; Mao, S. S., *Chemical Reviews* 2010, *110* (11), 6503-6570.

12. Yang, Y.; Niu, S.; Han, D.; Liu, T.; Wang, G.; Li, Y., *Advanced*

Energy Materials **2017,** *7* (19), 1700555.

13. Guo, Y.; Park, T.; Yi, J. W.; Henzie, J.; Kim, J.; Wang, Z.; Jiang, B.; Bando, Y.; Sugahara, Y.; Tang, J.; Yamauchi, Y., *Advanced Materials* **2019,** *31* (17), 1807134.

14. Zhao, H.; Li, X.; Cai, M.; Liu, C.; You, Y.; Wang, R.; Channa, A. I.; Lin, F.; Huo, D.; Xu, G.; Tong, X.; Wang, Z. M., *Advanced Energy Materials* **2021,** *11* (31), 2101230.

15. Rahman, M. Z.; Davey, K.; Qiao, S.-Z., *Journal of Materials Chemistry A* **2018,** *6* (4), 1305-1322.

16. Liu, J.; Liu, Y.; Liu, N.; Han, Y.; Zhang, X.; Huang, H.; Lifshitz, Y.; Lee, S.-T.; Zhong, J.; Kang, Z., *Science* **2015,** *347* (6225), 970-974.

17. Mishra, A.; Mehta, A.; Basu, S.; Shetti, N. P.; Reddy, K. R.; Aminabhavi, T. M., *Carbon* **2019,** *149*, 693-721.

18. Elsayed, M. H.; Jayakumar, J.; Abdellah, M.; Mansoure, T. H.; Zheng, K.; Elewa, A. M.; Chang, C.-L.; Ting, L.-Y.; Lin, W.-C.; Yu, H.-h.; Wang, W.-H.; Chung, C.-C.; Chou, H.-H., *Applied Catalysis B: Environmental* **2021,** *283*, 119659.

19. Han, C.; Dong, P.; Tang, H.; Zheng, P.; Zhang, C.; Wang, F.; Huang, F.; Jiang, J.-X., *Chemical Science* **2021,** *12* (5), 1796-1802.

20. Bacon, M.; Bradley, S. J.; Nann, T., *Particle & Particle Systems Characterization* **2014,** *31* (4), 415-428.

21. Ghaffarkhah, A.; Hosseini, E.; Kamkar, M.; Sehat, A. A.; Dordanihaghighi, S.; Allahbakhsh, A.; van der Kuur, C.; Arjmand, M., *Small* **2022,** *18* (2), 2102683.

22. Konstantatos, G.; Badioli, M.; Gaudreau, L.; Osmond, J.; Bernechea, M.; de Arquer, F. P. G.; Gatti, F.; Koppens, F. H. L., *Nature Nanotechnology* 2012, *7* (6), 363-368.

23. Tetsuka, H.; Asahi, R.; Nagoya, A.; Okamoto, K.; Tajima, I.; Ohta, R.; Okamoto, A., *Advanced Materials* 2012, *24* (39), 5333-5338.

24. Yeh, T.-F.; Teng, C.-Y.; Chen, S.-J.; Teng, H., *Advanced Materials* 2014, *26* (20), 3297-3303.

25. Dinda, D.; Park, H.; Lee, H.-J.; Oh, S.; Park, S. Y., *Carbon* 2020, *167*, 760-769.

26. Yang, J.; Miao, H.; Jing, J.; Zhu, Y.; Choi, W., *Applied Catalysis B: Environmental* 2021, *281*, 119547.

27. Chung, S.; Revia, R. A.; Zhang, M., *Advanced Materials* 2021, *33* (22), 1904362.

28. Gao, W.; Gou, W.; Zhou, X.; Ho, J. C.; Ma, Y.; Qu, Y., *ACS Appl Mater Interfaces* 2018, *10* (2), 1728-1733.

29. Zhou, F.; Tien, H. N.; Dong, Q.; Xu, W. L.; Li, H.; Li, S.; Yu, M., *Journal of Membrane Science* 2019, *573*, 184-191.

30. Zhao, B.; Bai, T., *Carbon* 2019, *144*, 481-491.

31. Cho, K. M.; Kim, K. H.; Park, K.; Kim, C.; Kim, S.; Al-Saggaf, A.; Gereige, I.; Jung, H.-T., *ACS Catalysis* 2017, *7* (10), 7064-7069.

32. Deng, B.; Wang, D.; Jiang, Z.; Zhang, J.; Shi, S.; Jiang, Z.-J.; Liu, M., *Carbon* 2018, *138*, 169-178.

33. Li, H.; Wang, P.; Yi, X.; Yu, H., *Applied Catalysis B: Environmental* 2020, *264*.

34. Marcano, D. C.; Kosynkin, D. V.; Berlin, J. M.; Sinitskii, A.; Sun, Z.; Slesarev, A.; Alemany, L. B.; Lu, W.; Tour, J. M., *ACS Nano* **2010,** *4* (8), 4806-4814.

35. Peng, J.; Gao, W.; Gupta, B. K.; Liu, Z.; Romero-Aburto, R.; Ge, L.; Song, L.; Alemany, L. B.; Zhan, X.; Gao, G.; Vithayathil, S. A.; Kaipparettu, B. A.; Marti, A. A.; Hayashi, T.; Zhu, J.-J.; Ajayan, P. M., *Nano Letters* **2012,** *12* (2), 844-849.

36. Ederer, J.; Janoš, P.; Ecorchard, P.; Tolasz, J.; Štengl, V.; Beneš, H.; Perchacz, M.; Pop-Georgievski, O., *RSC Advances* **2017,** *7* (21), 12464-12473.

37. Zeng, M.; Li, Y., *Journal of Materials Chemistry A* **2015,** *3* (29), 14942-14962.

38. Wang, S.; Wang, J.; Zhang, W.; Ji, J.; Li, Y.; Zhang, G.; Zhang, F.; Fan, X., *Industrial & Engineering Chemistry Research* **2014,** *53* (33), 13205-13209.

39. Li, Z.; Zabihi, O.; Wang, J.; Li, Q.; Wang, J.; Lei, W.; Naebe, M., *RSC Advances* **2017,** *7* (5), 2621-2628.

40. Shinagawa, T.; Garcia-Esparza, A. T.; Takanabe, K., *Scientific Reports* **2015,** *5* (1), 13801.

41. Wang, X.; Xu, C.; Jaroniec, M.; Zheng, Y.; Qiao, S.-Z., *Nature Communications* **2019,** *10* (1), 4876.

Chapter 3. Amphiphilic graphene quantum dots as HER photocatalyst via encapsulation of TADF photosensitizer

3.1 Introduction

Currently, finding renewable and environmentally friendly energy sources is a crucial issue in relation to global energy demand. Hydrogen energy is one of the promising candidates as a clean energy source. However, hydrogen energy is now commonly produced from fossil fuels such as natural gas, coal, and petroleum. However, there are several problems such as CO_2 emission and environmental pollution in the process of their combustion. To solve these problems, it is important to develop a strategy to utilize solar energy, an infinite and eco-friendly energy source. Photocatalytic hydrogen evolution reaction (HER) is one of the most promising pathways to convert solar energy into hydrogen energy.[1-3] In this regard, metal-based materials, including metal oxides, sulfides, and phosphides, have been studied as photocatalysts over the past few decades since the first study of a TiO_2-based photoelectrochemical

cell demonstrated by Fujishima and Honda in 1972.[4-8] However, these materials have several limitations, such as fast charge recombination, toxicity and instability, which encourage researchers to develop carbon-based photocatalysts for HER which is earth-abundant and have high stablity.[9-12]

After the discovery of graphene in 2004, graphene quantum dots (GQDs) have been studied extensively in recent years, focusing on their potential as metal-free HER photocatalysts due to their unique properties such as bandgap tunability, stability, and various functionalizations.[13, 14] GQDs are graphene nanoparticles with few-nanometer diameter which have excellent stability and water dispersibility due to oxygen-containing moieties such as carboxyl, carbonyl, and hydroxyl groups. Unlike graphene, graphene quantum dots are semiconductors with an open bandgap and have the potential to be used in various applications including HER.[15-18] For examples, in our recent work, we demonstrated ethylenediamine-functionalized GQD as an efficient photocatalyst material for alkaline HER.[18] We have covalently attached ethylenediamine to GQD by amide bond formation reaction. In contrast to bare GQD, the synthesized material showed increased HER performance (6.21% of AQY at pH=10) as the pH increased. We have confirmed that the remaining primary

amines could adsorb water molecules efficiently which helps to accelerate the water dissociation step. Despite these advantages and potential, GQDs have seriously been limited for photocatalytic HER because of their poor visible light absorption. Whilst dye sensitization has already been established as an effective strategy for enhancing the visible light absorption of catalysts, only few studies have been reported to increase the photocatalytic HER performance of GQDs by introducing organic dyes.[19-22] For example, Min et al. demonstrated a photocatalytic HER system using Eosin Y sensitized reduced graphene oxide (RGO) sheets with Pt catalyst which shows apparent quantum yield (AQY) up to 9.3% under visible light irradiation.[19] In our recent work, we successfully designed metal-free photocatalyst with dye-sensitized N, S-doped GQDs and covalently-attached 2,3-diaminophenazine. This system exhibited efficient HER performance (maximum AQY up to 49% under 400 nm light irradiation).[22] While the dye-sensitization via covalent bonding to GQD showed such encouraging result, it is practically demanded to develop a high efficiency strategy of forming dye-GQD composite nanoparticle by simple mixing of them instead of the covalent bonding as to be shown below. Generally, the neutral core structures of organic dyes are hydrophobic, which induces rapid charge transfer

by forming a complex through aggregation and adsorption to the hydrophobic photocatalysts such as TiO_2 in hydrophilic solvents.[23, 24] However, since GQD nanoparticle has hydrophilic surface, it is difficult to have close interaction with hydrophobic organic dyes, which leads to low stability and slow charge transfer in hydrophilic solvents. To solve this problem, it is necessary to adopt effective strategies to stabilize the organic photosensitizer such as the use of surfactant in hydrophilic solvents.[25–28] For example, Zhu, et al. demonstrated photocatalytic HER system utilizing noncovalently functionalized graphene nanocomposite of porphyrin with the assistance of cetyltrimethylammonium bromide (CTAB) surfactant. Addition of CTAB to the sample, the photocatalytic performance and stability were notably enhanced compared with the sample without CTAB, indicating that surfactant can effectively stabilize the nanocomposite by forming aggregates during the photocatalytic reaction.[25] In this study, we synthesized highly balanced amphiphilic GQD through HA functionalization based on several previous reports,[29, 30] so that GQD could act as photocatalyst and dye-templating surfactant at the same time. We confirmed that the synthesized GQD-HA can form several hundred-nanometer sized composite nanoparticles with a novel TADF organic photosensitizer

in hydrophilic solvents, which showed efficient HER performance under visible light irradiation. Notably, compared to bare GQD, GQD-HA formed more stable nanoparticles and showed remarkably improved HER performance. We also confirmed that amide linkage between GQD and HA efficiently facilitates electron transfer by passivating charge trap centers in GQD. In this work, we synthesized a novel donor-acceptor type TADF organic molecule (NAPTPA-2Br) with strong charge transfer character and long excited state lifetime which are favorable for efficient HER performance via electron transfer to the overlying GQD-HA.[31-35] We designed NAPTPA-2Br with triphenylamine donor and CF_3-substituted naphthalimide acceptor which are known for high stability and efficient charge transfer properties.[36-38] Particularly, two bromo groups were introduced to induce heavy atom effect, resulting in triplet state utilization and long excited state lifetime. These properties made the process of electron transfer to GQD-HA occur more frequently, thereby showing high HER performance. As far as we know, this system showed efficient HER performance close to that of state-of-the-art among carbon-based metal-free photocatalysts for HER under visible light irradiation.[22]

3.2 Experimental details

3.2.1 Chemical used

All chemicals were of analytical grade and used without any further purification. Graphite powder was purchased from Sigma-Aldrich. Sulfuric acid (H_2SO_4, 95 wt %), phosphoric acid (H_3PO_4, 85 wt %), hydrogen chloride (HCl, 36 %), hydrogen peroxide (H_2O_2, 30 %), potassium permanganate ($KMnO_4$) and sodium hydroxide (NaOH) were purchased from Samchun Chemical. Sodium nitrate ($NaNO_3$) was purchased from Alfa Aesar. N-hydroxysuccinimide (NHS), 2-morpholin-4-yl ethanesulfonic acid (MES) and hexylamine (HA) were purchased from Sigma-Aldrich. N-(3-dimethylaminopropyl)-N'-ethylcarbodiimide hydrochloride (EDC) was purchased from TCI.

3.2.2 Synthesis of GO

We synthesized GO from graphite with the modified Hummers method following our previously reported paper.[18] 2 g of graphite powder was added to 240 mL of concentrated mixed acids (H_2SO_4: H_3PO_4 = 5:1) and the mixture was stirred. 1 g of $NaNO_3$ was put into the mixture and stirred for 30 min. The temperature of the mixture was lowered with an ice bath, and 6 g of $KMnO_4$ was added gradually. The rate of

addition was controlled thoroughly to keep the temperature below 20 ° C. After that, the ice bath was removed and the temperature was gradually increased to 40 ° C. After 4 h, another 6 g of $KMnO_4$ was added to the mixture at once and the mixture was left at 40 ° C for 12 h. During the reaction, the mixture was gradually turned into a brownish-gray paste. After cooling to room temperature, the mixture was poured into 1 L ice-cold distilled water with stirring followed by the addition of 8 mL of 30% H_2O_2 solution. An immediate color change from brown to light yellow was observed. The yellow precipitate was left for precipitation. Then, the precipitate was washed with 1 L of 10% HCl solution and then with 2 L of distilled water to remove the unreacted reagents. Finally, the golden viscous GO was suspended in distilled water and stored for further use.

3.2.3 Synthesis of GQD

We have used as-synthesized GO for the synthesis of GQD. We have taken 20 mL (3.5 mg/mL) of GO solution in a beaker and diluted it by adding 60 mL of distilled water. The mixture was sonicated for 30 min for homogeneous dispersion. Then, the pH of the mixture was adjusted to 8~9 by adding 2 N NaOH solution and was sonicated for 1 h. The mixture was moved to a Teflon-lined autoclave and was

treated at 200 ° C for 16 h for hydrothermal synthesis. After cooling to room temperature, the filtrate solution was collected through 0.2 μm Millipore membrane filter and was dialyzed by 1KDa dialysis tube for 3 days. The solution was dried and yellow powder was collected.

3.2.4 Synthesis of GQD-HA

We have covalently attached HA to the carboxyl groups of GQD via amide coupling reaction to synthesize GQD-HA. For this, 4 mg of synthesized GQD was dissolved in 40 mL of distilled water. Next, 70 mg of MES was dissolved in it to maintain pH 6 during the reaction and stirred for 30 min. Then, 65 mg of EDC and 60 mg of NHS were added to it in sequence and stirred for 1 h in the dark. Then, different amounts of HA (50, 100, 150 and 200 μL) were added to the solution and left for 24 h in dark for amide bond formation reaction. Next, unreacted reagents were removed by dialyzing the solution in 1KDa dialysis tube for 3 days.

3.2.5 Synthesis of NAPTPA-2Br

NAPTPA-2Br was synthesized in a 2-step reaction. Suzuki coupling of 2-[3,5-bis(trifluoromethyl)phenyl]-6-bromo-1H-benzo[de]isoquinoline-1,3(2H)-dione (1) and 4-

(diphenylamino)phenylboronic acid gave compound 2, which was subsequently brominated with two equivalents of N-bromosuccinimide to form NAPTPA-2Br in a 70 % overall yield. The detailed synthesis procedure and structural identification of NAPTPA-2Br is described as below.

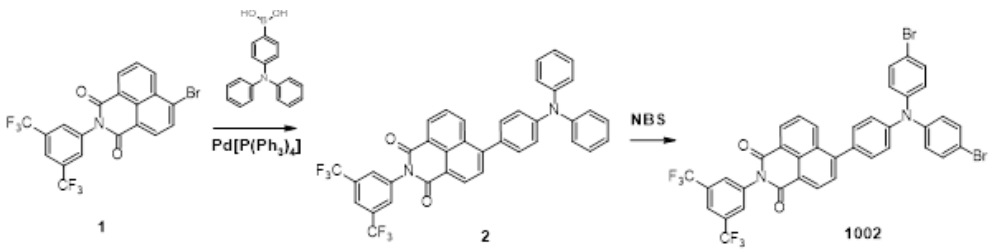

Scheme 3-2. Synthesis of NAPTPA-2Br

6-[4-(Diphenylamino)phenyl]-2-[3,5-bis(trifluoromethyl)phenyl]-1H-benzo[de]isoquinoline-1,3(2H)-dione (2) : To a mixture of 6-bromo-2-[3,5-bis(trifluoromethyl)phenyl]-1H-benzo[de]isoquinoline-1,3(2H)-dione (1, 490 mg, 1 mmol), 4-(diphenylamino)phenylboronic acid (350 mg, 1.2 mmol), potassium carbonate (750 mg) was dissolved in 10 mL of THF/water solution (4/1, v/v). The reaction flask was backfilled with argon three times, $Pd[P(Ph_3)]_4$ (35 mg, 0.03 mmol) was added under argon flow and the resulting mixture was stirred under argon at 60° C for 10h. Reaction mixture was diluted with

water, extracted with dichloromethane, and purified by silica gel column chromatography eluting with $CHCl_3$/n-hexane (1/1, v/v) to obtain title compound as orange solid in 76% yield (600 mg). 1H NMR (500 MHz, $CDCl_3$, δ): 7.11 (t, J=7.2 Hz, 2H), 7.20-7.25 (m, 6 H), 7.30-7.37 (m, 4 H), 7.41 (dd, J=8.7 Hz, 2 H), 7.66-7.83 (m, 2 H), 7.84 (s, 2 H), 8.00 (s, 1 H), 8.53 (dd, J=8.5 Hz, J=1.1 Hz, 1 H), 8.66-8.72 (m, 2 H); MALDITOF-MS: m/z: calcd for $C_{38}H_{22}F_6N_2O_2$ 653.2 $[M+H]^+$, found 653.4.

6-{4-[bis(4-bromophenyl)amino]phenyl}-2-[3,5-bis(trifluoromethyl)phenyl]-1H-benzo[de]isoquinoline-1,3(2H)-dione (NAPTPA-2Br) : A mixture of 1 (65 mg, 0.1 mmol) and N-bromosuccinimide (39 mg, 0.22 mmol) in $CHCl_3$ (0.5 mL) was stirred for 10h at room temperature in the absence of light. The solution was concentrated and MeOH was added to the residue. The precipitated solid was filtered, washed and purified by silica gel column chromatography eluting with $CHCl_3$/n-hexane (1/1). Yellow solid (73 mg, yield 91%). 1H NMR (500 MHz, $CDCl_3$, δ): 7.11 (m, 4 H), 7.20-7.25 (d, 2 H), 7.42 (m, 6 H), 7.75-7.83 (m, 2 H), 7.85 (s, 2 H), 8.00 (s, 1 H), 8.48 (dd, J=8.5 Hz, J=1.0 Hz, 1 H), 8.66-8.72 (m, 2 H)… MALDITOF-MS: m/z: calcd for $C_{38}H_{20}Br_2F_6N_2O_2$ 810.0 $[M+H]^+$, found 808.1.

3.2.6 Characterizations of the material

We have characterized synthesized GO, GQD, and GQD-HA through different spectroscopic and structural analyses. Fourier transform infrared spectroscopy (FTIR) was obtained by Nicolet iS50 (Thermo Fisher Scientific). X-ray photoelectron spectroscopy (XPS) was conducted through AXIS-His (KRATOS) systems. Raman spectroscopy was performed by LabRAM HR Evolution (HORIBA). X-Ray Diffractometer (XRD) data were measured by using D8 Advance (Bruker) with a diffractometer equipped with CuKα (λ = 1.5418 Å) radiation. JEM-2100F High-Resolution TEM and JEM-ARM200F Cs corrected TEM with Cold FEG were used for morphological analysis. UV-Vis absorption and photoluminescence measurements were carried out through Shimadzu UV-1650 PC and Varian Cary spectrophotometer. The evaluation of hydrophilicity of our synthesized GQD and GQD-HA was analyzed by contact angle measurements using a Drop Shape Analyzer DSA 25 (Krüss GmbH). Deionized water (1.8 μL) was dropped at three points of the sample and the average contact angle was calculated. Measurements were conducted immediately after treatment. Fluo Time 200 spectrometer (Pico Quant) equipped with a PicoHarp300 TCSPC board and a

PMA182 photomultiplier was used for fluorescence lifetime measurements. Electrophoretic light scattering (ELS) analysis for zeta potential and size measurements were carried out through ELS Z-100 (Otsuka Portal).

3.2.7 Photocatalytic HER experiments

We have done all the photocatalytic HER measurements with Agilent 7890A gas chromatography. 1 mg of bare GQD and GQD-HA composite were used as HER photocatalyst and 0.5 mg of NAPTPA-2Br was used as photosensitizer. 0.5 mL of triethylamine (TEA) was added as sacrificial reagents. Distilled water and THF were mixed 4:1 to maintain a total volume of 13 mL. Samples were placed in a 40 mL vial sealed with a Teflon septum and continuously purged with 5 sccm of argon gas. Hydrogen evolution rate was measured every 30 minutes of visible light irradiation; the vial was connected to the GC column via Tygon tube and the gas in the vial continuously flew into the GC column for a few seconds. The amount of hydrogen evolved in the gas during that time was calculated by a thermal conductivity detector (TCD). The exact amount of hydrogen was determined by the calibration value obtained by measuring the calibration gas (0.1 mol% of H_2 in Ar). Samples were irradiated with 300 W xenon lamp

with 400 nm cut-off filter. We have measured the amount of evolved hydrogen gas through Agilent 7890A gas chromatography (equipped with a thermal conductivity detector and a 5 Å molecular sieve column). The apparent quantum yield (AQY) was calculated according to the following equation:

$$AQY(\%) = \frac{number\ of\ reacted\ electrons}{number\ of\ incident\ photons} \times 100$$

$$= \frac{number\ of\ evolved\ H_2\ molecules \times 2}{number\ of\ incident\ photons} \times 100$$

3.2.8 Photoelectrochemical measurements

All the electrochemical measurements were carried out by Vertex.One (Ivium technology) electrochemical analyzer using standard three electrode system. We have used GQD or GQD-HA materials as the working electrode by drop casting them over ITO-coated polyethylene terephthalate (PET) plates. We used 0.1 M KPF_6 aqueous solution as the supporting electrolyte for linear sweep voltammetry (LSV) measurement electrochemical impedance spectroscopy (EIS). Ag/AgCl and Pt wire were used as reference and counter electrodes.

3.3 Results and discussion

3.3.1 Characterizations of GQD-HA

First, we have confirmed the successful formation of GQD after hydrothermal treatment to GO by characterizing a change of the structural and spectroscopic properties of GO and GQD. We have conducted several analyses including HR-TEM, Raman, and XPS. GO and GQD have been clearly analyzed as previously published in detail.[13, 39] First, we confirmed the 2D sheet-like morphology of synthesized GO as shown in Figure 3-1(a). In addition, in Figure 3-1(b) and 1(c), (1120) in-plane lattice structure of GQD was clearly confirmed and the average size distribution of synthesized GQD was 4~6 nm.

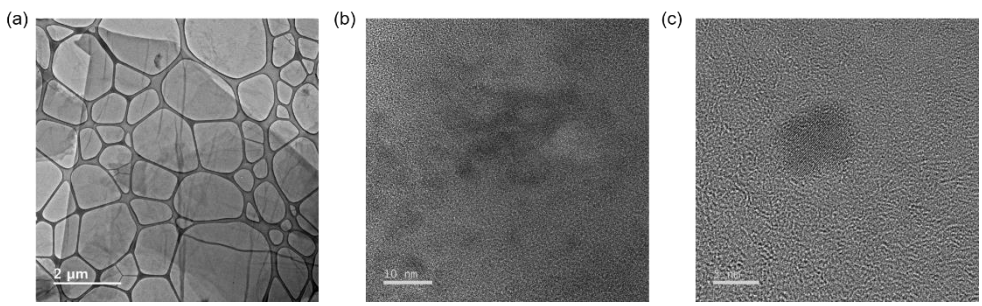

Figure 3-1. TEM image of (a) synthesized GO and (b), (c) synthesized GQD.

Further, we have confirmed the physical properties of our as-synthesized GQD-HA. In the high-resolution TEM (HR-TEM) image of GQD-HA in Figure 3-2(a), we clearly observed the crystal structure with a lattice spacing of 0.24 nm, which indicates the unique (1120) in-plane lattice of graphene. In Cs-corrected transmission

electron microscope (Cs-TEM) image of GQD-HA in Figure 3-2(b), we confirmed that the average size of GQD-HA particles is 4~6 nm, almost identical to that of bare GQD. The absence of changes in size and crystal structure suggests that HA functionalization did not significantly affect the physical properties of GQD.

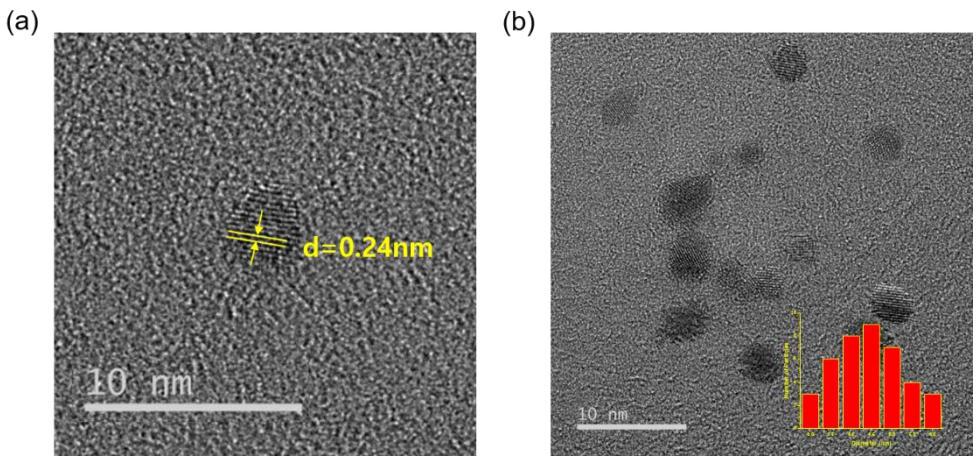

Figure 3-2. TEM images of GQD-HA. (a) HR-TEM image with the crystal lattice and (b) TEM image with particle diameter distribution (inset).

We have analyzed FTIR and XPS spectra of GQD and GQD-HA to confirm the formation of amide bond between GQD and HA after the coupling reaction. From the FTIR spectrum of GQD in Figure 3-3, we have found several peaks at 3440, 1600, and 1086 cm^{-1} which are related to O-H, C=C in-plane aromatic, and C-O stretching vibration.[40] In addition, two additional peaks at 1430 and 605 cm^{-1} were also observed which are corresponding to C-OH stretching and

C-H bending vibrations. In the spectrum of GQD-HA, it was observed that all characteristic peaks of GQD were maintained. Furthermore, we have observed two new peaks at 1630 cm^{-1} corresponding to the amide bond formed between GQD and HA and at 1550 cm^{-1} corresponding to N-H in-plane stretching.

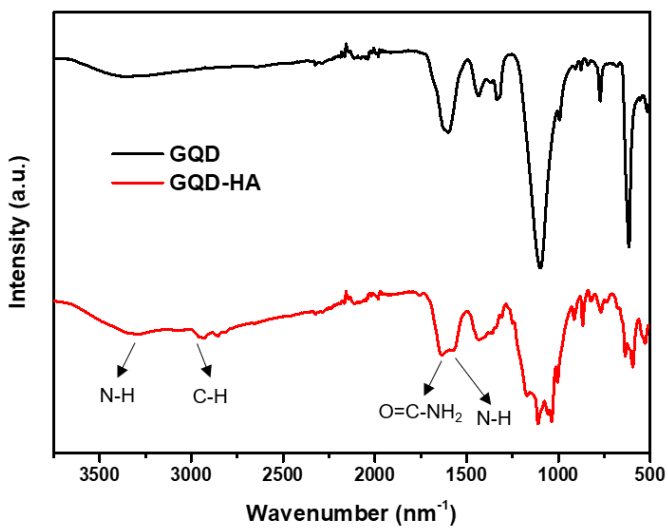

Figure 3-3. FTIR spectra of GQD and GQD-HA

In the XPS spectrum of GQD in Figure 3-4(a), we have observed several characteristic peaks around 284 eV related to carbon and 540 eV related to oxygen. Meanwhile, in the XPS spectrum of GQD-HA in Figure 3-4(a), it is confirmed that a new peak for nitrogen arises at 400 eV in addition to the remaining peaks of GQD. From these FTIR and XPS results, we have clearly confirmed that the amide bond

between GQD and HA is successfully formed after the coupling reaction. Furthermore, we deconvoluted the XPS spectra of GQD and GQD-HA. From the deconvoluted C_{1s} spectrum of GQD in Figure 3-4(b), we can observe C-C, C-O, and C=O peaks. On the other hand, from the deconvoluted C_{1s} spectrum of GQD-HA in Figure 3-4(c), we can observe C-C, C-O, C=O, and C-N peaks. The arisen C-N peak is the evidence of the successful formation of amide linkage after the coupling reaction with HA. In addition, in the deconvoluted spectrum of N_{1s} in Figure 3-4(d), we have observed amine peak (C-NH) at 399.5 eV and amide (HN-C=O) bond peak at 401.5 eV.[41] Particularly, the amide bond peak indicates that GQD-HA is successfully synthesized.

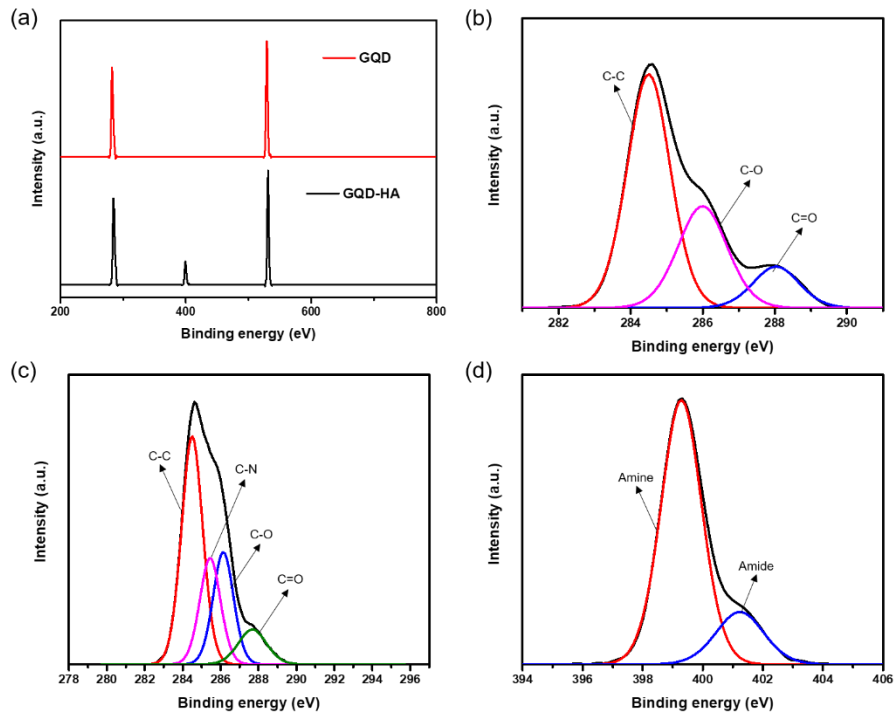

Figure 3-4. (a) Low-resolution XPS spectra of GQD and GQD-HA. High-resolution deconvoluted C_{1s} XPS spectra of (b) GQD, (c) GQD-HA and (d) N_{1s} of GQD-HA.

On the other hand, we have estimated the actual amount of attached HA by calculating the peak area of nitrogen. Calculation was carried out as follows: We assumed that number of attached HA = n, Weight of HA =101n (ignoring Hydrogen atoms). HA contains n of nitrogen atoms and 6n of carbon atoms (Total 7n of atoms). From the low resolution XPS spectrum of GQD, we observed that carbon : oxygen = 1 : 1. We assumed that number of carbon = x, number of oxygen = x, weight of GQD = x×12+x×16=28x. After EDA attaching, the

total number of atoms increased from 3x to 3x+7n. If the observed atomic percentage of nitrogen = p %, then

$$\frac{n}{3x+7n} = \frac{p}{100}$$

$$\frac{100-7p}{3p} n = x$$

From that,

$$Weight\ of\ GQD\ = 28x = \frac{28 \times (100-7p)}{3p} n$$

From that, we calculated wt% of HA

$$= \frac{303p}{28(100-7p)}$$

When different amounts of HA (50, 100, 150 and 200 μL) was used for synthesis reaction, the actual amount of attached HA was 3.1, 5.0, 6.8 and 8.6 wt% as shown in Figure 3-5.

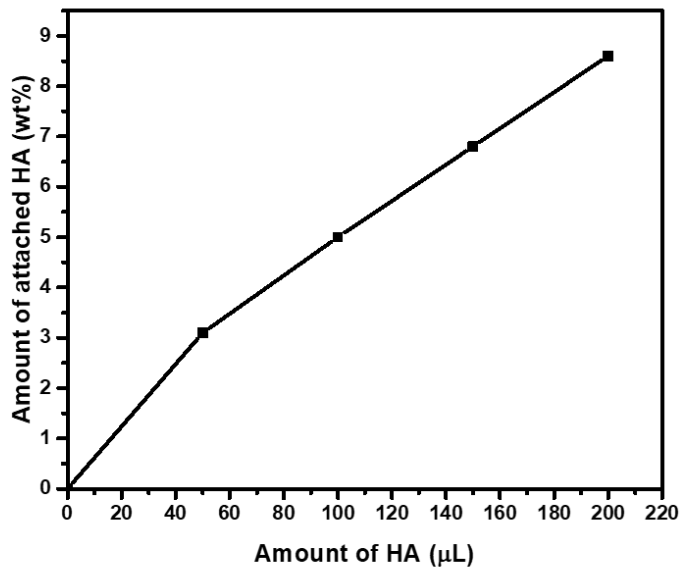

Figure 3-5. Calculated weight percentage of attached HA

We also measured Raman and XRD spectra of GQD and GQD-HA to clarify the change of defect states after HA functionalization(see Figure 3-6 and 3-7). In the Raman spectra in Figure 3-6, we have observed two peaks at 1590 cm^{-1} (G) assigned to the stretching vibration of the sp^2-hybridized carbon atoms in the graphene lattice and at 1350 cm^{-1} (D) assigned to the out-of-plane vibrations of structural defects. By comparing the peak intensity, we could have decided the relative number of defects. The Raman spectrum of GQD-HA (I_D/I_G = 1.033) shows a higher I_D/I_G ratio than GQD (I_D/I_G = 0.975), implying the formation of structural defects after HA functionalization. In the XRD spectra of GQD and GQD-HA in Figure

3-7, we confirmed a broad peak around 24° related to the (002) plane of graphene. Such a breadth of the peak demonstrates that huge amounts of edge sites are established after the synthesis of GQD with small size. However, after HA functionalization, there was no considerable change of the XRD spectrum after HA functionalization, suggesting no noticeable change of the physical properties of GQD.

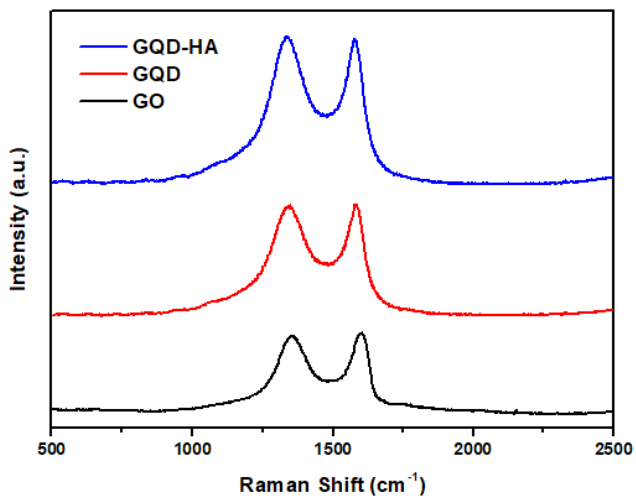

Figure 3-6. Raman spectrum of GO, bare GQD and GQD-HA

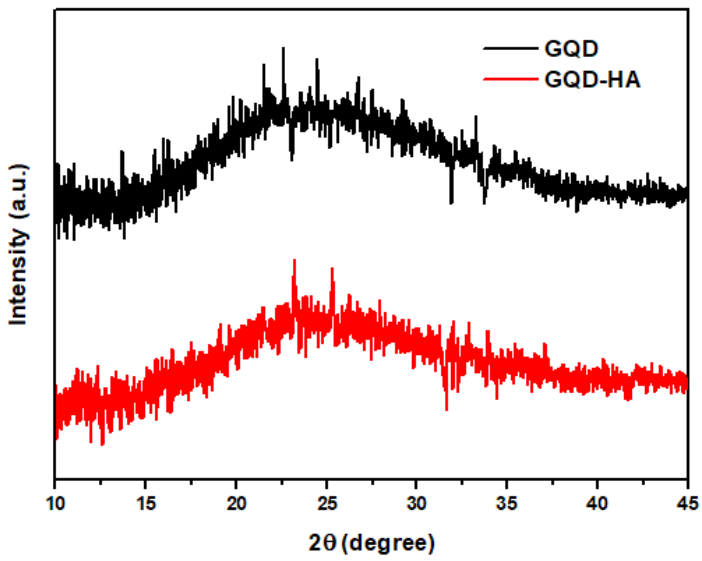

Figure 3-7. XRD spectra of GQD and GQD-HA

In addition, we have measured the water contact angles of GQD and GQD-HA to confirm a change of amphiphilicity after HA functionalization. In Figures 3-8 and 3-9, we confirmed the water contact angle is increased with increasing amounts of attached HA which indicates that the hydrophilicity of GQD significantly decreases by attached hydrophobic alkyl chains of HA after HA functionalization.

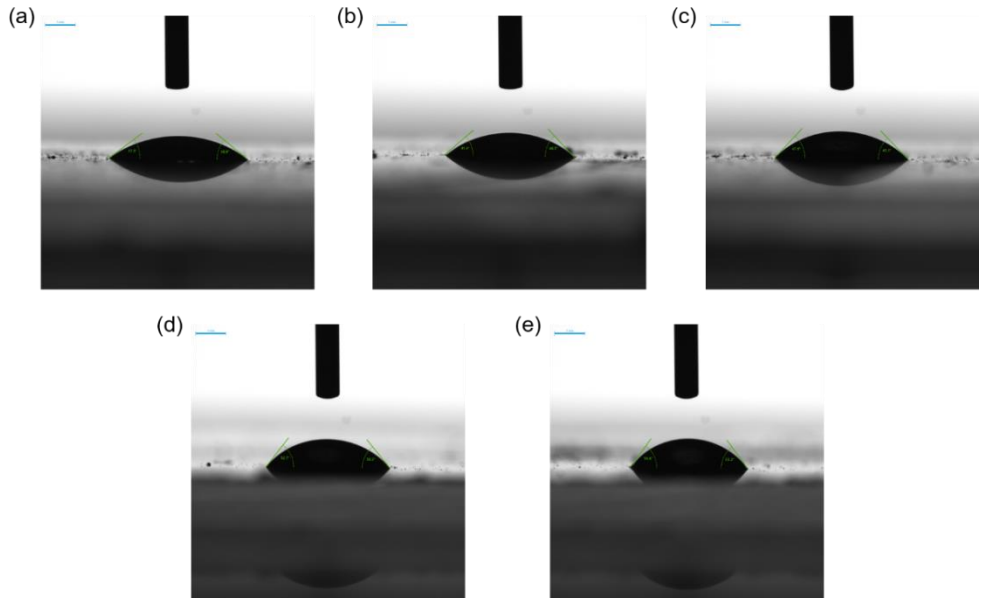

Figure 3-8. Image of water contact angles on (a) bare GQD film, (b) GQD-HA (3.1 wt%), (c) GQD-HA (5.0 wt%), (d) GQD-HA (6.8 wt%) and (e) GQD-HA (8.6 wt%).

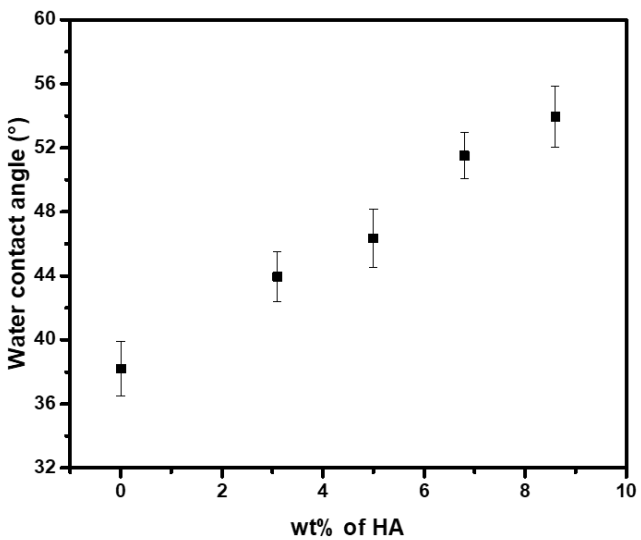

Figure 3-9. Water contact angle dependent on weight percentage of HA

3.3.2 Structural analysis of the photocatalytic system

After HER sample preparation, zeta potential and ELS analysis were performed to determine the size and stability of the formed nanoparticles. Through the zeta potential measurements, we have found that the zeta potential of NAPTPA−2Br without GQD material is −13.8 mV, indicating that NAPTPA−2Br is very unstable in hydrophilic solvents. Meanwhile, the absolute value of the zeta potential significantly increases when GQD material is added to NAPTPA−2Br, indicating that GQD interacts with NAPTPA−2Br and helps to increase the stability in hydrophilic solvents. However, GQD−HA/NAPTPA−2Br nanoparticles have a higher absolute value of zeta potential (−44.62 mV) than GQD/NAPTPA−2Br nanoparticles (−31.51 mV), indicating that GQD−HA can form more stable organic nanoparticles with NAPTPA−2Br than GQD. In addition, as shown in Figure 3−10, the size distribution data obtained through ELS analysis shows that the diameter of nanoparticles formed in the sample with GQD material is about 5 to 10 times smaller than that of the sample without GQD. Notably, the average diameter of GQD−HA/NAPTPA−2Br nanoparticles is twice as small as that of GQD/NAPTPA−2Br nanoparticles. From the results of zeta potential analysis and ELS analysis, we confirmed that more stable and smaller NAPTPA−2Br

nanoparticles can be formed with GQD-HA.

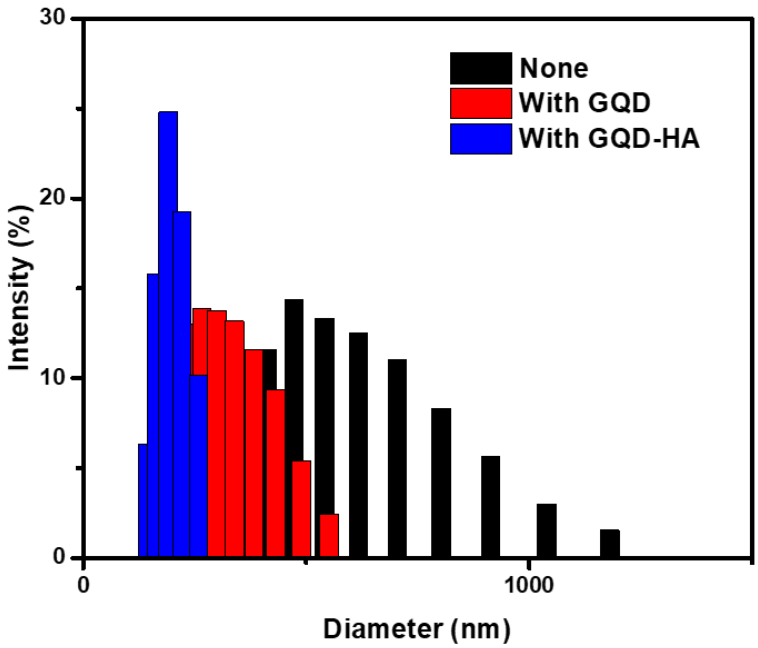

Figure 3-10. Size distribution of NAPTPA-2Br with GQD and GQD-HA

We performed TEM and SEM analysis to verify the morphology of the formed NAPTPA-2Br nanoparticles. As shown in Figure 3-11(a), in the absence of GQD-HA, NAPTPA-2Br has an amorphous sheet structure with a size of 1000 nm or more, whereas when GQD-HA is added, the sample exists as nanospheres with a diameter of about 100 to 200 nm (dark region in Figure 3-11(b)) on lacey carbon grid (bright region in Figure 3-11(b)). Taking a closer look at the dark region as shown in Figure 3-11(c), we observed that multiple

GQD-HA with (1120) crystal lattice are loaded on the NAPTPA-2Br nanoparticles, suggesting the formation of stable nanoparticles via close interaction between GQD-HA and NAPTPA-2Br.

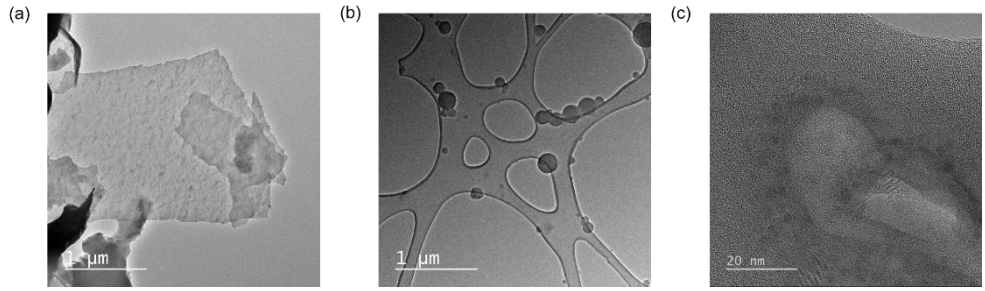

Figure 3-11. TEM images of NAPTPA-2Br (a) without GQD-HA and (b), (c) with GQD-HA on lacey carbon grid

We also observed similar spherical structures of GQD-HA/NAPTPA-2Br through SEM analysis as shown in Figure 3-12.

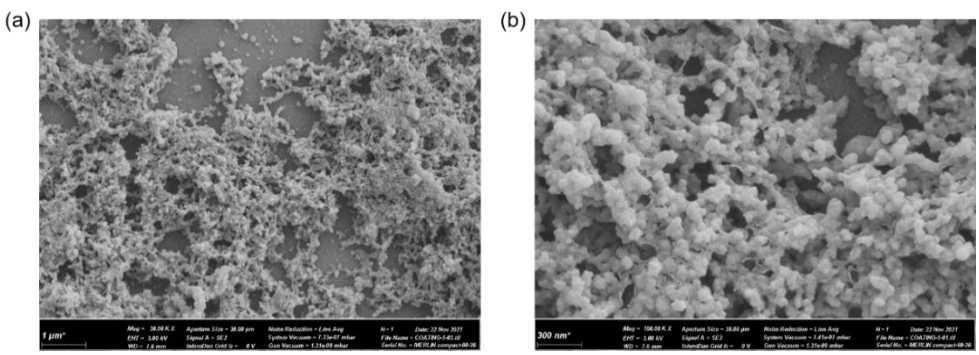

Figure 3-12. SEM image of GQD-HA/NAPTPA-2Br

From these structural analyses, we confirmed that GQD-HA helps

NAPTPA−2Br to form stable spherical nanoparticles. These results can be explained as follows. As the hydrophobic alkyl chain is functionalized on the surface of hydrophilic GQD, the composite becomes amphiphilic. Amphiphilicity of GQD−HA makes it possible to act as a surfactant and form stable micelles by surrounding the hydrophobic organic photosensitizer in hydrophilic solvents.

3.3.3 Photocatalytic HER performance

Composite nanoparticle of GQD−HA with NAPTPA−2Br was evaluated as the HER photocatalyst under visible light (λ > 400 nm) irradiation. We have conducted all the measurements using triethylamine (TEA) as a sacrificial electron donor. As shown in Figure 3−13(a), GQD−HA (with 5.0 wt% of HA)/NAPTPA−2Br shows quite a promising enhancement in HER performance compared to bare GQD/NAPTPA−2Br. On the other hand, the control NAPTPA−2Br sample only GQD material showed no photocatalytic HER, which obviously suggest that the GQD material is acting as a photocatalyst in the system. GQD−HA (with 5.0 wt% of HA)/NAPTPA−2Br shows an initial HER rate of 1.98 mmol/g·h and produces 11.64 mmol/g of hydrogen after 14 hours under visible light irradiation. Our system could produce hydrogen efficiently without

any metal co-catalyst under visible light irradiation compared to previous reports of carbon-based photocatalytic HER systems.[16, 18, 42-49] These results certainly indicate that HA functionalization helps to increase the amount of evolved hydrogen and improve the stability of the HER sample. We also measured the photocatalytic HER performance of NAPTPA-2Br with 5 different GQD-HA samples synthesized with different amounts of HA. In Figure 3-13(b), we confirmed that the HER performance gradually increased with increasing wt% of HA and peaked with 5.0 wt% of HA. Then, it decreased with increasing wt% of HA. If the wt% of HA becomes too high, it is considered that the photocatalytic HER activity decreases due to the decrease in water compatibility as the hydrophilicity of GQD decreases. To confirm the reusability of the photocatalyst, we checked the HER performance for 5 hours under visible light and collected the sample again by vacuum drying. This measurement was repeated 3 times and the results are shown in Figure 3-13(c). After recycling, the sample showed a performance drop from 100% (first run) to 81.6% (third run). These results indicated that our catalyst remained effective and reusable under visible light. In addition, we calculated wavelength dependent apparent quantum yield (AQY) values with the most effective GQD-HA sample to get more insight

into its HER activity. Under 400, 450, and 500 nm light irradiation, they show AQY values of 48.5, 35.7 and 0.5%, respectively, which are in good agreement with the absorption spectrum of NAPTPA-2Br as shown in Figure 3-13(d). All the calculations for AQY are given in the supporting information. Such a high AQY value confirms superior HER activity of GQD-HA/NAPTPA-2Br, which is close to the state-of-the-art.[22] Through these results, we confirmed the high stability of the formed composite nanoparticle and the close interaction between GQD-HA and NAPTPA-2Br lead to the enhanced photocatalytic hydrogen evolution performance. We concluded that amphiphilic GQD-HA could be a promising photocatalyst candidate for an efficient and stable metal-free heterogeneous photocatalytic HER system.

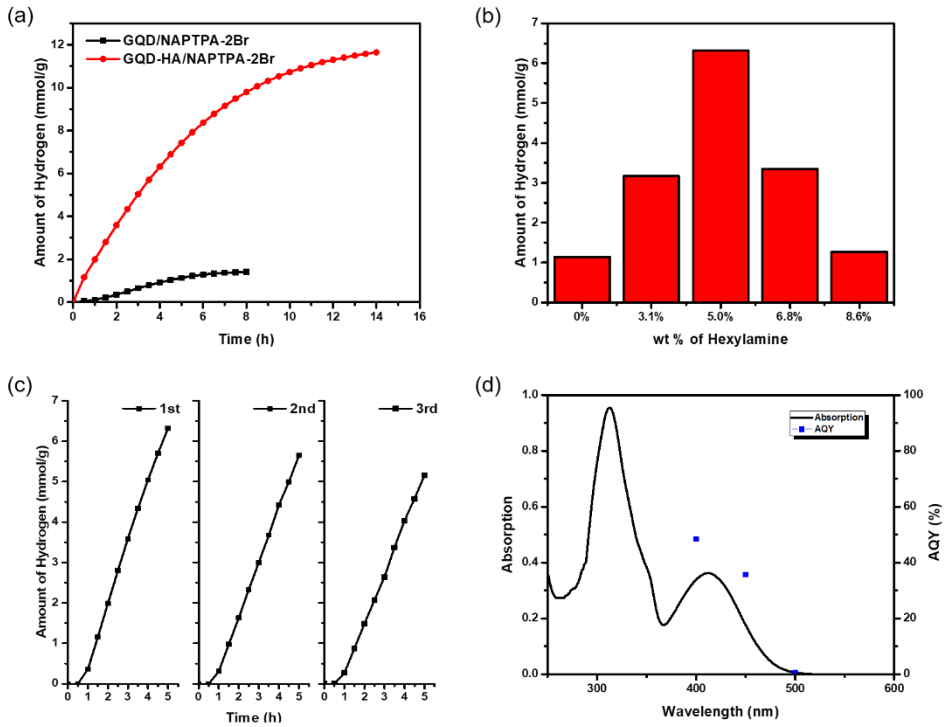

Figure 3-13. (a) Comparison of HER performance between GQD/NAPTPA-2Br and GQD-HA/NAPTPA-2Br, (b) photocatalytic HER performance of the system including GQD-HA with different wt % of HA after 5 h of visible light irradiation, (c) Repeatability test for photocatalytic HER under visible light irradiation, and (d) AQY values of GQD and GQD-HA.

3.3.4 Electrochemical & Photoelectrochemical measurements

We measured several electrochemical measurements with GQD-HA to get a further insight into the modified electrochemical properties of GQD after HA functionalization. We performed linear sweep voltammetry (LSV) measurements and estimated the conduction band (CB) position of the materials from the intercept of linear extrapolation. The CB positions of bare GQD and GQD-HA are found

to be −1.2 V (vs Ag/AgCl) as shown in Figure 3−14(a), which is much higher than the H_2/H_2O redox potential. Notably, GQD−HA exhibits higher current density than the bare GQD. We also confirmed the Mott−Schottky plot of GQD−HA displayed in Figure 3−14(c). Only the p−type semiconductor behavior was found in the Mott−Schottky plot of bare GQD (see Figure 3−14(b)), whereas the n−type semiconductor behavior was observed in the Mott− Schottky plot of GQD−HA. The lack of n−type semiconducting properties in bare GQD is because of the electron trapping property of the carboxyl and hydroxyl groups. After HA functionalization, these trapping sites were efficiently passivated, giving them n−type semiconducting properties. In addition, we compared the charge transfer resistance of bare GQD and GQD−HA through EIS results. In Figure 3−14(d), a semicircle radius of the Nyquist plot of GQD−HA was smaller than that of bare GQD at open circuit voltage condition. From these results, we have found that GQD−HA have enhanced charge separation properties and faster charge transfer rate than bare GQD. This is because covalent functionalization of HA can efficiently passivate electron trapping sites of GQD like carboxylic and hydroxyl groups and restore n−type conductivity. Because fast charge mobility is one of the important factors for efficient HER performance, it can be one

of the reasons for the superior HER performance of GQD-HA. We also measured oxidation potential of NAPTPA-2Br by cyclic voltammetry (CV) measurements as shown in Figure 3-14(e). The measured highest occupied molecular orbital (HOMO) position of NAPTPA-2Br is -5.2 eV and the lowest unoccupied molecular orbital (LUMO) position is -2.61 eV which is evaluated from HOMO and the optical band gap of 2.59 eV. From these results, we drew an electronic band structure for GQD-HA/NAPTPA-2Br nanoparticles regarding the HER mechanism under visible light irradiation as shown in Figure 3-14(f). After visible light absorption by NAPTPA-2Br, the excited electrons are formed and transferred from the LUMO of NAPTPA-2Br to the CB of GQD-HA and holes generated in NAPTPA-2Br are transferred to TEA during the HER mechanism.

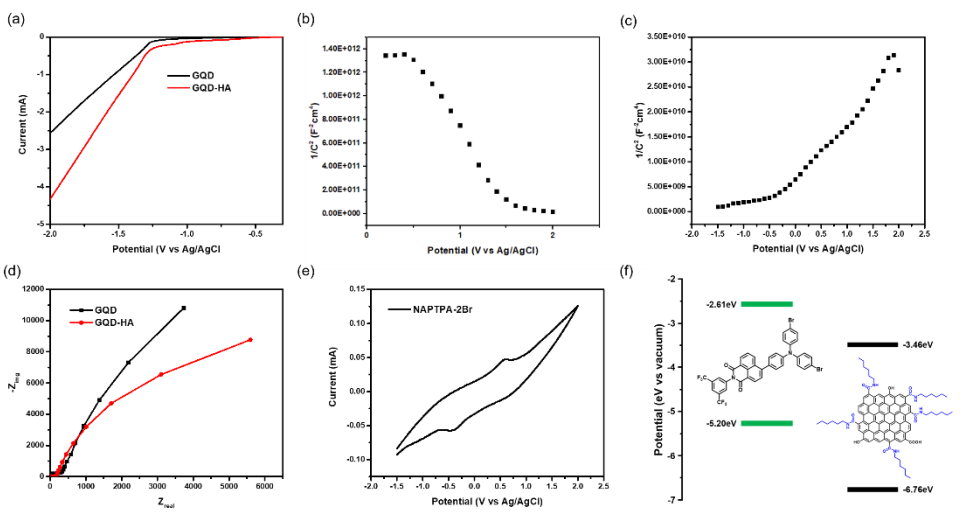

Figure 3-14. (a) LSV curves of GQD and GQD-HA. Mott-Schottky plots of (b) GQD and (c) GQD-HA. (d) Nyquist plots of GQD and GQD-HA. (e) C-

V curve of NAPTPA-2Br. (f) Energy diagram of GQD-HA/NAPTPA-2Br nanoparticles.

In addition, from the fluorescence quenching experiment shown in Figure 3-15 and Figure 3-16, we confirmed the electron transfer mechanism. From Figure 3-15, it is clearly observed that the fluorescence intensity of NAPTPA-2Br does not change after the addition of GQD-HA, which suggests the oxidative electron transfer does not happen. On the other hand, the fluorescence intensity of NAPTPA-2Br is gradually quenched in proportion to the amount of added TEA as shown in Figure 3-16. From these results, we concluded that the reductive quenching mechanism is working in our system. Concisely, electrons in NAPTPA-2Br are first excited by visible light and TEA molecules donate electrons to the excited NAPTPA-2Br molecule making it to radical anion followed by fast electron transfer to the GQD-HA.

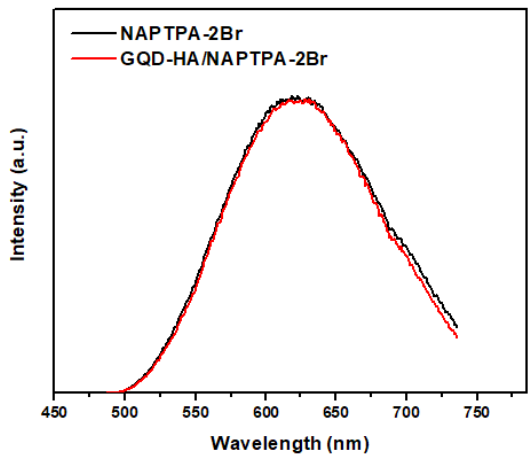

Figure 3-15. Change in photoluminescence of NAPTPA-2Br after addition of GQD-HA.

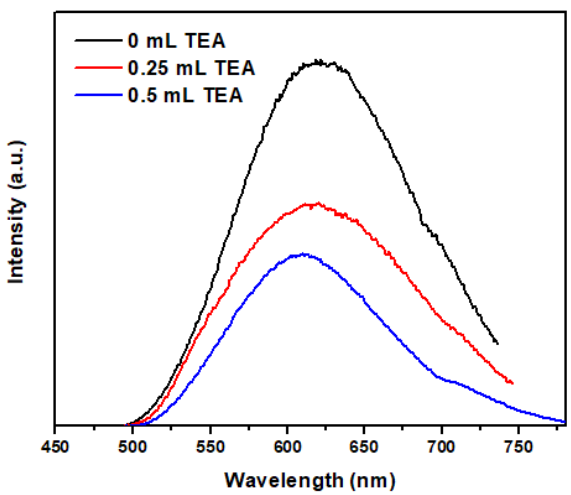

Figure 3-16. Change in photoluminescence of NAPTPA-2Br after gradual addition of TEA.

We also measured electrochemical and photoelectrochemical measurements with GQD/NAPTPA-2Br and GQD-HA/NAPTPA-

2Br nanoparticles to demonstrate the enhanced HER performance after HA functionalization. First, as shown in Figure 3-17(a), we confirmed Nyquist plots of GQD/NAPTPA-2Br and GQDHA/NAPTPA-2Br nanoparticles. Obviously, a semicircle radius of the Nyquist plot of GQD-HA/NAPTPA-2Br was much smaller than that of GQD/NAPTPA-2Br at -0.4 V. It indicates that the charges are separated and transferred more efficiently in GQDHA/NAPTPA-2Br than GQD/NAPTPA-2Br. This result clearly shows that the close interaction between GQD-HA and NAPTPA-2Br induces efficient charge separation and fast charge transfer, resulting in improved photocatalytic HER performance. We also performed transient photocurrent measurements regarding the excellent photocatalytic activity of GQD-HA/NAPTPA-2Br. Transient photocurrent measurements were performed by a conventional three-electrode system using GQD-HA/NAPTPA-2Br film as working electrode under simulated solar light illumination with UV cutoff filter. As shown in Figure 3-17(b), a significant change of photocurrent at zero bias voltage was observed when the illumination was turned on. This noticeable photocurrent response is caused by the photoinduced electron transfer from NAPTPA-2Br to the GQD-HA, which is stable and reproducible under consecutive on-off

cycles of visible light irradiation. Comparing GQD and GQD-HA, it was confirmed that GQD-HA/NAPTPA-2Br showed more than twice the photocurrent density compared to GQD/NAPTPA-2Br, which is consistent with enhanced HER performance. Fast photo-response in GQD-HA/NAPTPA-2Br implies highly efficient charge separation and transfer between GQD-HA and NAPTPA-2Br under visible light irradiation. These results indicate that the amphiphilic GQD-HA helps NAPTPA-2Br to form stable nanoparticles and its photocatalytic HER performance is enhanced due to efficient charge separation and fast charge transfer.

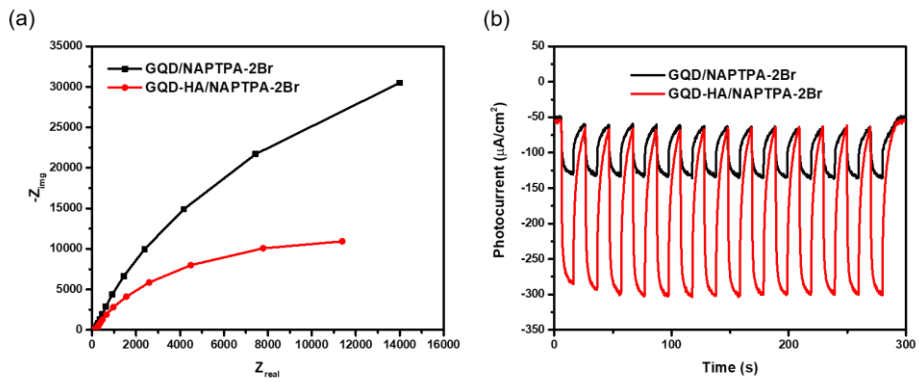

Figure 3-17. (a) Nyquist plots of GQD/NAPTPA-2Br and GQD-HA/NAPTPA-2Br nanoparticles. (b) Transient photocurrent response at zero bias voltage under simulated solar irradiation.

3.4 Conclusion

In conclusion, we have synthesized amphiphilic GQD-HA composite by HA functionalization of GQD via the amide linkage formation

reaction between carboxylic acids of GQD and amines of HA. As clearly confirmed by structural analyses, the synthesized GQD-HA stabilizes NAPTPA-2Br and forms spherical nanoparticles. Compared with GQD, GQD-HA forms more stable nanoparticles with NAPTPA-2Br and GQDHA/NAPTPA-2Br nanoparticles exhibited more stable and enhanced photocatalytic HER performance (with a maximum AQY of 48.5% at 400 nm wavelength) than GQD/NAPTPA-2Br nanoparticles under visible light irradiation. This result suggests that HA functionalization makes GQD amphiphilic, allowing GQD to act not only as a photocatalyst but also as a surfactant. Through electrochemical measurements, we found that charge mobility in GQD is efficiently enhanced after HA functionalization by passivating the electron trapping sites. We also confirmed that the photocatalytic HER performance of GQD-HA/NAPTPA-2Br was improved due to efficient charge separation and fast charge transfer caused by close interaction between GQD-HA and NAPTPA-2Br. Through these results, we concluded that amphiphilic HA functionalized GQD could effectively enhance the stability of hydrophobic organic photosensitizer by forming nanoparticles and it shows remarkably enhanced photocatalytic HER performance. This work suggests a simple and a promising method

to demonstrate an efficient and stable metal-free dye-sensitized photocatalytic HER system in hydrophilic solvents.

Bibliography

1. Tachibana, Y.; Vayssieres, L.; Durrant, J. R., *Nature Photonics* **2012,** *6* (8), 511−518.

2. Takanabe, K., *ACS Catalysis* **2017,** *7* (11), 8006−8022.

3. Pratibha; Kapoor, A.; Rajput, J. K., *International Journal of Hydrogen Energy* **2022,** *47* (40), 17544−17582.

4. Fujishima, A.; Honda, K., *Nature* **1972,** *238* (5358), 37−38.

5. Yang, Y.; Niu, S.; Han, D.; Liu, T.; Wang, G.; Li, Y., *Advanced Energy Materials* **2017,** *7* (19), 1700555.

6. Guo, Y.; Park, T.; Yi, J. W.; Henzie, J.; Kim, J.; Wang, Z.; Jiang, B.; Bando, Y.; Sugahara, Y.; Tang, J.; Yamauchi, Y., *Advanced Materials* **2019,** *31* (17), 1807134.

7. Zhou, K. L.; Wang, Z.; Han, C. B.; Ke, X.; Wang, C.; Jin, Y.; Zhang, Q.; Liu, J.; Wang, H.; Yan, H., *Nature Communications* **2021,** *12* (1), 3783.

8. Liu, Y.; Zheng, X.; Yang, Y.; Li, J.; Liu, W.; Shen, Y.; Tian, X., *ChemCatChem* **2022,** *14* (5), e202101439.

9. Zhou, W.; Jia, T.; Shi, H.; Yu, D.; Hong, W.; Chen, X., *Journal of Materials Chemistry A* **2019,** *7* (1), 303−311.

10. Rahman, M. Z.; Kibria, M. G.; Mullins, C. B., *Chemical Society Reviews* **2020,** *49* (6), 1887−1931.

11. Hu, C.; Dai, Q.; Dai, L., *Cell Reports Physical Science* **2021,** *2* (2), 100328.

12. Elsayed, M. H.; Jayakumar, J.; Abdellah, M.; Mansoure, T. H.;

Zheng, K.; Elewa, A. M.; Chang, C.-L.; Ting, L.-Y.; Lin, W.-C.; Yu, H.-h.; Wang, W.-H.; Chung, C.-C.; Chou, H.-H., *Applied Catalysis B: Environmental* 2021, *283*, 119659.

13. Bacon, M.; Bradley, S. J.; Nann, T., *Particle & Particle Systems Characterization* 2014, *31* (4), 415-428.

14. Ghaffarkhah, A.; Hosseini, E.; Kamkar, M.; Sehat, A. A.; Dordanihaghighi, S.; Allahbakhsh, A.; van der Kuur, C.; Arjmand, M., *Small* 2022, *18* (2), 2102683.

15. Chung, S.; Revia, R. A.; Zhang, M., *Advanced Materials* 2021, *33* (22), 1904362.

16. Yang, J.; Miao, H.; Jing, J.; Zhu, Y.; Choi, W., *Applied Catalysis B: Environmental* 2021, *281*, 119547.

17. Ruiyi, L.; Keyang, H.; Yongqiang, Y.; Haiyan, Z.; Zaijun, L., *Chemical Engineering Journal* 2021, *426*, 130893.

18. Park, H.; Park, S. Y., *ACS Applied Materials & Interfaces* 2022, *14* (23), 26733-26741.

19. Min, S.; Lu, G., *The Journal of Physical Chemistry C* 2011, *115* (28), 13938-13945.

20. Tiwari, A.; Mondal, I.; Pal, U., *RSC Advances* 2015, *5* (40), 31415-31421.

21. Zhang, X.; Peng, T.; Song, S., *Journal of Materials Chemistry A* 2016, *4* (7), 2365-2402.

22. Dinda, D.; Park, H.; Park, S. Y., *Journal of Catalysis* 2021, *404*, 273-282.

23. Han, W.-S.; Wee, K.-R.; Kim, H.-Y.; Pac, C.; Nabetani, Y.; Yamamoto, D.; Shimada, T.; Inoue, H.; Choi, H.; Cho, K.; Kang, S. O., *Chemistry – A European Journal* 2012, *18* (48), 15368-15381.

24. Ding, H.; Xu, M.; Zhang, S.; Yu, F.; Kong, K.; Shen, Z.; Hua, J., *Renewable Energy* 2020, *155*, 1051-1059.

25. Zhu, M.; Li, Z.; Xiao, B.; Lu, Y.; Du, Y.; Yang, P.; Wang, X., *ACS Applied Materials & Interfaces* 2013, *5* (5), 1732-1740.

26. Hansen, M.; Troppmann, S.; König, B., *Chemistry – A European Journal* 2016, *22* (1), 58-72.

27. Li, R.-X.; Liu, X.-F.; Liu, T.; Yin, Y.-B.; Zhou, Y.; Mei, S.-K.; Yan, J., *Electrochimica Acta* 2017, *237*, 207-216.

28. Elsayed, M. H.; Abdellah, M.; Hung, Y.-H.; Jayakumar, J.; Ting, L.-Y.; Elewa, A. M.; Chang, C.-L.; Lin, W.-C.; Wang, K.-L.; Abdel-Hafiez, M.; Hung, H.-W.; Horie, M.; Chou, H.-H., *ACS Applied Materials & Interfaces* 2021, *13* (47), 56554-56565.

29. Cho, H.-H.; Yang, H.; Kang, D. J.; Kim, B. J., *ACS Applied Materials & Interfaces* 2015, *7* (16), 8615-8621.

30. He, J.; Li, Z.; Zhao, R.; Lu, Y.; Shi, L.; Liu, J.; Dong, X.; Xi, F., *Colloids and Surfaces A: Physicochemical and Engineering Aspects* 2019, *563*, 77-83.

31. Lu, J.; Pattengale, B.; Liu, Q.; Yang, S.; Shi, W.; Li, S.; Huang, J.; Zhang, J., *Journal of the American Chemical Society* 2018, *140* (42), 13719-13725.

32. Yu, Z.-J.; Lou, W.-Y.; Junge, H.; Päpcke, A.; Chen, H.; Xia, L.-

M.; Xu, B.; Wang, M.-M.; Wang, X.-J.; Wu, Q.-A.; Lou, B.-Y.; Lochbrunner, S.; Beller, M.; Luo, S.-P., *Catalysis Communications* 2019, *119*, 11-15.

33. Tritton, D. N.; Bodedla, G. B.; Tang, G.; Zhao, J.; Kwan, C.-S.; Leung, K. C.-F.; Wong, W.-Y.; Zhu, X., *Journal of Materials Chemistry A* 2020, *8* (6), 3005-3010.

34. Lee, H.-J.; Kim, J.; Abudulimu, A.; Cabanillas-Gonzalez, J.; Nandajan, P. C.; Gierschner, J.; Lüer, L.; Park, S. Y., *The Journal of Physical Chemistry C* 2020, *124* (13), 6971-6978.

35. Bryden, M. A.; Zysman-Colman, E., *Chemical Society Reviews* 2021, *50* (13), 7587-7680.

36. Kwok, Y.-Y.; Ho, P.-Y.; Wei, Y.; Zheng, Z.; Yiu, S.-C.; Ho, C.-L.; Huang, S., *Chemistry of Materials* 2022, *34* (12), 5522-5534.

37. Tang, G.; Sukhanov, A. A.; Zhao, J.; Yang, W.; Wang, Z.; Liu, Q.; Voronkova, V. K.; Di Donato, M.; Escudero, D.; Jacquemin, D., *The Journal of Physical Chemistry C* 2019, *123* (50), 30171-30186.

38. Masimukku, N.; Gudeika, D.; Volyniuk, D.; Bezvikonnyi, O.; Simokaitiene, J.; Matulis, V.; Lyakhov, D.; Azovskyi, V.; Gražulevičius, J. V., *Physical Chemistry Chemical Physics* 2022, *24* (8), 5070-5082.

39. Marcano, D. C.; Kosynkin, D. V.; Berlin, J. M.; Sinitskii, A.; Sun, Z.; Slesarev, A.; Alemany, L. B.; Lu, W.; Tour, J. M., *ACS Nano* 2010, *4* (8), 4806-4814.

40. Peng, J.; Gao, W.; Gupta, B. K.; Liu, Z.; Romero-Aburto, R.; Ge, L.; Song, L.; Alemany, L. B.; Zhan, X.; Gao, G.; Vithayathil, S. A.;

Kaipparettu, B. A.; Marti, A. A.; Hayashi, T.; Zhu, J.-J.; Ajayan, P. M., *Nano Letters* 2012, *12* (2), 844-849.

41. Ederer, J.; Janoš, P.; Ecorchard, P.; Tolasz, J.; Štengl, V.; Beneš, H.; Perchacz, M.; Pop-Georgievski, O., *RSC Advances* 2017, *7* (21), 12464-12473.

42. Yeh, T.-F.; Syu, J.-M.; Cheng, C.; Chang, T.-H.; Teng, H., *Advanced Functional Materials* 2010, *20* (14), 2255-2262.

43. Latorre-Sánchez, M.; Primo, A.; García, H., *Angewandte Chemie International Edition* 2013, *52* (45), 11813-11816.

44. Lavorato, C.; Primo, A.; Molinari, R.; Garcia, H., *Chemistry - A European Journal* 2014, *20* (1), 187-194.

45. Yeh, T.-F.; Chen, S.-J.; Yeh, C.-S.; Teng, H., *The Journal of Physical Chemistry C* 2013, *117* (13), 6516-6524.

46. Yeh, T.-F.; Teng, C.-Y.; Chen, S.-J.; Teng, H., *Advanced Materials* 2014, *26* (20), 3297-3303.

47. Gliniak, J.; Lin, J. H.; Chen, Y. T.; Li, C. R.; Jokar, E.; Chang, C. H.; Peng, C. S.; Lin, J. N.; Lien, W. H.; Tsai, H. M.; Wu, T. K., *ChemSusChem* 2017, *10* (16), 3260-3267.

48. Chen, L.-C.; Teng, C.-Y.; Lin, C.-Y.; Chang, H.-Y.; Chen, S.-J.; Teng, H., *Advanced Energy Materials* 2016, *6* (22), 1600719.

49. Dinda, D.; Park, H.; Lee, H.-J.; Oh, S.; Park, S. Y., *Carbon* 2020, *167*, 760-769.

Chapter 4. Dye-sensitized amphiphilic graphene quantum dots for visible-light-driven photocatalytic HER in seawater

4.1 Introduction

Hydrogen energy is one of the most promising energy sources to replace fossil fuels, which have many limitations such as environmental pollution and limited reserves, and is receiving a lot of attention because it is a zero-emission energy source with high energy density. The photocatalytic hydrogen evolution reaction (HER) system, which is one of the most environmentally friendly methods for producing hydrogen energy, is a method of converting solar energy, an infinite energy source, into hydrogen energy using a photocatalyst, and a lot of studies has been conducted on this recently.[1-3] However, most of the photocatalytic HER systems studied so far were designed based on freshwater, which accounts for only about 3% of the total water. Considering that a vast amount of water is required to satisfy the vast global energy demand, the use of seawater, which accounts for about 97% of the total water, is an

important issue in large-scale hydrogen production.[4-6] To avoid highly expensive purification and desalination processes to change seawater to freshwater, it is necessary to design a HER system that can produce hydrogen directly from seawater. However, seawater contains large amounts of various ions (Na^+, Mg^{2+}, K^+, Ca^{2+}, Cl^-, and SO_4^{2-}) and impurities (iron, lead, and gold), which could affect the stability and performance of the photocatalytic system.[4, 7] Because seawater is highly corrosive as well, it is difficult to maintain a stable photocatalytic HER system in seawater. Since there have been only few reports of photocatalytic HER systems working stable in seawater, it is important to find novel and stable photocatalysts which are adequately durable for photocatalytic HER in seawater.

After the first demonstration of a photoelectrochemical HER system based on TiO_2 developed by Fujishima and Honda in 1972,[8] most of the photocatalytic HER systems have been studied using metal-based semiconductor materials.[9-13] Although these materials exhibit high performance, their sustainable utilization is limited by rapid charge recombination, toxicity, corrosion and low selectivity. In order to overcome these limitations, it is desirable to find a metal-free photocatalyst that is abundant and eco-friendly.[14-17] From this point of view, many studies have been conducted on catalysts made of

earth-abundant elements for photocatalytic HER. Graphene quantum dots (GQDs) have recently emerged as one of the most promising candidates due to their unique physical and chemical properties. GQDs, actually made of reduced graphene oxide (RGO) quantum dots, are nanoparticles with a size of a few nanometers that are stabilized by having oxygen-containing groups such as carboxyl, hydroxyl, and carbonyl groups on their surface.[18-20] The semiconductor properties and quantum confinement effect induced by open band gap nature allow GQD to be utilized in a variety of applications, including photocatalytic HER.[21-25]

However, limited visible light absorption and also the presence of electron trapping sites on the GQD' s surface attributed to the oxygen-containing functional groups seriously prevent it from having high photocatalytic HER performance. As an innovative strategy to solve these two problems at the same time, we have synthesized GQD with covalently-bonded rhodamine 123 and successfully demonstrated both effects of dye-sensitization and alleviation of electron trapping site. As with other dye-sensitizing strategies in photocatalytic systems,[26-31] an excellent visible light absorption of rhodamine 123 allowed the GQD photocatalysts with high HER performance (maximum HER rate of 0.488 mmol/g · h and

total HER amount of 1.360 mmol/g in 12 hours) under visible light irradiation. We also confirmed through electrochemical and photoelectrochemical measurements that the covalent attachment of rhodamine 123 to GQD via amide bond significantly improved the HER performance by restoring the n-type semiconductor property of GQD by passivating the electron trap sites on the surface of GQD.30 Subsequently, 2,3-diaminophenazine-bonded N,S-doped GQD was used as a metal-free single catalyst to show HER rate of 1.44 mmol/g · h and AQY of 49% under 400 nm light irradiation, which is the state-of-the-art value among carbon-based photocatalytic HER systems.[31] Through these studies, we have originally proposed that the dye-sensitization strategy through amide bonds can be a viable strategy for fabricating highly efficient GQD-based state-of-the-art HER photocatalysts. As an alternative strategy towards high efficiency dye-sensitized GQD system, we synthesized amphiphilic GQD through hexylamine (HA) functionalization (GQD-HA) which can spontaneously assemble with various hydrophobic dyes into composite nanoparticle. It should be noted that the HA functionalization provided trap passivation effect as well as the amphiphilicity. This strategy opened a more convenient pathway of using dye-sensitization without complicated covalent bond formation

reaction. Recently, we could show that the nanoparticles comprising amphiphilic GQD-HAs and organic thermally-activated delayed fluorescence (TADF) photosensitizer showed efficient HER performance (maximum HER rate of 1.98 mmol/g · h and total HER amount of 11.64 mmol/g in 14 hours) under visible light irradiation, which is much improved compared to that of bare GQD.[32] Also, this system showed AQY up to 48.5% under 400 nm light irradiation which is close to the state-of-the-art among carbon-based photocatalytic HER systems.

While all these GQD-based dye-sensitized HER systems are quite efficient in pure water, they unfortunately showed rather inferior HER performance in seawater as other photocatalysts shown in many reported papers.[4, 33-35] We can hypothesize, in principle, that the photocatalytic systems which show enhanced HER performance in the presence of metal halide salts should be most useful in seawater splitting. Among the photocatalysts reported so far,[36-38] we came to note that an ionic amphiphilic octupolar organic molecule (TPATCS) with a Pt co-catalyst showed significant enhancement of HER performance in the presence of halide salts together with a high visible light absorption.[38] Unfortunately, however, the TPATCS photocatalyst alone without Pt co-catalyst barely showed HER

activity (initial rate of 0.044 mmol/g · h and 0.121 mmol/g of hydrogen after 3 hours). Aiming at a metal-free photocatalytic HER system in seawater, in this work, we decided to combine these amphiphilic organic molecule (TPATCS) and amphiphilic GQD-HA. We synthesized amphiphilic GQD-HA by attaching HA through the amide bond. We confirmed that the amphiphilicity of synthesized GQD-HA induces a close interaction with the amphiphilic organic TPATCS and forms a photostable nanostructure. Notably, composite nanostructure showed enhanced HER performance in simulated seawater higher than that in pure water. It produced hydrogen efficiently (initial rate of 0.182 mmol/g · h and 1.303 mmol/g of hydrogen after 15 hours) and showed AQY of 22.5% under 500 nm light irradiation, which is the state-of-the-art value among metal-free photocatalytic HER system in seawater. We also observed that the amide bond between GQD and HA passivates the charge trap centers of GQD, effectively promoting charge separation and transfer.

4.2 Experimental details

4.2.1 Chemicals used

All chemicals were of analytical grade and used without further

purification. Graphite powder was purchased from Sigma-Aldrich. Sulfuric acid (H_2SO_4, 95 wt%), phosphoric acid (H_3PO_4, 85 wt%), hydrogen chloride (HCl, 36 %), hydrogen peroxide (H_2O_2, 30 %), potassium permanganate ($KMnO_4$), and sodium hydroxide (NaOH) were purchased from Samchun Chemical. Sodium nitrate ($NaNO_3$) was purchased from Alfa Aesar. N-hydroxysuccinimide (NHS), 2-morpholin-4-yl ethanesulfonic acid (MES) and hexylamine (HA) were purchased from Sigma-Aldrich. N-(3-dimethylaminopropyl)-N'-ethylcarbodiimide hydrochloride (EDC) was purchased from TCI. 2-(4-bromophenyl)acetonitrile, 4-pyridineboronic acid, Tetrakis(triphenylphosphine)palladium(0) , and iodomethane were purchased from Sigma-Aldrich. Tetrabutylammonium chloride and 4,4',4''-nitrilotribenzaldehyde were purchased from TCI.

4.2.2 Synthesis of graphene oxide (GO)

We have synthesized GO through the modified Hummers method which is reported in our previous paper.[25] 2 g of graphite powder was put into 240 mL of concentrated mixed acids (H_2SO_4: H_3PO_4 = 5:1) and stirred for 30 min. Next, the temperature of the mixture was lowered in an ice bath to maintain the temperature below 20 ° C and 6 g of $KMnO_4$ was gradually added into the mixture. Then, the ice

bath was removed and the temperature of the mixture was gradually raised to 40 ° C in an oil bath. After 4 h, another 6 g of $KMnO_4$ was added at once and the mixture was stirred at 40 ° C for 12 h. After cooling to room temperature, the brownish-gray product was poured into 1 L of stirring ice-cold distilled water with 8 mL of added H_2O_2. An instantaneous color change to light yellow was observed. The mixture was left in a refrigerator for precipitation. Afterwards, the yellow precipitate was washed with 1 L of 10% HCl aqueous solution and then with 2 L of distilled water to clear the unreacted reagents. At last, the golden viscous GO suspended in distilled water (3.5 mg/mL) was collected and stored for further use.

Synthesis of GQD

We have used synthesized GO for the synthesis of GQD. We have taken 30 mL of GO and diluted it to 80 mL with distilled water. The mixture was sonicated for 30 min and the pH of the mixture was adjusted to 8~9 with 2 N NaOH and 2 N HCl solution. After 1 h sonication, the mixture was transferred to a Teflon-lined autoclave and was left at 200 ° C for 16 h for hydrothermal reaction. After cooling to room temperature, the filtrate solution was collected through 0.2 μm Millipore membrane filter and dialyzed by 1KDa

dialysis tube for 3 days. Then, the solution was vacuum-dried and light-yellow powder was collected.

Synthesis of GQD-HA

We have synthesized GQD-HA by covalent attachment of HA to the carboxyl groups of GQD via amide coupling reaction. 4 mg of synthesized GQD was dissolved in 40 mL of distilled water. Next, 70 mg of MES buffer was added into the mixture to maintain pH 6 during the reaction and stirred for 30 min. Then, 65 mg of EDC and 60 mg of NHS were added and stirred for 1 h in the dark. Then, 0.1 mL of HA were added to the solution and stirred for 24 h in dark. Then, the solution was collected and dialyzed by 1KDa dialysis tube for 3 days to remove unreacted reagents.

Synthesis of TPATCS

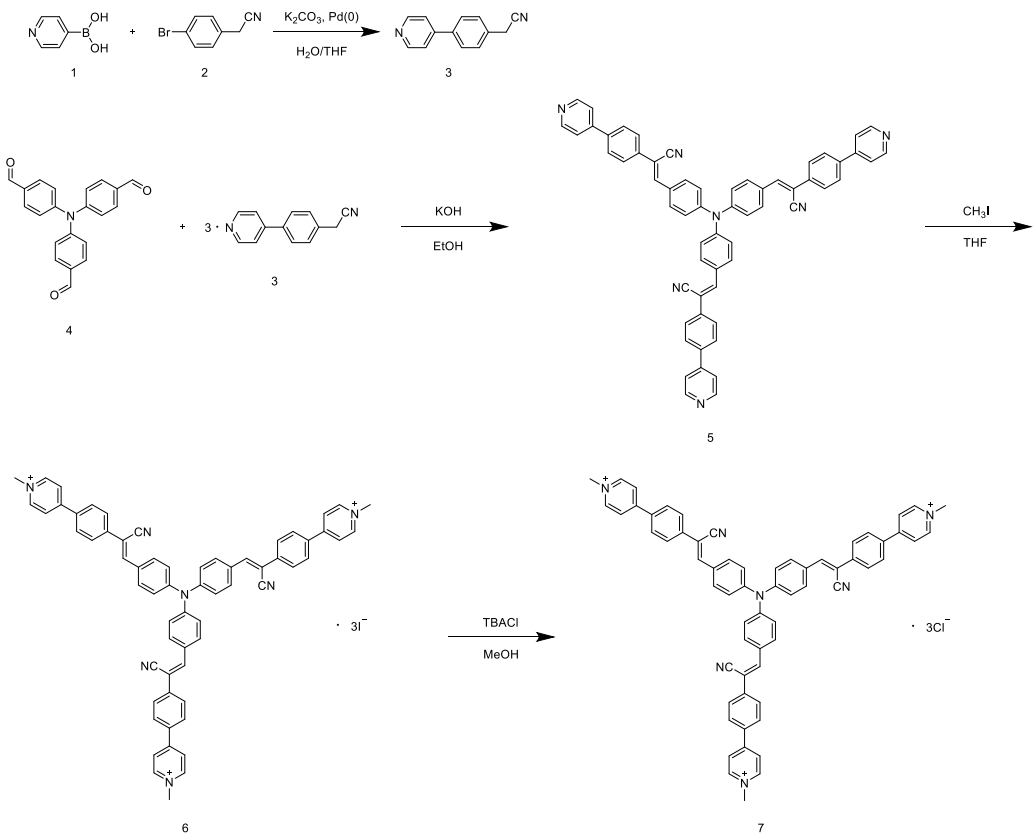

Scheme 4-2 Synthetic route of TPATCS

TPATCS was synthesized as reported previously.[38] Synthetic route was illustrated in Scheme 4-1.

Synthesis of 2-(4-(pyridine-4-yl)phenyl)acetonitrile (3): 2-(4-bromophenyl)acetonitrile (2.66 g, 13.6 mmol) was dissolved in 30 mL of THF, and 4-pyridineboronic acid (2 g, 16.3 mmol) was dissolved in 25 mL of distilled water. K_2CO_3 (7 g, 50 mmol) and 20 mL of ethanol were added in consecutive order. The mixture was stirred and degassed by N_2 purging at 80 °C for 30 mins. Tetrakis(triphenylphosphine)palladium(0) (0.16 g, 0.14 mmol) was

dissolved in 10 ml THF and degassed by N_2 purging for 30 mins. Then it was added to the mixture dropwise. The mixture was stirred overnight at 80 ° C at N_2 atmosphere. The mixture was cooled to room temperature and poured into 200 mL of distilled water. The mixture was extracted with 200 mL of ethyl acetate for three times. Then, hydrophobic layer was collected and remaining water was removed with $MgSO_4$. Final mixture was evaporated and the crude product was collected. The product was purified by using column chromatography (ethyl acetate : hexane = 5 : 5, v/v) and a white crystalline product was obtained. Yield: 2.44 g (93 %). 1H NMR (300 MHz, $CDCl_3$) δ 8.68 (d, J = 4.6 Hz, 2H), 7.66 (d, J = 7.7 Hz, 2H), 7.48 (m, J = 7.4 Hz, 4H), 3.83 (s, 1H)

Synthesis of (2Z,2'Z,2''Z)−3,3',3''−(nitrilotris(benzene−4,1−diyl))tris(2−(4−(pyridin−4−yl)phenyl)acrylonitrile) (5): 3 (0.97 g, 5.01 mmol) and 4,4',4''−nitrilotribenzaldehyde (4, 0.5 g, 1.52 mmol) were dissolved in 10 mL of THF and the solution was poured into 100 mL of ethanol. 0.5 g of potassium hydroxide was dissolved in 50 mL of ethanol, then it was added to the mixture dropwise. The mixture was stirred for 10 mins followed by filtering. The filtrate was washed several times with ethanol and vacuum−dried. Orange crystalline product was obtained. Yield: 0.81 g (63 %). 1H NMR (300

MHz, $CDCl_3$) δ 8.70 (d, J = 5.9 Hz, 2H), 7.94 (d, J = 8.7 Hz, 2H), 7.82 (d, J = 8.4 Hz, 2H), 7.74 (d, J = 8.5 Hz, 2H), 7.58 (s, 1H), 7.55 (d, J = 5.9 Hz, 2H), 7.27 (d, J = 6.3 Hz, 2H).

Synthesis of 4,4',4''-(((1Z,1'Z,1''Z)-(nitrilotris(benzene-4,1-diyl))tris(1-cyanoethene-2,1-diyl))tris(benzene-4,1-diyl))tris(1-methylpyridin-1-ium) iodide (6): 5 (0.4 g, 0.47 mmol) was dissolved in 30 mL of THF, and iodomethane (2 g, 14.1 mmol) was added dropwise. The solution was stirred for 2 days in room temperature. Then the solution was poured into 100 mL of dichloromethane and filtered. The residue was washed with dichloromethane to remove remaining reactants. Red product was obtained and vacuum-dried. Yield: 0.45 g (75 %). 1H NMR (300 MHz, DMSO) δ 9.04 (d, J = 7.1 Hz, 2H), 8.57 (d, J = 6.9 Hz, 2H), 8.25 (m, J = 10.5 Hz, 3H), 8.06 (dd, J = 14.8, 8.7 Hz, 4H), 7.33 (d, J = 8.7 Hz, 2H), 4.35 (s, 3H).

Synthesis of 4,4',4''-(((1Z,1'Z,1''Z)-(nitrilotris(benzene-4,1-diyl))tris(1-cyanoethene-2,1-diyl))tris(benzene-4,1-diyl))tris(1-methylpyridin-1-ium) chloride (7): 6 (0.4 g, 0.31 mmol) was dissolved in 10 ml of DMF, and a 20 ml of methanol solution of tetrabutylammonium chloride (2.58 g, 9.3 mmol) was added dropwise. The solution was stirred for 2 days. After that, the

solution was poured into 100 ml of toluene. Red product was collected by filtration and washed with toluene several times. Yield: 0.26 g (61 %). 1H NMR (300 MHz, MeOD) δ 8.91 (d, J = 6.9 Hz, 2H), 8.46 (d, J = 7.0 Hz, 2H), 8.15 (d, J = 8.7 Hz, 2H), 8.05 (m, J = 11.6, 6.7 Hz, 5H), 7.29 (d, J = 15.9 Hz, 2H), 4.42 (s, 3H).

4.2.3 Characterization of the materials

We have characterized our synthesized GO, GQD, and GQD-HA by using several spectroscopic as well as microstructural analyses. Fourier transform infrared spectroscopy (FTIR) was carried out through Nicolet iS50 (Thermo Fisher Scientific). X-ray photoelectron spectroscopy (XPS) was carried out through AXIS-His (KRATOS) systems. Raman analysis was performed by LabRAM HR Evolution (HORIBA). X-Ray Diffractometer (XRD) analysis was carried out through D8 Advance (Bruker) with a diffractometer equipped with CuKα (λ = 1.5418 Å) radiation. JEM-2100F High-Resolution TEM and JEM-ARM200F Cs corrected TEM with Cold FEG were used for morphological analysis. UV-Vis absorption and photoluminescence measurements were carried out through Shimadzu UV-1650 PC and Varian Cary spectrophotometer. The evaluation of hydrophilicity of our synthesized GQD and GQD-HA

was analyzed by contact angle measurements using a Drop Shape Analyzer DSA 25 (Krüss GmbH). Deionized water (1.8 μL) was dropped at three points of the sample and the average contact angle was calculated. Measurements were conducted immediately after treatment. Fluo Time 200 spectrometer (Pico Quant) equipped with a PicoHarp300 TCSPC board and a PMA182 photomultiplier was used for fluorescence lifetime measurements. Electrophoretic light scattering (ELS) analysis for zeta potential and size measurements were carried out through ELS Z-100 (Otsuka Portal).

4.2.4 Photocatalytic HER experiments

All photocatalytic HER measurements were conducted with an Agilent 7890A gas chromatography equipped with a thermal conductivity detector (TCD). 1 mg of bare GQD and GQD-HA composite were used as the photocatalyst and 0.65 mL of 1mM TPATCS aqueous solution was used as the photosensitizer (0.5 mol). 350 mg of ascorbic acid, a sacrificial reagent, was dissolved in 13 mL of distilled water and the pH was adjusted to 4. Samples were put into a 40 mL vial sealed with a Teflon septum and continuously purged with 5 sccm of argon gas. The vial was connected to the GC column via Tygon tube and the gas in the vial continuously flew into

the GC column. Hydrogen evolution rate was measured every 30 minutes of visible light irradiation and the exact amount of hydrogen was calibrated by measuring the standard gas (0.1 mol% of H_2 in Ar). Samples were irradiated with a 300 W xenon lamp with 420 nm cutoff filter. The apparent quantum yield (AQY) was calculated according to the following equation:

$$AQY(\%) = \frac{number\ of\ reacted\ electrons}{number\ of\ incident\ photons} \times 100$$

$$= \frac{number\ of\ evolved\ H_2\ molecules \times 2}{number\ of\ incident\ photons} \times 100$$

4.2.5 Electrochemical & photoelectrochemical measurements

All the electrochemical and photoelectrochemical measurements were conducted by Vertex.One (Ivium technology) electrochemical analyzer using standard three-electrode system. We have prepared GQD and GQD-HA thin films on ITO-coated polyethylene terephthalate (PET) plates and used them as working electrodes. 0.1 M KPF_6 aqueous solution was used as the supporting electrolyte for linear sweep voltammetry (LSV) measurement electrochemical impedance spectroscopy (EIS). Pt wire and Ag/AgCl were used as counter and reference electrodes, respectively. Oxidation potential of TPATCS was measured by cyclic voltammetry using 0.01 M

$AgNO_3$/Ag as a reference electrode, glassy carbon disc (diameter = 3 mm) as a working electrode and Pt wire as a counter electrode. The redox potential of the reference electrode was calibrated using ferrocenium/ferrocene (Fc^+/Fc) as an internal standard. Here, 0.1 M NBu_4PF_6 in anhydrous acetonitrile was used as the supporting electrolyte. 100 mW/cm^2 solar simulator model PEC L01 was used as the light source for photoelectrochemical measurements.

4.3 Results and discussion

4.3.1 Characterization of the materials

We have characterized our as-synthesized GO and GQD by high-resolution TEM (HR-TEM) to confirm the morphology and successful synthesis. As shown in Figure 4-1, as-synthesized GO showed 2D sheet-like structure with a narrow thickness. After hydrothermal reaction, GQD with a 0.24 nm wide (1120) lattice fringe have been successfully synthesized as shown in Figure 4-2.

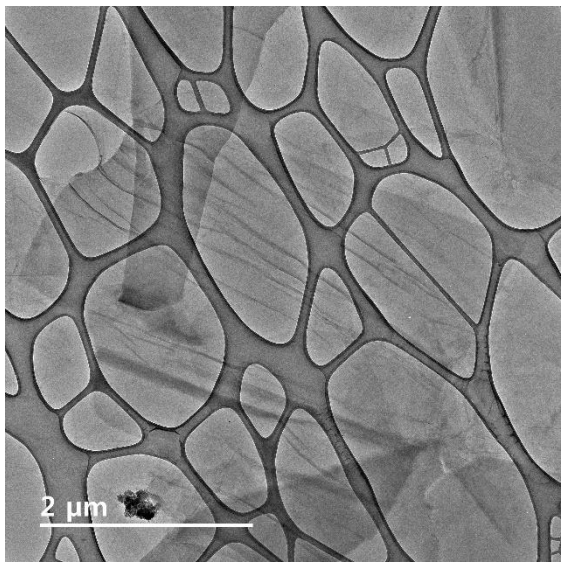

Figure 4-1. TEM image of as-synthesized GO

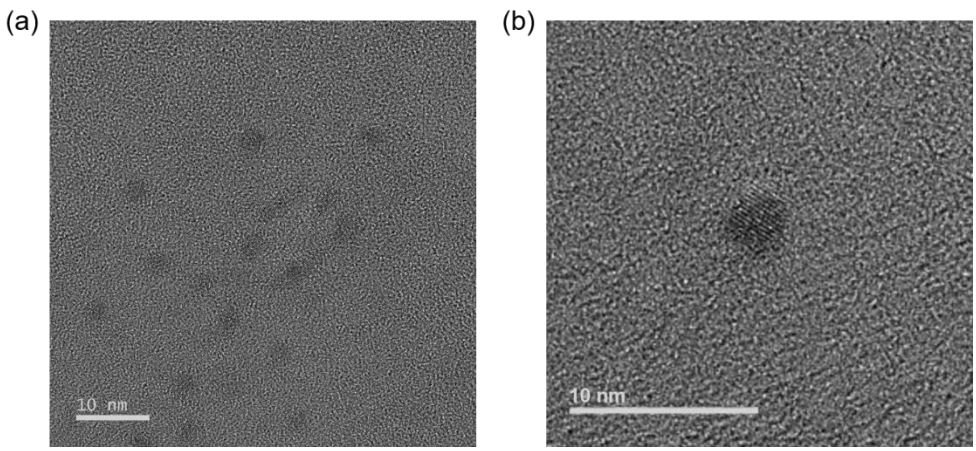

Figure 4-2. TEM image of as-synthesized GQD

To confirm a successful synthesis and properties of GQD-HA, we have conducted several analyses. In Figure 4-3(a), a crystalline structure with a lattice spacing of 0.24 nm was clearly observed, which corresponds to a (1120) in-plane lattice of graphene. Since

there was no change in size and lattice structure, we have confirmed that there was no change in the basic physical properties of GQD after HA functionalization. In the HR-TEM image of GQD-HA in Figure 4-3(b), we have confirmed that the average size of GQD-HA particles is 4 to 6 nm, which is almost the same as the average size of bare GQD.

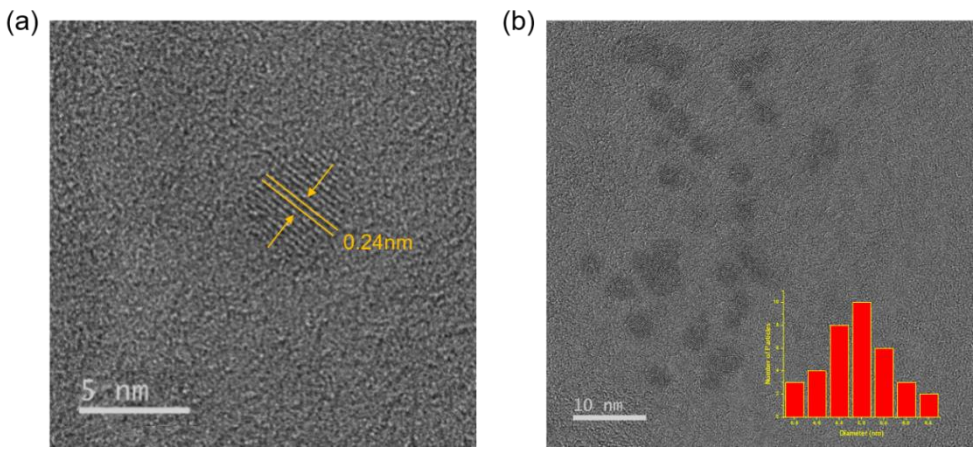

Figure 4-3. (a) High-resolution TEM image of GQD-HA. (b) TEM image with diameter distribution (inset)

We have performed FTIR and XPS analyses to verify the formation of amide bond between GQD and HA after the reaction. In the FTIR spectrum of GQD in Figure 4-4, we have demonstrated several characteristic peaks assigned to O-H, C=C and C-O bonds at 3330, 1603, and 1095 cm^{-1}.[18] In addition, other peaks assigned to O=C-OH and C-H bending vibrations at 1435 and 615 cm^{-1} were

confirmed. After HA functionalization, we have observed not only all characteristic peaks of bare GQD but also several new peaks assigned to the amide bond and N–H in–plane stretching at 1636 and 1575 cm^{-1}.[39] Based on these results, we confirmed that HA was covalently attached to the GQD.

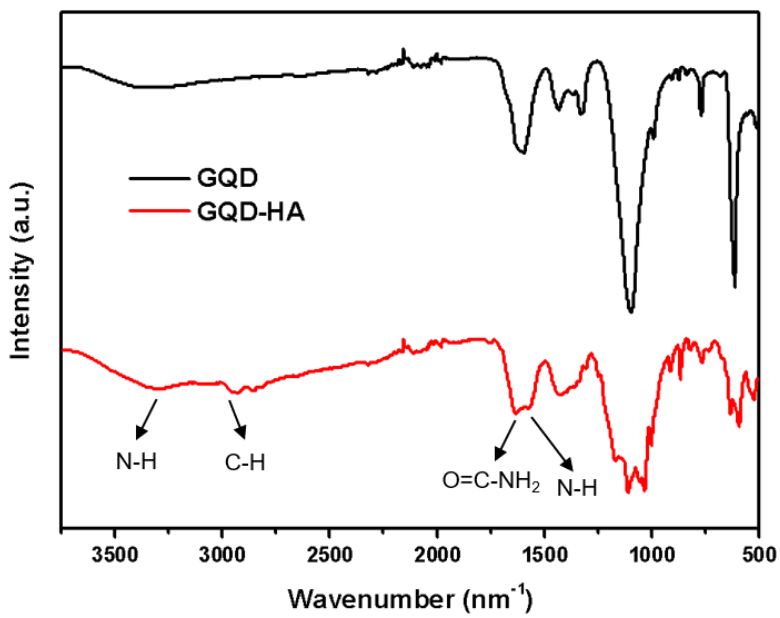

Figure 4–4. FT–IR spectra of GQD and GQD–HA

In the low–resolution XPS spectrum of GQD in Figure 4–5(a), we have observed several characteristic peaks assigned to carbon and oxygen at 284 and 540 eV. On the other hand, in the XPS spectrum of GQD–HA in Figure, a new peak assigned to nitrogen at 400 eV was observed, which clearly indicates the successful formation of

amide bond between GQD and HA. Actual amount of attached HA was estimated by integrating the area of the nitrogen peak in the low-resolution XPS spectra as follow:

We assumed that number of attached HA = n, Weight of HA =101n (ignoring Hydrogen atoms). HA contains n of nitrogen atoms and 6n of carbon atoms (Total 7n of atoms). From the low resolution XPS spectrum of GQD, we observed that carbon : oxygen = 1 : 1. We assumed that number of carbon = x, number of oxygen = x, weight of GQD = x×12+x×16=28x. After EDA attaching, the total number of atoms increased from 3x to 3x+7n. If the observed atomic percentage of nitrogen = p %, then

$$\frac{n}{3x+7n} = \frac{p}{100}$$

$$\frac{100-7p}{3p} n = x$$

From that,

$$Weight\ of\ GQD\ = 28x = \frac{28 \times (100-7p)}{3p} n$$

From that, we calculated wt% of HA

$$= \frac{303p}{28(100-7p)}$$

When 0.1 mL of HA was used for reaction, the actual amount of attached HA was 5.0 wt%.

Moreover, we deconvoluted the XPS spectra of GQD and GQD-HA to analyze the functional groups. In the deconvoluted C_{1s} spectrum of GQD in Figure 4-5(b), C-C, C-O, and C=O peaks were observed. After HA functionalization, it was confirmed that a new pick corresponding to C-N was raised in addition to the existing picks as shown in Figure 4-5(c). The presence of the C-N peak proves that the amide bond was successfully formed after the coupling reaction with HA. Furthermore, Figure 4-5(d) illustrates that the deconvoluted spectrum of N_{1s} shows free amine and amide bond peaks at 399.5 and 401.5 eV respectively.[40] The amide bond peak clearly demonstrates the presence of HA covalently attached to the GQD.

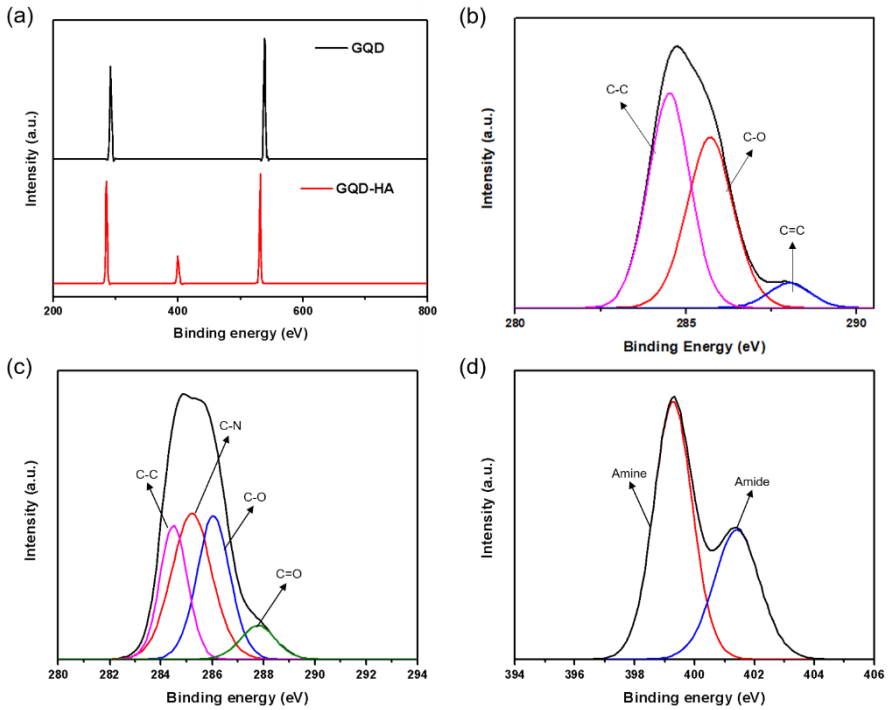

Figure 4-5. (a) Low-resolution XPS spectra of GQD and GQD-HA. Deconvoluted C_{1s} XPS spectrum of bare GQD. Deconvoluted (c) C_{1s} and (d) N_{1s} spectra of GQD-HA

In addition, we measured the Raman and XRD spectra of GQD and GQD-HA to characterize the defect states. In the Raman spectra of GQD and GQD-HA in Figure 4-6, the peak at 1580 cm^{-1} (G) assigned to vibration of sp^2-hybridized carbon atoms in the graphene lattice and the peak at 1350 cm^{-1} (D) assigned to out-of-plane vibration induced by structural defects were observed. We compared the intensity ratios of the D and G bands of GQD and GQD-HA. GQD-HA showed a higher I_D/I_G ratio (I_D/I_G = 1.02) than that of GQD (I_D/I_G

= 0.96), implying that structural defects were formed after HA functionalization.

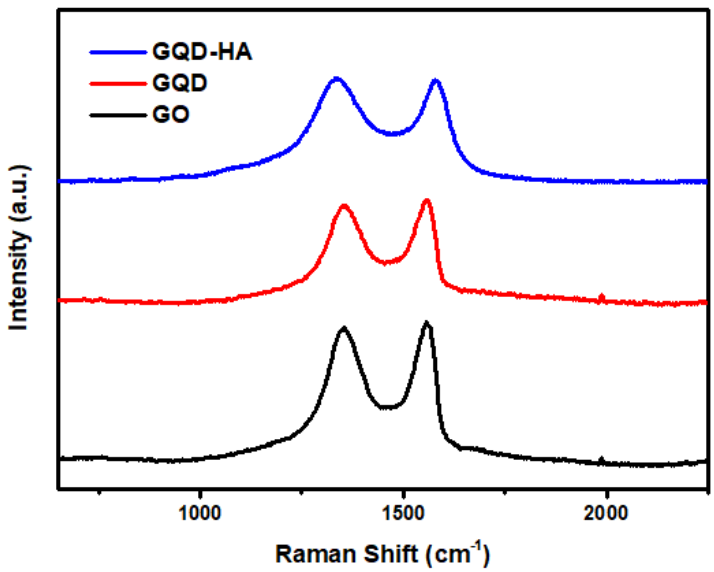

Figure 4-6. Raman spectrum of GO, bare GQD and GQD-HA

Moreover, as can be seen in the XRD spectrum in Figure 4-7, a broad peak at 24° corresponding to the (002) plane of graphene was confirmed. The broadness of the peak indicates that a large number of edge sites were established by the formation of GQD in the order of a few nanometers in size. However, we observed no significant changes in the XRD spectra of GQD after HA functionalization, suggesting no significant changes in the physical properties of the GQD core.

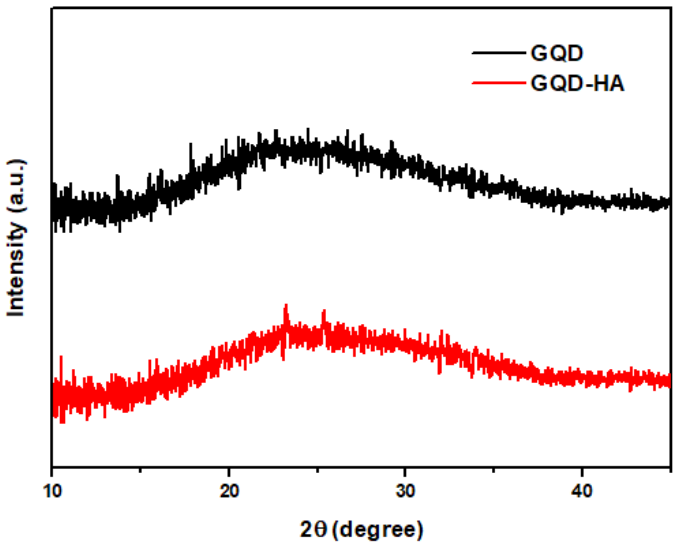

Figure 4-7. XRD spectra of GQD and GQD-HA

4.3.2 Structural characterization of HER system

After HER sample preparation, zeta potential and ELS analysis were performed to determine the stability and size of the complex system. First, the zeta potential of the sample was measured before and after visible light irradiation for 2 hours. When only TPATCS was used as a HER sample, the initial zeta potential (+32.23 mV) decreased to 9.76 mV after visible light irradiation, which means that the photostability of TPATCS is poor. On the other hand, when both TPATCS and GQD-HA were used together as a HER sample, the initial zeta potential (+28.59 mV) decreased to 17.99 mV after visible light irradiation. Comparing the initial zeta potential, it was confirmed

that the zeta potential was slightly decreased when GQD-HA was added, which is because the zeta potential of GQD-HA itself is negative (-10.15 mV). Comparing the zeta potential after visible light irradiation, it was confirmed that the absolute value of the zeta potential was maintained more stable after addition of GQD-HA. This result suggests that GQD-HA helps to improve the photostability of TPATCS. In addition, we have measured the size distribution data of the samples through ELS analysis as shown in Figure 4-8. The diameter of nanoparticles formed in the sample with GQD-HA material is about 2~3 times larger than that of the sample without GQD-HA. In particular, after irradiation with visible light for 2 hours, the average diameter of the sample without GQD-HA increased by about 3-4 times, whereas the average diameter of the sample with GQD-HA increased by about 1.5 times. These results suggest that GQD-HA helps to depress the morphology change of organic nanostructure under visible light. From the results of zeta potential analysis and ELS analysis, we confirmed that more photostable organic nanoparticles can be formed with GQD-HA.

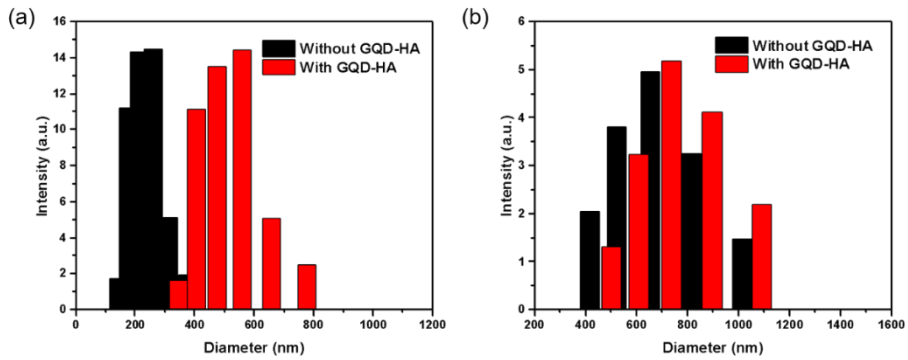

Figure 4-8. Size distribution data (a) before and (b) after 2 hours of visible light irradiation.

Additionally, we analyzed TEM images of TPATCS with and without GQD-HA as shown in Figure 4-9. Before the addition of GQD-HA, TPATCS had a hexagonal dumbbell-like shape with a width of about 400 to 600 nm in Figure 4-9(a), whereas after the addition of GQD-HA, amorphous smaller nanostructures were formed as shown in Figure 4-9(b). In HR-TEM image in Figure 4-9(c), we confirmed that the characteristic lattice structures of GQD-HA were distributed on the nanostructure, which indicates that GQD-HA can form a nanostructure with a modified morphology through close interaction with TPATCS. To confirm the photostability of the system, we also observed TEM images after 2 hours of visible light irradiation. In Figure 4-9(d), we confirmed that the hexagonal dumbbell-like of TPATCS was dismantled after visible light irradiation. In case of the

sample with GQD-HA, it was confirmed that there was no significant change in the morphology or size of the nanostructure as shown in Figure 4-9(e). In addition, through the remaining characteristic lattice structures of GQD-HA in HRTEM image shown in Figure 4-9(f), we found that GQD-HA was still distributed on the organic nanostructure even after irradiation with visible light.

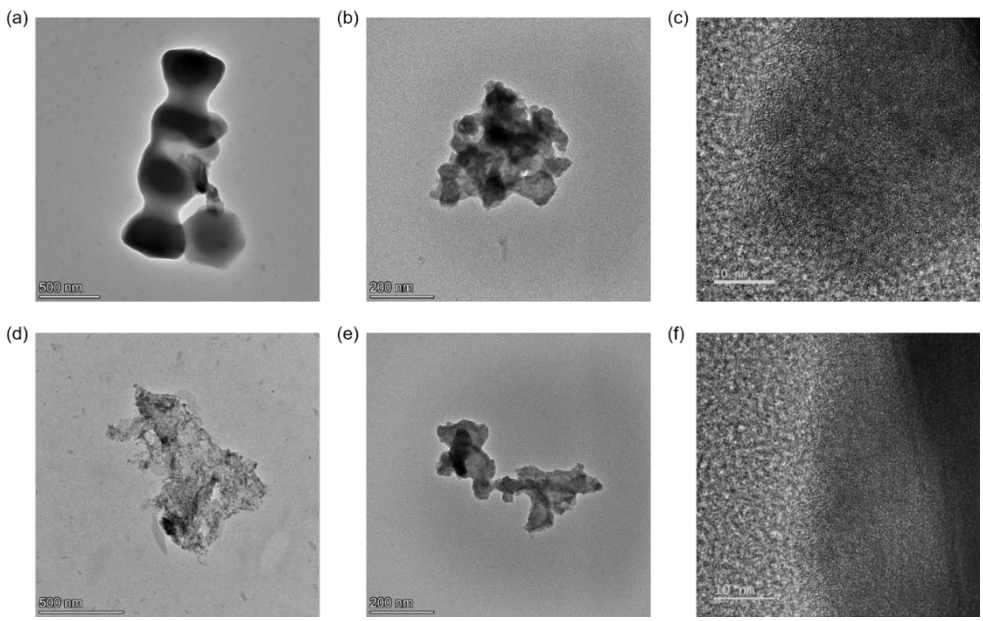

Figure 4-9. TEM image of TPATCS (a) without GQD-HA and (b) with GQD-HA before irradiation. (c) HRTEM image of TPATCS with GQD-HA before irradiation. TEM image of TPATCS (d) without GQD-HA and (e) with GQD-HA after irradiation. (f) HRTEM image of TPATCS with GQD-HA after irradiation.

In addition, we analyzed optical properties of TPATCS with and without GQD-HA. From absorption spectra in Figure 4-10, we found

that the width of absorption peak increased after the addition of GQD-HA.

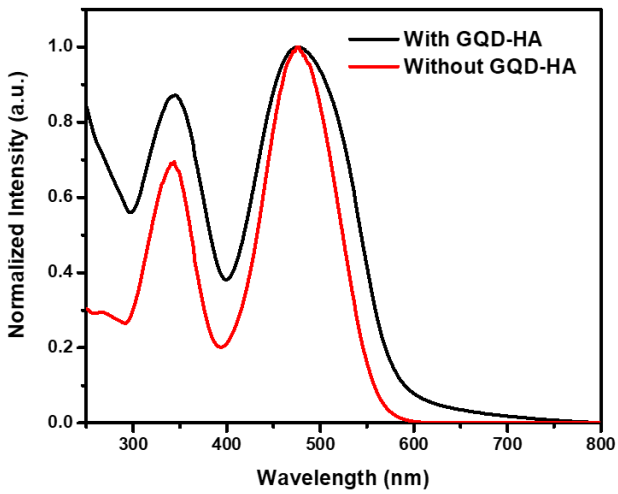

Figure 4-10. Absorption spectra of TPATCS with GQD-HA (black line) and without GQD-HA (red line).

In photoluminescence spectra in Figure 4-11, we also confirmed that the maximum peak was red-shifted and the peak intensity increased after the addition of GQD-HA. These results indicate that the aggregation property was changed by a close interaction with GQD-HA.

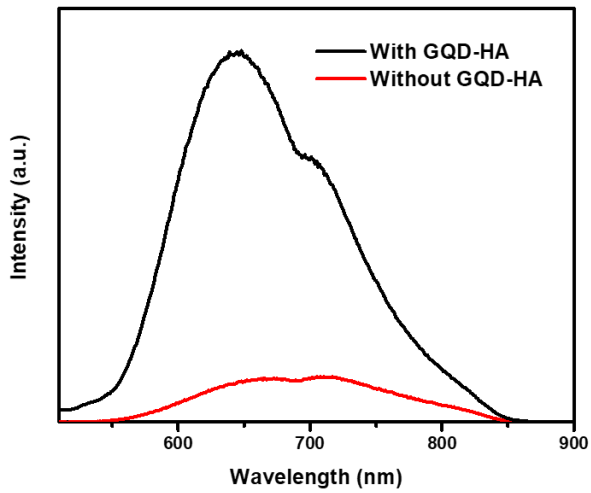

Figure 4-11. Photoluminescence spectra of TPATCS with GQD-HA (black line) and without GQD-HA (red line).

4.3.3 Photocatalytic HER performance

We have evaluated HER performance of the samples with ascorbic acid as a sacrificial electron donor under visible light (λ > 420 nm) irradiation. In Figure 4-12(a), we have confirmed that HER performance of the sample with GQD-HA shows significant enhancement in HER rate and stability compared to the sample without GQD-HA. With GQD-HA, the sample produced 0.276 mmol/g of hydrogen after 8 hours, which is more than 5 times the performance of the sample without GQD-HA (0.052 mmol/g of hydrogen after 3 hours). These results can be explained in detail as follows. We have confirmed that our TPATCS is capable of producing

hydrogen without any catalyst. However, its photostability is poor which may be due to the poor stability of the radical state, which is formed by photo-excited electrons. To improve the photostability, it is important to stabilize the radical state by achieving fast electron transfer. After the addition of GQD-HA, excited electrons in TPATCS transfer to the GQD-HA and the radical state is rapidly removed. In other words, TPATCS is rapidly stabilized, and stabilized TPATCS absorbs visible light again and forms excited electrons. For this reason, the sample containing GQD-HA showed more stable HER performance than the sample without it. In addition, we have measured HER performance of the samples with simulated seawater (0.15 M of NaCl) as shown in Figure 4-12(b). As in the pure water, the sample with GQD-HA showed greatly improved HER performance (initial rate of 0.182 mmol/g · h and 1.303 mmol/g of hydrogen after 15 hours) compared to the sample without GQD-HA (initial rate of 0.044 mmol/g · h and 0.121 mmol/g of hydrogen after 3 hours). These results clearly indicate that GQD-HA acts as an efficient photocatalyst for HER in seawater under visible light irradiation. To clarify why HER performance improved in seawater, we have also measured HER performance of a sample with 0.15 M of NaI aqueous solution. As shown in Figure 4-12(c), the sample with

iodide showed much more improved HER performance than the sample with simulated seawater. As described in the previous paper from our group, the improvements of HER performance after the addition of iodides can be explained by heavy atom effect. When the atomic weight of the added halides increases, triplet state can be utilized by an increase of intersystem crossing. This can prevent the excited electrons from losing energy through unwanted pathways. As a result, the excited state lifetime increases, which allows more frequent utilization of excited electrons for HER. In addition, we have calculated wavelength dependent apparent quantum yield (AQY) values with the sample with GQD-HA to get more insight into its HER performance. Under 450, 500, and 550 nm light irradiation, they showed AQY values of 18.1, 22.5 and 11.3%, respectively, which are in good agreement with the absorption spectrum of TPATCS as shown in Figure 4-12(d). From these results, we successfully confirmed that the organic molecule acts as the photosensitizer in the HER system. We concluded that self-assembled organic nanostructure with amphiphilic GQD-HA could be an efficient and stable metal-free heterogeneous photocatalytic HER system.

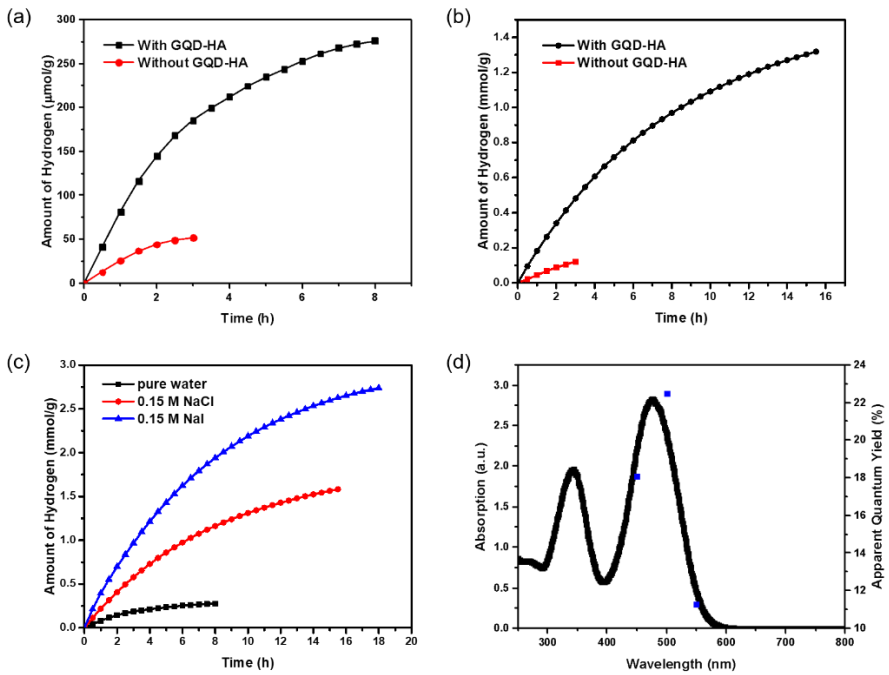

Figure 4-12. HER performance of TPATCS with GQD-HA (black line) and without GQD-HA (red line) (a) in pure water and (b) in simulated seawater. (c) Effect of halides on HER performance. (d) AQY values and the absorption spectrum of TPATCS.

4.3.4 Electrochemical measurements

We have also confirmed the Mott-Schottky plot of GQD-HA displayed in Figure 4-13. Only the p-type semiconductor behavior was observed in the Mott-Schottky plot of bare GQD as shown in Figure 4-13(a), whereas the n-type semiconductor behavior was observed in the Mott-Schottky plot of GQD-HA as shown in Figure 4-13(b). These results indicate that the carboxylic groups in GQD are electron trap sites which can effectively be passivated by amide

bond formation and restore n-type conductivity. The lack of n-type semiconducting properties in bare GQD is due to the electron trapping property of functional groups such as carboxyl and hydroxyl groups. After HA functionalization, these electron trapping sites are effectively passivated, giving them n-type semiconducting properties.

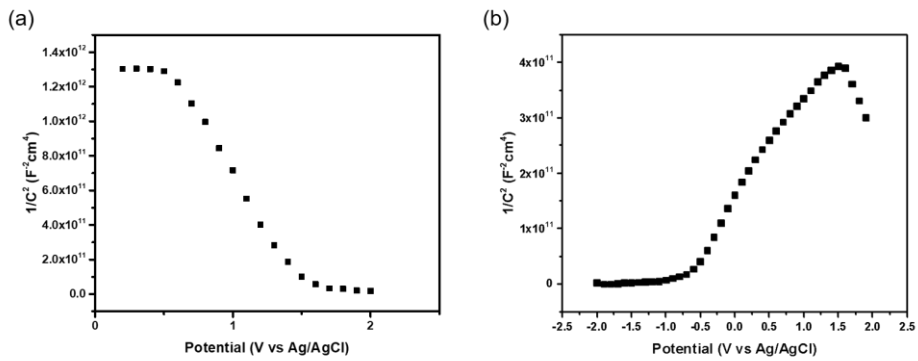

Figure 4-13. Mott-Schottky plots of (a) bare GQD and (b) GQD-HA

We have measured several electrochemical measurements with bare GQD and GQD-HA to better understand the electrochemical properties changed after HA functionalization. We have conducted linear sweep voltammetry (LSV) measurements and determined the conduction band (CB) position of the materials from the intercept of linear extrapolation. The CB positions of bare GQD and GQD-HA are found to be -1.22 V and -1.32 V (vs Ag/AgCl) as shown in Figure 4-14(a), which is higher enough to reduce protons. Notably, we

confirmed that the current density of the GQD-HA electrode is much higher than that of the bare GQD electrode. In addition, we have measured charge transfer resistance of bare GQD and GQD-HA by EIS analysis. As shown in Figure 4-14(b), the Nyquist plot of GQD-HA has a smaller semicircle radius compared to that of bare GQD at open circuit voltage condition, which indicates that GQD-HA have more efficient charge separation properties and higher charge transfer rate than bare GQD. This is also because HA functionalization efficiently passivated electron trapping sites of GQD such as carboxylic and hydroxyl groups and restored n-type conductivity, which aided in promoting fast charge mobility. Since charge mobility is essential for HER performance, it could be one of the major reasons for the enhanced HER performance of GQD-HA. We also measured the oxidation potential of TPATCS by cyclic voltammetry (CV) measurements as shown in Figure 4-14(c). The measured highest occupied molecular orbital (HOMO) position of TPATCS is -5.6 eV and the lowest unoccupied molecular orbital (LUMO) position is -3.0 eV which is estimated from HOMO and the optical band gap of 2.6 eV. From these results, we drew an energy band diagram for the photocatalytic system regarding the HER mechanism under visible light irradiation as shown in Figure 4-

14(d). After visible light absorption, the excited electrons are generated in TPATCS and transferred to the CB of GQD-HA. Holes generated in TPATCS are filled by transferred electrons from ascorbic acid during the HER mechanism.

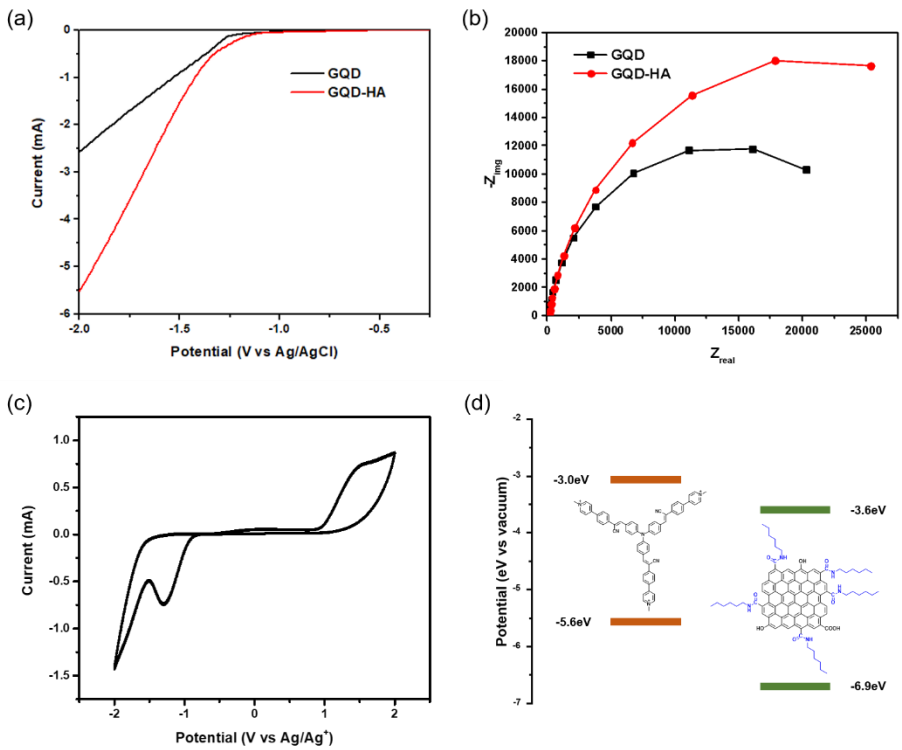

Figure 4-14. (a) LSV curve of GQD and GQD-HA. (b) Nyquist plots of GQD and GQD-HA. (c) C-V curve of TPATCS. (d) Electronic band structure of HER system.

4.4 Conclusion

In summary, we demonstrated photocatalytic HER system which can

produce hydrogen efficiently in seawater. The synthesized GQD-HA had close interaction with amphiphilic TPATCS in aqueous solution and formed photostable nanostructure. It was confirmed that the formed nanostructure can efficiently and stably produce hydrogen (maximum AQY of 22.5% under 500 nm light irradiation) in simulated seawater. From these results, we clearly confirmed that amphiphilic GQD can act as an efficient photocatalyst for HER in seawater. In electrochemical measurements, we verified that the charge separation and transfer properties are much improved after HA functionalization, which could passivate electron trapping sites. We concluded that amphiphilic GQD could act as a photocatalyst as well as a stabilizer of the organic molecule and it shows good photocatalytic HER performance in seawater. This study suggests a new strategy to design an efficient and stable metal-free photocatalytic system for HER in seawater.

Bibliography

1. Tachibana, Y.; Vayssieres, L.; Durrant, J. R., *Nature Photonics* **2012,** *6* (8), 511−518.

2. Takanabe, K., *ACS Catalysis* **2017,** *7* (11), 8006−8022.

3. Pratibha; Kapoor, A.; Rajput, J. K., *International Journal of Hydrogen Energy* **2022,** *47* (40), 17544−17582.

4. Ayyub, M. M.; Chhetri, M.; Gupta, U.; Roy, A.; Rao, C. N. R., *Chemistry – A European Journal* **2018,** *24* (69), 18455−18462.

5. Yao, Y.; Gao, X.; Meng, X., *International Journal of Hydrogen Energy* **2021,** *46* (13), 9087−9100.

6. Li, J.; Sun, J.; Li, Z.; Meng, X., *International Journal of Hydrogen Energy* **2022,** *47* (69), 29685−29697.

7. Millero, F. J.; Feistel, R.; Wright, D. G.; McDougall, T. J., *Deep Sea Research Part I: Oceanographic Research Papers* **2008,** *55* (1), 50−72.

8. Fujishima, A.; Honda, K., *Nature* **1972,** *238* (5358), 37−38.

9. Yang, Y.; Niu, S.; Han, D.; Liu, T.; Wang, G.; Li, Y., *Advanced Energy Materials* **2017,** *7* (19), 1700555.

10. Guo, Y.; Park, T.; Yi, J. W.; Henzie, J.; Kim, J.; Wang, Z.; Jiang, B.; Bando, Y.; Sugahara, Y.; Tang, J.; Yamauchi, Y., *Advanced Materials* **2019,** *31* (17), 1807134.

11. Hong, L.−f.; Guo, R.−t.; Yuan, Y.; Ji, X.−y.; Lin, Z.−d.; Li, Z.−s.; Pan, W.−g., *ChemSusChem* **2021,** *14* (2), 539−557.

12. Liu, Y.; Zheng, X.; Yang, Y.; Li, J.; Liu, W.; Shen, Y.; Tian, X.,

ChemCatChem **2022,** *14* (5), e202101439.

13. Zhao, H.; Jian, L.; Gong, M.; Jing, M.; Li, H.; Mao, Q.; Lu, T.; Guo, Y.; Ji, R.; Chi, W.; Dong, Y.; Zhu, Y., *Small Structures* **2022,** *3* (7), 2100229.

14. Zhou, W.; Jia, T.; Shi, H.; Yu, D.; Hong, W.; Chen, X., *Journal of Materials Chemistry A* **2019,** *7* (1), 303-311.

15. Rahman, M. Z.; Kibria, M. G.; Mullins, C. B., *Chemical Society Reviews* **2020,** *49* (6), 1887-1931.

16. Hu, C.; Dai, Q.; Dai, L., *Cell Reports Physical Science* **2021,** *2* (2), 100328.

17. Elsayed, M. H.; Jayakumar, J.; Abdellah, M.; Mansoure, T. H.; Zheng, K.; Elewa, A. M.; Chang, C.-L.; Ting, L.-Y.; Lin, W.-C.; Yu, H.-h.; Wang, W.-H.; Chung, C.-C.; Chou, H.-H., *Applied Catalysis B: Environmental* **2021,** *283*, 119659.

18. Peng, J.; Gao, W.; Gupta, B. K.; Liu, Z.; Romero-Aburto, R.; Ge, L.; Song, L.; Alemany, L. B.; Zhan, X.; Gao, G.; Vithayathil, S. A.; Kaipparettu, B. A.; Marti, A. A.; Hayashi, T.; Zhu, J.-J.; Ajayan, P. M., *Nano Letters* **2012,** *12* (2), 844-849.

19. Bacon, M.; Bradley, S. J.; Nann, T., *Particle & Particle Systems Characterization* **2014,** *31* (4), 415-428.

20. Ghaffarkhah, A.; Hosseini, E.; Kamkar, M.; Sehat, A. A.; Dordanihaghighi, S.; Allahbakhsh, A.; van der Kuur, C.; Arjmand, M., *Small* **2022,** *18* (2), 2102683.

21. Yeh, T.-F.; Teng, C.-Y.; Chen, S.-J.; Teng, H., *Advanced Materials* **2014,** *26* (20), 3297-3303.

22. Chung, S.; Revia, R. A.; Zhang, M., *Advanced Materials* 2021, *33* (22), 1904362.

23. Yang, J.; Miao, H.; Jing, J.; Zhu, Y.; Choi, W., *Applied Catalysis B: Environmental* 2021, *281*, 119547.

24. Zahir, N.; Magri, P.; Luo, W.; Gaumet, J. J.; Pierrat, P., *ENERGY & ENVIRONMENTAL MATERIALS* 2022, *5* (1), 201-214.

25. Park, H.; Park, S. Y., *ACS Applied Materials & Interfaces* 2022, *14* (23), 26733-26741.

26. Min, S.; Lu, G., *The Journal of Physical Chemistry C* 2011, *115* (28), 13938-13945.

27. Min, S.; Lu, G., *International Journal of Hydrogen Energy* 2012, *37* (14), 10564-10574.

28. Min, S.; Lu, G., *International Journal of Hydrogen Energy* 2013, *38* (5), 2106-2116.

29. Zhang, W.; Li, Y.; Peng, S., *ACS Applied Materials & Interfaces* 2016, *8* (24), 15187-15195.

30. Dinda, D.; Park, H.; Lee, H.-J.; Oh, S.; Park, S. Y., *Carbon* 2020, *167*, 760-769.

31. Dinda, D.; Park, H.; Park, S. Y., *Journal of Catalysis* 2021, *404*, 273-282.

32. Hyunho Park; Illia E. Serdiuk; Soo Young Park, 2022.

33. Maeda, K.; Masuda, H.; Domen, K., *Catalysis Today* 2009, *147* (3), 173-178.

34. Li, Y.; Gao, D.; Peng, S.; Lu, G.; Li, S., *International Journal of*

Hydrogen Energy 2011, *36* (7), 4291-4297.

35. Guo, L.; Yang, Z.; Marcus, K.; Li, Z.; Luo, B.; Zhou, L.; Wang, X.; Du, Y.; Yang, Y., *Energy & Environmental Science* 2018, *11* (1), 106-114.

36. Yang, X.; Hu, Z.; Yin, Q.; Shu, C.; Jiang, X.-F.; Zhang, J.; Wang, X.; Jiang, J.-X.; Huang, F.; Cao, Y., *Advanced Functional Materials* 2019, *29* (13), 1808156.

37. Liu, Y.; Liao, Z.; Ma, X.; Xiang, Z., *ACS Applied Materials & Interfaces* 2018, *10* (36), 30698-30705.

38. Lee, H.-J.; Abudulimu, A.; Roldao, J. C.; Nam, H.; Gierschner, J.; Lüer, L.; Park, S. Y., *ChemPhotoChem* 2022, *n/a* (n/a), e202200177.

39. Ji, Y.; Yang, X.; Ji, Z.; Zhu, L.; Ma, N.; Chen, D.; Jia, X.; Tang, J.; Cao, Y., *ACS Omega* 2020, *5* (15), 8572-8578.

40. Ederer, J.; Janoš, P.; Ecorchard, P.; Tolasz, J.; Štengl, V.; Beneš, H.; Perchacz, M.; Pop-Georgievski, O., *RSC Advances* 2017, *7* (21), 12464-12473.

List of Publications

1. Dinda, D.; Park, H.; Lee, H.-J.; Oh, S.; Park, S. Y., "Graphene quantum dot with covalently linked rhodamine dye: A high efficiency photocatalyst for hydrogen evolution", *Carbon* 2020, *167*, 760-769.
2. Dinda, D.; Park, H.; Park, S. Y., "Ultra-stable dye-sensitized graphene quantum dot as a robust metal-free photocatalyst for hydrogen production", *Journal of Catalysis* 2021, 404, 273-282.
3. Park, H.; Park, S. Y., "Enhancing the Alkaline Hydrogen Evolution Reaction of Graphene Quantum Dots by Ethylenediamine Functionalization", *ACS Applied Materials & Interfaces* 2022, 14 (23), 26733-26741.
4. Park, H.; Serdiuk, I. E.; Park, S. Y., "Amphiphilic Graphene Quantum Dots: Metal-Free Photocatalyst for Hydrogen Evolution via Encapsulation of Organic Thermally Activated Delayed Fluorescence Photosensitizers", *ChemPhotoChem* 2022, e202200267.

List of Presentations

1. (poster) All-organic Supramolecular Photosensitizer Template Consisting of Cyanostilbene Derivatives for Photocatalytic Hydrogen Evolution, Hyunho Park, Hyun-Jun Lee, Ji Eon Kwon, and Soo Young Park*, 한국고분자학회 추계학술대회, 11 October, 2019, Republic of Korea.

List of Patents

1. 박수영, 이현준, 딥티만 딘다, 박현호, “가시광 감응 광촉매 구조체, 그 제조방법 및 그를 이용한 물 분해 수소 생산 방법”, 대한민국 제 10-2251004 호.

초 록

대표적인 신재생에너지 자원 중 하나인 수소에너지는 이동과 교통이 편리하고 에너지 밀도가 높아 최근 많은 관심을 받고 있다. 수소 에너지를 효율적으로 생산하기 위해서는 수소 생산 반응(HER)을 위한 효율적인 광촉매 물질을 찾는 것이 요구된다. 가장 유망한 광촉매 물질 중 하나는 그래핀 양자점(GQD)으로, 이미 HER 광촉매로 여러 차례 연구된 유망한 HER 광촉매 소재 중 하나이지만, 가시광선 흡수율이 낮고 표면에 분포되어있는 전하 트랩 영역으로 인해 HER 성능이 제한된다. 따라서 효율적인 HER을 위한 개조 및 설계에 대한 연구가 여전히 필요하다. 본 논문은 GQD에 대한 화학적 표면 개질 전략과 염료 감응 전략을 통해 효율적인 HER 광촉매를 설계하는 데 초점을 맞췄다.

제2장에서는 아미드 결합 형성 반응에 의해 에틸렌다이아민(EDA)이 기능화된 GQD를 합성하였다. EDA 기능화된 GQD(GQD-EDA)는 GQD(10시간 동안 150 μmol/g의 수소)에 비해 현저하게 증가된 HER 성능(10시간 동안 342 μmol/g의 수소)을 보였다. 중요한 것은 GQD-EDA의 HER 성능이 pH에 비례하여 증가하고 pH = 10에서 가장 높은 성능을 보였다는 점인데, 이는 보통의 GQD의 HER 성능이 pH와 함께 감소하는 것과는 대조적이다. 선형 스위프 전압 측정 및 전기화학적 임피던스 분광법을 통해 공유결합된 EDA가 물 해리 부위로 작용하여 알칼리 매질 내 광촉매 HER을 향상시키는 것을 확인할 수 있다.

제3장에서는 아미드 결합 형성 반응을 통해 헥실아민(HA)으로

기능화된 양친매성 GQD를 합성하였다. 헥실아민 기능화된 GQD(GQD-HA)는 양친매성이며, 광촉매와 계면활성제로 동시에 작용할 수 있음을 확인하였다. GQD-HA는 TADF 특성을 가진 소수성 광감응제와 함께 기존 GQD보다 훨씬 더 안정적인 복합 나노입자를 형성할 수 있다. 중요한 것은 HA 기능화 후 복합 시스템의 HER 성능(14시간 동안 11.64 mmol/g의 수소)과 안정성이 크게 향상된다는 것이다. 전기화학적 분석을 통해 GQD-HA가 광감응제와 함께 형성한 나노입자가 효율적인 전하분리 및 빠른 전하전달 특성을 가짐을 확인하였다.

제4장에서는 가시광선 감응 염료를 포함하는 GQD-HA의 고효율 광촉매 HER 시스템이 시연되었다. HA 기능화는 전하 트랩 구역을 부동태화함과 동시에 염료 감음 전략의 적용 가능성을 제공함으로써 GQD가 수소를 보다 효율적으로 생산할 수 있도록 돕는다는 것을 확인하였다. GQD-HA는 광감응제와의 강력한 상호작용을 통해 변형된 나노구조를 형성하였다. 염료가 혼합된 GQD-HA 나노구조물은 효율적인 HER 성능(초기 속도 0.182 mmol/g · h, 15시간 후 수소 1.303 mmol/g)과 500 nm 광조사 하에서 22.5%의 AQY를 나타냈다. 또한 증류수와 모의 해수 모두에서 향상된 안정성을 보였다. 전기화학적 분석을 통해 확인한 결과, 염료 감응형 GQD-HA는 높은 전하분리 및 효율적인 전하전달 특성을 나타내었다.

Keywords : 물분해; 광촉매; 수소생산; 광감응제; 기능화; 그래핀양자점.

Student Number : 2018-21006